

# **The zonal approach applied to the simulation of the radiative heat transfer in a packed pebble bed**

**S van der Walt**

 **[Orcid.org/0000-0002-9307-2876](https://orcid.org/0000-0002-9307-2876)**

Thesis accepted in fulfilment of the requirements for the degree  
*Doctor of Philosophy in Nuclear Engineering* at the North-West  
University

Promoter: Prof CGDK du Toit

Co-promoter: Prof PG Rousseau

Graduation: May 2020

Student number: 20399782

# Declaration of Authorship

I, Stefan VAN DER WALT, declare that this thesis titled, “The zonal approach applied to the simulation of the radiative heat transfer in a packed pebble bed” and the work presented in it are my own. I confirm that:

- This work was done wholly or mainly while in candidature for a research degree at this University.
- Where any part of this thesis has previously been submitted for a degree or any other qualification at this University or any other institution, this has been clearly stated.
- Where I have consulted the published work of others, this is always clearly attributed.
- Where I have quoted from the work of others, the source is always given. With the exception of such quotations, this thesis is entirely my own work.
- I have acknowledged all main sources of help.
- Where the thesis is based on work done by myself jointly with others, I have made clear exactly what was done by others and what I have contributed myself.

Signed:

---

Date:

---

*“For I know the plans I have for you,” says the LORD . “They are plans for good and not for disaster, to give you a future and a hope.”*

Jeremiah 29:11

*“All models are wrong, but some are useful.”*

George Box

*“Humility is to make a right estimate of one’s self.”*

Charles Spurgeon

## *Abstract*

The Fukushima Daiichi Nuclear Disaster highlighted the importance of nuclear safety and the importance of modeling a nuclear reactor under diverse conditions. Applied to pebble bed reactors, these diverse conditions include taking into account the macroscopic temperature gradient through the bed. At high temperatures the thermal radiation component of the effective thermal conductivity becomes the dominant heat transfer mode and the short-range and long-range radiation must be properly taken into account.

The Multi-Sphere Unit Cell (MSUC) model was developed to address the shortcomings in the conduction and radiation components of the effective thermal conductivity model. Although the conduction component was properly addressed, the long-range component of the thermal radiation component still had some shortcomings. The Zonal Approach, which is a network-type approach, was suggested to replace the thermal radiation component of the MSUC model due to its simplicity, capability to model long-range radiation and its relatively fast solution time.

The participating medium of the Zonal Approach was changed from a semi-transparent porous medium to a medium containing surfaces to accommodate the large spheres inside a packed bed. The emission and absorption from volume zones effectively changed to surface-to-surface exchange. The volume-to-surface and volume-to-volume direct exchange areas were re-derived to accommodate the changes in the volume zones. The attenuation factors for both the simple cubic and random packed beds were derived. The derived attenuation factor for the random bed included the wall region, near-wall region and bulk region. The zones were also subdivided to account for non-isothermal sphere surface temperatures.

The thermal radiation results from the adapted Zonal Approach were compared to the results from a Computational Fluid Dynamics (CFD) package using surface-to-surface radiation only without solid models to eliminate the effect of heat transfer from solid conduction. The results were generally in good agreement with the CFD results, but it highlighted the importance of an accurate attenuation factor.

The conduction component from the MSUC model was coupled to the Zonal Approach and the results were compared to the Near-wall Thermal Conductivity Test Facility (NWTCTF) experimental results for a simple cubic and a random packed bed. The predicted heat was in good agreement with the experimental results but the predicted thermal resistance was too low.

The Zonal Approach generally predicted the thermal radiation well for both the simple cubic and random packed beds. The subdivision of the control volumes or zones eliminated

the need for a conductivity correction parameter needed to correct non-isothermal sphere surfaces. With further improvement of certain components the accuracy of the results can be improved.

**Keywords:** *Zonal Approach, Pebble Bed Reactor, Thermal Radiation, Thermal Conductivity.*

## *Acknowledgements*

I would first like to thank my wife Bernice, who kept on encouraging me through this whole process and were subject to a lot of lonely nights and weekends. I love you very much and I promise to spoil you after this project is finished. I would also like to thank my parents for their continued support throughout my years of study. They encouraged me to read from a very early age, challenged me to think beyond my known environment and helped me when I got stuck. Thank you also for your advice and mentorship throughout this project. A special dedication to my dad who never got the chance to finish his Doctorate. I would also like to thank my family for their support and encouragement, especially my youngest sister Nadia who proofread my thesis. I would also like to thank my study leaders for their wisdom, input and support over this period. Last but not least I would like to thank Jesus Christ, my Saviour, for endowing me with the grace and opportunity to finish my studies.

This work is based upon research supported by the South African Research Chairs Initiative of the Department of Science and Technology and National Research Foundation (Grant No. 61059). Any opinion, finding and conclusion or recommendation expressed in this material is that of the author and the NRF does not accept any liability in this regard.

# Contents

<b>Declaration of Authorship</b>	<b>i</b>
<b>Abstract</b>	<b>iii</b>
<b>Acknowledgements</b>	<b>v</b>
<b>1 Introduction and Background</b>	<b>1</b>
1.1 Introduction . . . . .	1
1.2 Model Selection . . . . .	2
1.3 Problem Statement . . . . .	4
1.4 Hypothesis . . . . .	4
1.5 Methodology . . . . .	4
1.6 Contributions of this Study . . . . .	5
1.7 Chapter Layout . . . . .	5
<b>2 Thermal Radiation in a Packed Pebble Bed</b>	<b>6</b>
2.1 Introduction . . . . .	6
2.2 Background . . . . .	6
2.2.1 Different Approaches to Model Radiation Heat Transfer . . . . .	6
2.2.1.1 Overview . . . . .	6
2.2.1.2 Exact Solutions to the RTE . . . . .	9
2.2.1.3 Statistical Approach . . . . .	9
2.2.1.4 Flux Models . . . . .	9
2.2.1.5 Network-type Approaches . . . . .	11
2.3 The Multi-sphere Unit Cell (MSUC) Model . . . . .	11
2.3.1 The Current Study's Initial Progress with SUN Model . . . . .	13
2.3.2 The Zonal Approach . . . . .	17
2.4 Summary . . . . .	19
<b>3 The Zonal Approach Applied to a Packed Pebble Bed</b>	<b>20</b>
3.1 Introduction . . . . .	20
3.2 Background . . . . .	21

3.3	Radiative exchange without a participating medium . . . . .	21
3.4	Radiative exchange with a participating medium . . . . .	22
3.4.1	Derivation of surface to volume direct exchange area . . . . .	22
3.4.2	Derivation of the emission of an isothermal volume . . . . .	25
3.4.3	Derivation of volume to surface direct exchange area . . . . .	27
3.4.4	Derivation of volume to volume direct exchange area . . . . .	28
3.5	Energy balances for the Zonal Approach . . . . .	29
3.6	Adapting the Zonal Approach for Surface Exchange . . . . .	30
3.6.1	Background . . . . .	30
3.6.2	Exchange for a volume zone containing one centralised sphere . .	31
3.6.2.1	Surface to surface direct exchange areas . . . . .	31
3.6.2.2	Volume to surface direct exchange areas . . . . .	33
3.6.2.3	Volume to volume direct exchange areas . . . . .	34
3.6.3	Evaluating the Direct-Exchange Areas . . . . .	36
3.6.3.1	Surface-to-Surface Exchange Evaluation . . . . .	36
3.6.3.2	Volume-to-Surface Exchange Evaluation . . . . .	37
3.6.3.3	Volume-to-Volume Exchange Evaluation . . . . .	38
3.6.4	Exchange of a volume zone containing random-packed spheres . .	41
3.6.4.1	Surface area inside a random-packed volume zone . . .	41
3.6.4.2	Internal radiation inside a random-packed volume zone	43
3.6.4.3	Direct exchange areas for a volume zone from a random- packed bed . . . . .	44
3.7	Smoothing of the direct exchange areas . . . . .	44
3.8	Energy balance for an enclosure filled with mono-sized spheres . . . . .	46
3.9	Solving for the radiosities and temperatures . . . . .	46
3.10	Deriving the attenuation factor . . . . .	49
3.11	Conduction Coupled to Radiation . . . . .	50
3.12	MSUC Conduction Component . . . . .	55
3.13	Summary . . . . .	57
<b>4</b>	<b>Comparison of Thermal Radiation Results</b>	<b>58</b>
4.1	Introduction . . . . .	58
4.2	Solving the model without a participating medium . . . . .	58
4.3	Solving the model with a participating medium . . . . .	59
4.3.1	Thermal Radiation in a Simple Cubic Bed . . . . .	59
4.3.1.1	The Attenuation Factor in a Simple Cubic Bed . . . . .	59
4.3.1.2	Comparison of Thermal Radiation Results in a Simple Cubic Bed . . . . .	61



4.3.1.3	Random Bed Attenuation Factor . . . . .	66
4.3.1.4	Comparison of Thermal Radiation Results in a Random Packed Bed . . . . .	68
4.3.2	Comparison with the NWTCTF . . . . .	75
4.3.2.1	The NWTCTF . . . . .	75
4.3.2.2	Comparison with the NWTCTF Simple Cubic Cases . .	75
4.3.2.3	Comparison with the NWTCTF Random Packed Cases	76
4.4	Summary . . . . .	83
<b>5</b>	<b>Conclusions and Recommendations</b>	<b>84</b>
5.1	Summary . . . . .	84
5.2	Conclusions . . . . .	86
5.3	Recommendations for Further Research . . . . .	86
	<b>Bibliography</b>	<b>88</b>
<b>A</b>	<b>Appendix A: Matlab Model for Radiation-Conduction Model</b>	<b>92</b>

# List of Figures

1.1	Chinese HTR . . . . .	1
1.2	MSUC Model Development . . . . .	3
2.1	The shells surrounding the viewed sphere demarcating the view factors allocated to the surround spheres. . . . .	12
2.2	Comparison of SUN results to CFD simulation for a fixed central sphere temperature and enclosure boundary heat removal rate (left) and fixed central sphere and enclosure temperature (right). . . . .	13
2.3	A typical section from an annular packed bed (left) and the CSUN model setup of the HTTU (Van der Meer, 2011). . . . .	14
2.4	Results comparison between the CSUN model and the HTTU test in the bulk region for the 82.7kW case (Van der Meer, 2011). . . . .	14
2.5	Demonstration of the computational grid with a sphere-centered control volume (left) and a generic control volume (right). . . . .	15
2.6	The results of the adapted SUN model compared to CFD results with the inner temperature and enclosure heat prescribed (left) and for inner and enclosure temperature prescribed (right). . . . .	16
2.7	The results using the error redistribution procedure for the cubic model case (left) and the near-spherical model case (right) . . . . .	17
2.8	Zonal Approach on Furnace . . . . .	18
3.1	Radiation exchange between two differential surfaces. . . . .	21
3.2	Surface to Volume Radiation Exchange . . . . .	23
3.3	Emmision of a Volume Element . . . . .	25
3.4	Volume to a Surface Radiation Exchange . . . . .	27
3.5	Volume to Volume Radiation Exchange . . . . .	28
3.6	A representation of a cubic structured bed subdivided by equally sized volume and surface zones. . . . .	32
3.7	A representation of a volume zone for a cubic structured bed containing one centralised sphere. . . . .	32
3.8	Radiation exchange between a sphere and a surface element. . . . .	33
3.9	Radiation exchange between two spheres. . . . .	35

3.10	Figure to be used together with eq. [3.60] to calculate the exchange between two identical parallel plates, from Howell and Mengüç (2011).	37
3.11	Surface-to-surface exchange plot of derived Zonal correlation and analytical correlation from Hamilton and Morgan, 1952.	38
3.12	Volume-to-surface emission for a sphere to a flat surface.	39
3.13	Figure to be used together with eq. [3.61] to calculate the exchange between a sphere and a perpendicular plate, from Howell and Mengüç (2011).	40
3.14	Volume-to-surface exchange plot of derived Zonal correlation and analytical correlation from Feingold and Gupta (1970).	40
3.15	Figure to be used together with eq. [3.64] to calculate the exchange between two spheres, from Howell and Mengüç (2011).	41
3.16	Volume-to-volume exchange comparing the derived correlation from eq. [3.62] to the semi-analytical solution presented by Juul (1976)	41
3.17	A representation of a volume zone one sphere diameter per side for a random bed from the bulk region.	42
3.18	Thermal radiation network from surface $i$ (Rousseau et al., 2012).	51
3.19	Combined conduction and radiation network.	53
3.20	Different conduction thermal resistances of the MSUC model (Van Antwerpen et al., 2012).	55
3.21	Different packing regions in a random packed pebble bed.	56
4.1	16x16x4 $D_p$ Enclosure with No Participating Medium	59
4.2	Attenuation factor for various cross-sectional sizes and various radial thicknesses for a simple cubic bed.	60
4.3	A single simple cubic control volume or volume zone with a heated front surface and a cold rear surface.	63
4.4	Temperature plot of the 1x1x1 $D_p$ enclosure comparing the front to rear temperature of the CFD simulation, the subdivided Zonal Approach and the non-subdivided Zonal Approach.	64
4.5	The $30 \times 30 \times 30 D_p$ bed being packed using the DEM solver of Star-CCM+.	66
4.6	The section made from the one wall of the packed bed to derive the radial attenuation factors from the wall. One $0.5 \times D_p$ thick slice is shown on the right.	67
4.7	Empty slice used to calculate the view factor without the spheres present. Notice the holes (colored rings) in the front and rear surfaces.	67
4.8	The view factors obtained from the section cut from the DEM packed bed using ray tracing.	68

4.9	The radial temperature for the 1200K case for the bulk region packed into a $10 \times 10 \times 10D_p$ enclosure for the Zonal Approach with subdivision and the CFD simulation. . . . .	70
4.10	The radial temperature for the 1500K case for the bulk region packed into a $10 \times 10 \times 10D_p$ enclosure for the Zonal Approach with subdivision and the CFD simulation. . . . .	71
4.11	The radial temperature for the 2000K case for the bulk region packed into a $10 \times 10 \times 10D_p$ enclosure for the Zonal Approach with subdivision and the CFD simulation. . . . .	72
4.12	Comparison of the predicted temperature plots for the Zonal Approach and the CFD simulation at the wall and near-wall region for the 1000K case.	72
4.13	Comparison of the predicted temperature plots for the Zonal Approach and the CFD simulation at the wall and near-wall region for the 1000K case.	73
4.14	Comparison of the predicted temperature plots for the Zonal Approach and the CFD simulation at the wall and near-wall region for the 2000K case.	73
4.15	The derived radial attenuation factor for the wall, near-wall and bulk region.	74
4.16	The radial porosity for an annular random packed bed from various experimental and numerical studies (Toit, 2008). . . . .	74
4.17	Basic layout of the NWTCTF (De Beer et al., 2018). . . . .	77
4.18	Comparison between Zonal Approach prediction and NWTCTF experimental results for the 800°C simple cubic bed case. . . . .	78
4.19	Comparison between Zonal Approach prediction and NWTCTF experimental results for the 600°C simple cubic bed case. . . . .	78
4.20	Comparison between Zonal Approach prediction and NWTCTF experimental results for the 800°C simple cubic bed case with reduced solid conduction. . . . .	79
4.21	Comparison between Zonal Approach prediction and NWTCTF experimental results for the 600°C simple cubic bed case with reduced solid conduction. . . . .	79
4.22	Comparison between Zonal Approach prediction and NWTCTF experimental results for the 800°C random-packed bed case. . . . .	81
4.23	Comparison between Zonal Approach prediction and NWTCTF experimental results for the 800°C random-packed bed case with reduced solid conduction. . . . .	81
4.24	Comparison between Zonal Approach prediction and NWTCTF experimental results for the 600°C random-packed bed case. . . . .	82

4.25 Comparison between Zonal Approach prediction and NWTCTF experimental results for the 600°C random-packed bed case with reduced solid conduction. . . . .	82
---	----

# List of Tables

2.1	View factors assigned to the spherical shells surrounding a viewed sphere of 0.06 m in diameter in a random bed in the bulk region. . . . .	12
4.1	Results comparison between Zonal Approach without a participating medium and Star-CCM+. . . . .	59
4.2	Results comparison between the Zonal Approach with and without subdivision of the control volumes and the CFD simulation for a $1 \times D_p$ radially thick simple cubic bed, with a 600K front surface temperature. . . . .	62
4.3	Results comparison between the Zonal Approach with and without subdivision of the control volumes and the CFD simulation for a $1 \times D_p$ radially thick simple cubic bed, with a 1000K front surface temperature. . . . .	62
4.4	Results comparison between the Zonal Approach with and without subdivision of the control volumes and the CFD simulation for a $1 \times D_p$ radially thick simple cubic bed, with a 1500K front surface temperature. . . . .	62
4.5	Results comparison between the Zonal Approach with and without subdivision of the control volumes and the CFD simulation for a $1 \times D_p$ radially thick simple cubic bed, with a 2000K front surface temperature. . . . .	63
4.6	Comparison between results from Zonal Approach and CFD model for various radial thicknesses of a simple cubic bed with a front surface temperature of 600K. . . . .	65
4.7	Comparison between results from Zonal Approach and CFD model for various radial thicknesses of a simple cubic bed with a front surface temperature of 1000K. . . . .	65
4.8	Comparison between results from Zonal Approach and CFD model for various radial thicknesses of a simple cubic bed with a front surface temperature of 1500K. . . . .	65
4.9	Comparison between results from Zonal Approach and CFD model for various radial thicknesses of a simple cubic bed with a front surface temperature of 2000K. . . . .	66

4.10	Results comparison between Zonal Approach with and without subdivision of its control volumes and the CFD simulation for a $10 \times 10 \times 10D_p$ enclosure filled with the bulk region of a random packed bed. . . . .	69
4.11	The results comparison between the Zonal Approach with subdivision and the CFD simulation for the wall and near-wall region for various front wall temperatures. . . . .	71
4.12	The results predicted by the coupled Zonal-MSUC model compared with the NWTCTF experimental results for the simple cubic bed. . . . .	77
4.13	Summarised results for the Zonal-MSUC model predicted heat of the NWTCTF random packed bed experiments. . . . .	80

# List of Abbreviations

<b>CFD</b>	<b>C</b> omputational <b>F</b> luid <b>D</b> ynamics
<b>CSUN</b>	<b>C</b> ylindrical <b>S</b> pherical <b>U</b> nit <b>N</b> odalisation
<b>HTR</b>	<b>H</b> igh <b>T</b> emperature <b>R</b> eactor
<b>MSUC</b>	<b>M</b> ulti <b>S</b> phere <b>U</b> nit <b>C</b> ell
<b>NWTCTF</b>	<b>N</b> ear <b>W</b> all <b>T</b> hermal <b>C</b> onductivity <b>T</b> ransfer <b>F</b> acility
<b>PBMR</b>	<b>P</b> ebble <b>B</b> ed <b>M</b> odular <b>R</b> eactor
<b>RTC</b>	<b>R</b> adiative <b>T</b> ransfer <b>C</b> oefficient
<b>RTE</b>	<b>R</b> adiative <b>T</b> ransfer <b>E</b> quation
<b>SUN</b>	<b>S</b> pherical <b>U</b> nit <b>N</b> odalisation



# Physical Constants

Stephan-Boltzman constant  $\sigma = 5.67 \times 10^{-8} \text{ W/m}^2/\text{K}^4$

# List of Symbols

$A$	Surface Area	$\text{m}^2$
$A$	Matrix containing direct-exchange areas	$\text{m}^2$
$A_{circle}$	Projected area of sphere	$\text{m}^2$
$A_p'''$	Volumetric area density	$\text{m}^{-1}$
$A_{random}$	Effective surface area of a random-packed control volume	$\text{m}^2$
$A_{sphere}$	Surface area of sphere	$\text{m}^2$
$\mathbf{b}$	Vector containing specified heat and temperature	-
$c$	Switch coefficient for specified heat or temperature	-
$D_p$	Sphere diameter	$\text{m}$
$D_{p*}$	Diameter of sphere with reduced size	$\sin$
$E_b$	Black-body radiation	$\text{W}/\text{m}^2$
$F_{i,j}$	View factor from $i$ to $j$	-
$F_{i,j}^{SC}$	View factor from sphere-centered control volume	-
$F_{i,j}^R$	View factor from random control volume	-
$F_{i,j}^0$	Originally calculated view factor used in smoothing procedure	-
$F_{0,k,*}$	Effective view factor from reduced sphere to shell $k$ of SUN model	-
$F_{i,j}^*$	View factor perturbation value used in smoothing procedure	-
$F_e^*$	Radiation exchange factor	-
$\overline{g_i g_j}$	Volume-to-volume direct-exchange area	$\text{m}^2$
$\overline{g_i g_j}^{SC}$	Volume-to-volume exchange from a sphere-centered control volume	$\text{m}^2$
$\overline{g_i g_j}^R$	Volume-to-volume exchange from a sphere-centered control volume	$\text{m}^2$
$\overline{g_i s_j}$	Volume-to-surface direct-exchange area	$\text{m}^2$
$\overline{g_i s_j}^{SC}$	Volume-to-surface exchange from a sphere-centered control volume	$\text{m}^2$
$\overline{g_i s_j}^R$	Volume-to-surface exchange from a random-packed control volume	$\text{m}^2$
$I$	Radiosion intensity	$\text{W}/\text{sr}$
$J$	Radiosity	$\text{W}/\text{m}^2$
$k_{cond}$	Conduction coefficient	$\text{W m}^{-1} \text{K}^{-1}$
$k_{eff}$	Total effective thermal conductivity	$\text{W m}^{-1} \text{K}^{-1}$
$k_{eff}^{rad}$	Effective thermal conductivity due to radiation	$\text{W m}^{-1} \text{K}^{-1}$
$L$	Length	$\text{m}$
$n$	Refractive index	-
$n_{balls}$	number of balls or spheres inside a control volume	-
$\hat{n}$	Unit surface normal	-
$Q$	Nett heat	$\text{W}$
$Q_s$	Nett heat for surface $i$	$\text{W}$
$\dot{Q}$	Heat transfer rate	$\text{W}$
$q$	Heat flux	$\text{W}/\text{m}^2$
$q_s$	Nett heat flux for surface $i$	$\text{W}/\text{m}^2$
$R$	Thermal resistance	$\text{K W}^{-1}$

$r_p$	Radius of pebble or sphere	m
$\bar{r}$	Position	-
$S_{ij}$	Distance from $i$ to $j$	m
$\overline{s_i g_j}$	Surface-to-volume direct-exchange area	m <sup>2</sup>
$\overline{s_i s_j}$	Surface-to-surface direct-exchange area	m <sup>2</sup>
$\overline{s_i s_j}^{SC}$	Surface-to-surface exchange from a sphere-centered control volume	m <sup>2</sup>
$\overline{s_i s_j}^R$	Surface-to-surface exchange from a random-packed control volume	m <sup>2</sup>
$\hat{s}$	Unit vector	-
$T$	Temperature	K
$\bar{T}$	local average temperature	K
$\bar{\bar{T}}$	Average temperature	K
$V$	Volume	m <sup>3</sup>
$V_{cv}$	Volume of control volume	m <sup>3</sup>
$V_{s,cv}$	Volume of spheres inside a control volume	m <sup>3</sup>
$x$	Dimensionless distance; x-coordinate	-
$\mathbf{x}$	Vector containing unknown heat and temperature	-

### Greek Symbols

$\alpha$	Porosity	-
$\beta_{i,j,k}$	Fraction of spherical shell $k$ belonging to $i$ that cuts into $j$	-
$\delta_{ij}$	Kronecker delta	-
$\epsilon_i$	Emissivity of surface $i$	-
$\epsilon_p$	Porosity	-
$\epsilon_{R,1}$	error value	-
$\kappa$	Attenuation factor	-
$\lambda$	Wavelength, lagrangian multiplier	m, -
$\Psi$	Azimuth angle	rad
$\theta$	Angle	rad
$\Omega$	Solid angle	sr

*This is dedicated to my wife, Bernice. Your love inspires me  
to go beyond what I thought was possible.*

# 1 Introduction and Background

## 1.1 Introduction

Although the South-African Pebble Bed Modular Reactor (PBMR) project stopped research and development on packed pebble bed reactors, South Africa remains at the forefront of international research on packed pebble bed reactors by continuing research efforts in the field by among others Van Antwerpen (2009), Pitso (2011), Rousseau et al. (2014) and De Beer et al. (2018). The construction of the HTR-PM (shown in figure 1.1), the upscaled version of the Chinese HTR-10, ensures renewed interest in packed pebble bed reactor research (Asakuma et al., 2014).

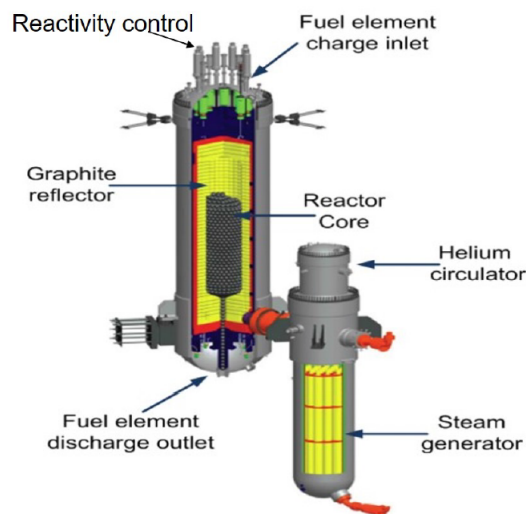


FIGURE 1.1: A simplified illustration of the Chinese HTR-PM demonstration pebble bed nuclear reactor (Dong, 2018).

The Fukushima Daiichi Nuclear Disaster highlighted the importance of nuclear safety, and the importance of being able to model a nuclear reactor under diverse conditions. The effective thermal conductivity is a crucial parameter in the inherent safety of a packed pebble bed gas cooled reactor. The effective conductivity consists of four distinct components:

1. conduction through the solids;

2. conduction through the contact areas between spheres and the spheres and the walls;
3. conduction through the stagnant gas phase;
4. thermal radiation between the solid surfaces.

The conduction and convection components of the effective thermal conductivity have been properly addressed by Van Antwerpen (2009), but the radiation component wasn't addressed entirely satisfactorily. The role of the thermal radiation inside a packed bed at low temperatures is not as important as that of conduction and convection. However at high temperatures, the temperatures at which the packed pebble bed gas cooled reactors operate, the thermal radiation plays an equally and perhaps even a dominant role in the total heat transfer in the bed (Van Antwerpen, 2009).

The effective thermal conductivity is based on the well-known Fourier conduction equation with the bed, modelled as a porous medium, subdivided into control volumes with adjacent control volumes. The equation is given by Rousseau et al. (2014):

$$\dot{Q} = -k_{eff} A \frac{dT}{dx} \quad (1.1)$$

The thermal radiation component of the effective thermal conductivity is given by (Rousseau et al., 2014):

$$k_{eff}^{rad} = 4F_e^* \sigma D_p \bar{T}^3 \quad (1.2)$$

with  $F_e^*$  the radiation exchange factor,  $\sigma$  the Stephan-Boltzman constant,  $d_p$  the sphere diameter and  $\bar{T}$  the average temperature between the two adjacent control volumes. It can be seen from eq. [1.2] that the preferred method is to use the local averaged temperature, which is only valid for small temperature differences between the respective control volumes. It also only takes into account the temperature gradient between cells that are directly adjacent to one another. Empirical data suggests that the radiation heat transfer is a strong function of both the local temperature level and the macro temperature gradient through the bed. The existing approach does not capture this effect sufficiently, which implies that a different approach should be used (Rousseau et al., 2014).

## 1.2 Model Selection

The Multi-Sphere Unit Cell (MSUC) model was developed by Van Antwerpen (2009) to address the shortcomings of other effective thermal conductivity models, especially in the wall- and near-wall regions of a packed pebble bed reactor, by applying a more fundamental approach. The MSUC model consisted of a summation between the conduction and radiation terms of the effective thermal conductivity. The MSUC model incorporated both

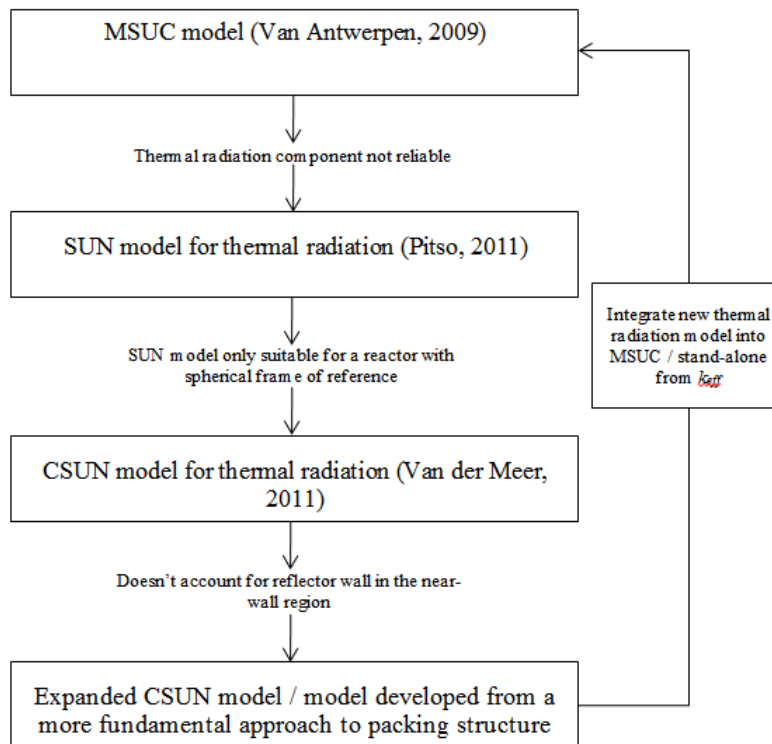


FIGURE 1.2: Diagram illustrating the development of the thermal conductivity models from the MSUC model with emphasis on the thermal conductivity due to thermal radiation.

short- and long-range thermal radiation in its model, but the long long-range component was still unrefined and not suitable for high-temperature applications. Pitso (2011) identified this shortcoming in the long-range radiation component from the MSUC model and developed the Spherical Unit Nodalisation (SUN) model to better describe the long-range radiation. Van der Meer (2011) succeeded to implement the SUN model in a cylindrical or annular system by developing the Cylindrical Spherical Nodalisation method, or CSUN method. The SUN model was further developed by adapting it to be implemented using a generic methodology for the bulk region of a random-packed bed (Rousseau et al., 2014). The development in its current form stopped due to questions regarding the validity of implementing radiation that was adapted from a sphere-centered system (as done by Rousseau et al. (2012)) to a generic random-packed bed. Figure 1.2 illustrates the development of the radiation component of the MSUC model.

An improved formulation for the thermal radiation component of the MSUC model is required. The model must solve the radiation heat transfer inside a packed pebble bed reactor and need to be able to solve sufficiently fast for a full-sized reactor; it needs to be applied to generic geometries without re-evaluating the geometry each time; and it needs to be sufficiently accurate on a systems-level approach. The reactor solution model must

be able to solve porous media as part of a network. The model must also take long distance radiation into account, including in the near-wall region. The model must be coupled with the MSUC model by replacing the current thermal radiation component used in this model.

The Zonal Approach could be a suitable choice to solve the radiation heat transfer inside a packed pebble bed reactor. Its coarse mesh as well as its known use on a systems-level approach to model radiation heat transfer inside furnaces ensures it is an applicable model for this purpose. However its current difficulty to calculate the direct-exchange areas for more complex geometries will limit its application for generic geometries.

It will then be necessary to characterise the view factors inside a packed bed before applying it to the direct exchange areas in the zonal method. This characterisation can be done by using the Monte Carlo Ray Tracing method and can be applied for various geometries with the same packing structure (i.e. random, simple cubic etc.) and the same size pebbles. This preceding characterisation should enable the zonal method to be applied to generic simple and complex geometries without over-complicating it.

### **1.3 Problem Statement**

Long range thermal radiation inside a packed pebble bed nuclear reactor is an important physical phenomenon, but is not properly accounted for in existing simulation models, especially in the near-wall region. Therefore, an improved model for the thermal radiation in a packed pebble bed reactor needs to be developed to account for the macroscopic temperature gradient through the bed that influences the long range radiation. It should also be able to accommodate the wall and near-wall regions of a packed pebble bed.

### **1.4 Hypothesis**

It is possible to model the thermal radiation inside a packed pebble bed nuclear reactor accurately and efficiently with the Zonal Approach coupled with the Monte Carlo Ray Tracing Method for pre-processing of the direct exchange areas for generic geometries. It is also possible to take the wall region and near-wall region into account in the Zonal Approach.

### **1.5 Methodology**

This study will first identify which parts of the Zonal Approach must be adapted to enable it to solve thermal radiation inside a pebble bed. The identified parts will then be adapted



and discussed and the pebble bed will be characterised to enable thermal radiation modeling inside the bed. For the current study, a pebble bed will refer to a bed packed with mono-sized spheres. The evaluated packing structures will be the simple cubic structure and a random packed bed. The regions that will be evaluated will include the wall region, the near-wall region and the bulk region. This newly derived Zonal Approach will first be compared with simulation results of thermal radiation only; thereafter the derived thermal radiation model will be combined with the Multi-Sphere Unit Cell model's conduction component which will be compared with test results from the Near-Wall Thermal Conductivity Test Facility (NWTCTF) from De Beer (2014).

## 1.6 Contributions of this Study

This study will present a new thermal radiation model for modelling long-range thermal radiation inside a pebble bed. The Zonal Approach will be adapted to accommodate thermal radiation inside a pebble bed filled with mono-sized spheres. The direct exchange areas will be adapted for both a structured and a random-packed pebble bed. The attenuation factor for both these packing structures will be derived and tested. This study will also investigate the practicality of adapting the Zonal Approach for modeling the thermal radiation inside a pebble bed by coupling it with the conduction component of the MSUC model and comparing it with the NWTCTF test results. The applicable control volume (zone) sizing will also be discussed.

## 1.7 Chapter Layout

Following this chapter, Chapter 2 will discuss the different approaches of modeling thermal radiation as well as more specifically discussing the thermal radiation models for pebble beds. It will also discuss the initial progress made with the SUN model at the start of this study. Chapter 3 will discuss the Zonal Approach in more depth as well as adapting it for use with beds with mono-sized spheres. In Chapter 4 the attenuation factors will be derived for both a structured simple-cubic pattern and a random packing after which the thermal radiation model of the adapted Zonal Approach will be compared with simulation results from an industry-standard multi-physics solver Star-CCM+. The modified Zonal Approach will also be coupled with the conduction component of the MSUC model and compared with test results from the NWTCTF. In Chapter 5 a brief overview of the achieved work will be given and conclusions and recommendations for future study will be given.

## 2 Thermal Radiation in a Packed Pebble Bed

### 2.1 Introduction

In this chapter an overview of the different thermal radiation modeling approaches will be given. The shortcomings of the current thermal radiation component of the Multi-Sphere Unit Cell (MSUC) model will be addressed, the Spherical Unit Nodalisation (SUN) model together with its developments will be discussed and the reasons behind selecting the Zonal Approach will be given.

### 2.2 Background

A distinct feature of the gas-cooled pebble bed reactor is its inherent safety due to its self-acting decay heat removal chain. The effective thermal conductivity forms part of this heat removal chain which makes it of utmost importance to describe the effective thermal conductivity through the packed pebble beds, as accurately as possible. The MSUC model was developed by Van Antwerpen (2009) to address the conduction and radiation in a packed pebble bed in a more fundamental way. While the conduction component of the MSUC model was satisfactory, the thermal radiation component still didn't properly address the long-range radiation in the bed (Rousseau et al., 2012).

#### 2.2.1 Different Approaches to Model Radiation Heat Transfer

##### 2.2.1.1 Overview

Van Antwerpen et al. (2010) gave a quite comprehensive literature survey on the different methods for simulating radiative heat transfer and grouped it into three approaches:

1. Radiative Transfer Equation (RTE) approach
2. Unit Cell method approach
3. Radiative Transfer Coefficient (RTC) approach

The RTE approach requires an energy balance equation for the emitting, absorbing and scattering medium. It also requires a set of optical properties (such as the scattering coefficient, absorption coefficient etc.) that must first be obtained. The optical properties can either be obtained experimentally or numerically. According to Van Antwerpen et al. (2010), the RTE was explained by considering the two-flux model, but the two-flux model produced unrealistically low values of emissivity compared to the Monte Carlo diffuse model. According to Viskanta and Menguc (1987), the RTE forms the basis for the quantitative study of the transfer of radiant energy in participating media. The solution for even a simple one-dimensional, planar, grey medium can be quite difficult, while most engineering systems are multidimensional. Even the spectral variation of radiative properties must be accounted for in the solution of the RTE if its prediction is to be accurate. This proves the necessity of simplifying assumptions for each application, which leads to different solution techniques regarding the different simplifying assumptions. This theory is suitable for modelling heat transfer in a reactor and different solution approaches of this theory have already been used to model heat transfer in various types of reactors. The main solution approaches are: ray tracing, flux models and zonal type models.

The Unit Cell method approach makes use of repeated units of idealised geometry with predetermined optical properties. The energy distribution for the system can thus be formulated as a set of simple algebraic equations. The general term for the thermal radiative conductivity for a unit cell in a packed bed is recalled from eq. [1.2] as:

$$k_{eff}^{rad} = 4F_E^* \sigma d_p \bar{T}^3 \quad (2.1)$$

with  $F_E^*$  the radiation exchange factor,  $\sigma$  the Stephan-Boltzman constant,  $d_p$  the sphere diameter and  $\bar{T}^3$  the average temperature between the two adjacent control volumes.

Fundamenski and Gierszewski (1991) stated that the well-known Zehner-Bauer-Schlunder model used the bed porosity as the main scaling parameter and therefore did not assume particle arrangement or packing. It also incorporated parameters such as the Smoluchowski effect, thermal radiation transfer and contact area. Van Antwerpen et al. (2010) noted that the unit cell from the Zehner-Bauer-Schlunder model assumed that it was closed and didn't take radiation from the voids outside the unit cell into account, ignoring long-range radiation.

According to Van Antwerpen et al. (2010), Strieder stated that  $k_{eff}^{rad}$  only remained valid as long as could be assumed that the steady state temperature drop across the local averaged bed is much smaller than the average bed temperature. This approach is limited by the value of  $F_E^*$  that cannot be calculated easily, which led some researchers to state that this simple approach is inaccurate.

The RTC approach is a numerical method that provides the average temperature solutions as fine as the size of the spheres. The RTC is a function of the microstructure (coordination number, area of contact and the distance between the centres of the spheres) and the radiative properties of the packed sphere system. In the RTC approach, a set of algebraic equations is first established to calculate the energy in each sphere. With a known energy distribution, each sphere's temperature can be calculated. The RTC is calculated using a Monte Carlo Ray-Tracing method. With the RTC known, the algebraic equations can be solved iteratively (Van Antwerpen et al., 2010).

Viskanta and Menguc (1987) reported two independently developed and conceptually distinct theories in modelling the propagation and interaction of electromagnetic radiation with matter:

1. The classical electromagnetic wave theory
2. Radiative transfer theory

The classical electromagnetic wave theory looks at the propagation and interaction of radiation with matter at a microscopic point of view, and this fundamental approach can be used to predict the macroscopic properties for the media which can be used as coefficients in the radiative transfer equation. The radiative transfer theory looks at the propagation and interaction of radiation with matter at a macroscopic level. The radiative transfer theory is concerned with the quantitative study on the phenomenological level of the interaction of radiation with matter that absorbs, scatters and emits radiant energy (Viskanta and Menguc, 1987).

The radiation transfer theory is simpler than the electromagnetic wave theory due to the fact that the radiative transfer theory ignores the wave nature of radiation and describes it in terms of geometric optics which is the study of electromagnetism in the limiting case of extremely short wavelengths (relative to the bodies it interact with) or high frequency. The RTE forms the basis for modeling radiant energy in a participating medium (Viskanta and Menguc, 1987).

According to Viskanta and Menguc (1987) the solution of radiative transfer equation can be sub-divided into roughly four groupings:

1. Exact solutions
2. Statistical approaches
3. Flux models
4. Network-type approaches

### 2.2.1.2 Exact Solutions to the RTE

The exact solution for the RTE require certain simplification assumptions, such as uniform radiative properties of the medium and homogeneous boundary conditions. Altaç and Tekkalmaz (2011) modelled a cubic enclosure containing an absorbing, emitting and anisotropically scattering homogeneous medium while Liemert and Kienle (2011) modelled an infinitely extended and anisotropically scattering medium which compared exactly to a Monte-Carlo solution. Viskanta and Menguc (1987) reported various exact solutions to the RTE but concluded that, apart from serving as benchmarks for the accuracy of other models for simple geometries, these models are too impractical for engineering problems.

### 2.2.1.3 Statistical Approach

The ray tracing approaches are statistical approaches which traces emitted radiative energy bundles until they are absorbed or exit the system. A good example of this approach is the Monte Carlo Ray Tracing approach such as Kovtanyuk et al. (2012) who proposed a modified Monte-Carlo algorithm for the solution of nonlinear coupled radiative-conductive heat transfer problems. These approaches are highly accurate, comparable to exact solutions, but due to its statistical nature, statistical errors can arise which can lead to non-convergence. These approaches are suitable for highly complex geometries, but ray tracing needs to be done for each geometry being evaluated and it has a very high computational cost.

### 2.2.1.4 Flux Models

These models use a direct solution of the RTE by subdividing the directional variation into a small number of angles in which the radiation intensity is assumed to be constant. It uses a CFD fine mesh and diffuse radiation heat transfer between neighbouring cells. The radiation interaction is only between neighbouring cells, which are modelled as part of an effective thermal conductivity term. Cells are much finer than those used in the Zonal method, which accounts for its high computational cost. This approach is widely used in the engineering community in the solution of radiation inside boiler furnaces.

The flux models enjoy the most wide-spread use in modeling the conductive and radiative heat transfer inside reactors due to its integration in CFD simulation packages. Examples of the flux models are the discrete ordinate method, discrete element method and the finite volume method. The CFD package Fluent as well as CD-Adapco's Star-CCM+ code use the Discrete Ordinate Method to solve radiative heat transfer in participating media (Fluent, 2001) (CD-Adapco, 2014).

Kim (2008) recommends the use of the finite volume method for the solution of radiative heat transfer in an axisymmetric cylindrical geometry with an absorbing, emitting and scattering medium. Asakuma et al. (2014) applied a homogenisation method to a packed pebble bed to define a periodic domain for each unit cell, and applied the finite element method to solve the derived cell problem for the effective thermal conductivity in the bed. The thermal radiation heat flux is only considered between neighbouring particles. Ruan et al. (2006) developed a model to solve the coupled radiative-conductive heat transfer in participating media for rectangular, cylindrical and annular enclosures, by using a finite element approach with an unstructured mesh.

The shortcoming of only taking thermal radiation between neighbouring particles into account by Asakuma et al. (2014) was partially addressed by Wu et al. (2016) who proposed using Voronoi polyhedra for models incorporating short- and long-range radiation respectively. The short-range model only incorporated adjacent Voronoi polyhedra, ignoring long-range radiation. It was found to be useful in calculating the thermal radiation in beds of temperatures below 1215°C due to its over-prediction of the solid conductivity and under-prediction of the view factors between polyhedra. In general, it was found to be unsuitable for materials with large conductivities (relative to the radiation component of the effective thermal conductivity) and with a non-dimensional solid conductivity of less than 10. The long-range radiation model used Monte Carlo Ray-Tracing to obtain the view factors between the polyhedral surfaces and in general provided a more accurate model for calculating thermal radiation due to its incorporation of radiation exchange between all possible competing spheres. However, this model can only be applied when the dimensionless surface conductivity is larger than 10 or when the material had a large conductivity. A correction of the long-range model was suggested.

Wu et al. (2017) remedied the shortcoming of the short-range radiation model's accuracy in modelling the thermal radiation at higher temperatures by modifying the short-range radiation heat transfer equation for temperatures above 1400K. This modified radiation model was used in conjunction with a CFD-DEM model to provide a complete model which considered particle motion, fluid flow, particle-fluid interactions and heat convection, conduction and radiation.

The explicit model presented by Wu et al. (2016) and Wu et al. (2017) to model the thermal radiation inside a packed pebble bed can be replaced by an implicit control volume-based model to model both the short-range and long-range radiation. The Zonal Approach is suggested since this approach not only takes the small temperature differences between respective control volumes into account, but also the temperature gradient between non-adjacent cells (long-range radiation). A random packed pebble bed can be characterised with Monte Carlo ray tracing from which an attenuation function is derived, which can

then be exported to the Zonal Approach. The Zonal Approach was originally developed for use in coal-fired furnaces, but it will be shown that it can be applied to a pebble bed, as well to effectively account for both the short-range and long-range radiation in generic random packed pebble beds.

### 2.2.1.5 Network-type Approaches

Network-type approaches typically subdivide an enclosure filled with a porous medium into zones and connect each zone to the other by means of thermal resistances. From this a matrix of the exchange is formed and solved via matrix inversion to obtain the temperatures and heat of each zone, depending on what was specified. Examples of a network-type approach is the SUN-model (Pitso, 2011) and the Zonal Approach (Hottel and Cohen, 1958).

## 2.3 The Multi-sphere Unit Cell (MSUC) Model

It was demonstrated by Van Antwerpen (2009) that porosity alone was not enough to quantify randomly packed beds. Therefore Van Antwerpen proceeded to develop the MSUC model from a more fundamental approach by comparing the radiation in a packed bed to the radiation between two diffuse, grey parallel plates. The MSUC model described the packing structure more accurately, especially in the near-wall region.

The effective thermal conductivity is a characterisation of an arrangement of solid-fluid/gas mediums and not a thermo-physical property. This led to that most of the research on the simulation of the heat transfer coefficient was done in the bulk region of the reactor, since the structure is mostly uniform and the characteristics of the solid-fluid/gas mediums are simpler than in the near-wall region. It has been shown that the porous structure in a pebble-bed reactor varies significantly near the wall due to the disruption of the packing geometry in this region (Van Antwerpen, 2009).

It is important to model the heat transfer in the near-wall region as accurately as possible, because of two reasons (Van Antwerpen, 2009):

1. The control rod reactivity housed in the reflectors is highly temperature dependent;  
and
2. The pebble-to-reflector interface is on the critical path for the decay heat removal under accident conditions.

Van Antwerpen (2009) presented the MSUC model to simulate the effective thermal conductivity, which incorporated seven distinct components of the effective thermal conductivity. The MSUC Model described the effect of the packing structure more fundamentally,

TABLE 2.1: View factors assigned to the spherical shells surrounding a viewed sphere of 0.06 m in diameter in a random bed in the bulk region.

Shell #	Boundaries [ $\times D_p$ ]	View Factor $F_{0,j}$
0	$0.0 < r < 0.5$	0
1	$0.5 < r < 1.0$	0.5010
2	$1.0 < r < 1.5$	0.3207
3	$1.5 < r < 2.0$	0.1294
4	$2.0 < r < 2.5$	0.0342
5	$2.5 < r < 3.0$	0.01058
6	$3.0 < r < 4.5$	0.0040
7	$r = 4.5$	0.0001

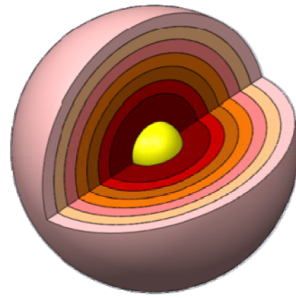


FIGURE 2.1: The shells surrounding the viewed sphere demarcating the view factors allocated to the surround spheres.

which renders it ideal as a basis for further development of the effective thermal conductivity. It was employed for both the bulk and near-wall conditions and attempts to minimise the empirical nature of the previously used correlations. The MSUC Model is a summation of the thermal conduction and the thermal radiation.

The thermal radiation component is sub-divided into short-range thermal radiation and long-range radiation. Although the MSUC model distinguished between short-range and long-range radiation, the long-range component as modelled by Van Antwerpen (2009) was unrefined and thus unsuitable for high-temperature applications. The SUN-model was initially proposed as a replacement to the thermal radiation component of the MSUC model (Rousseau et al., 2014) in order to combine the short-range (adjacent/touching spheres) and long-range (non-adjacent) radiation but due to it being a sphere-centered approach it wasn't suitable for use as a control volume-centered approach in a random bed, at least not in its current form. The SUN-model was based on the concept that the spheres surrounding a viewed sphere could be grouped into concentric shells (shown in figure 2.1) which determined the exchange attributed to the surrounding spheres. The view factors associated with the shells surrounding the viewed sphere is given in Table 2.1 .



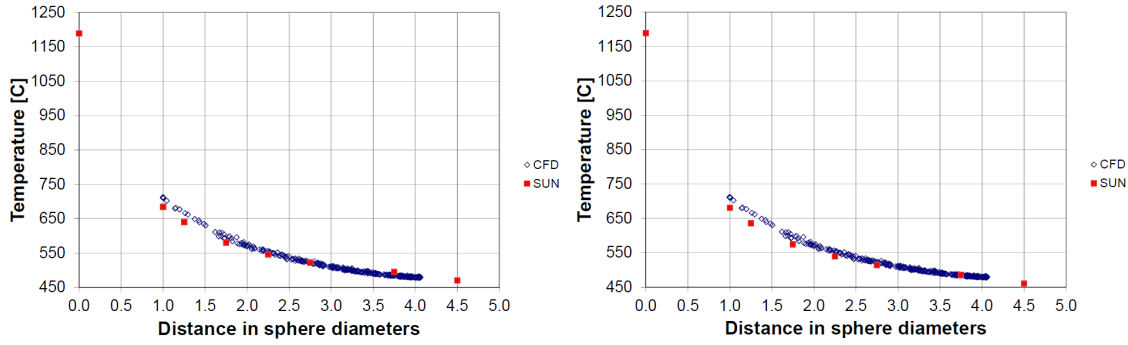


FIGURE 2.2: Comparison of SUN results to CFD simulation for a fixed central sphere temperature and enclosure boundary heat removal rate (left) and fixed central sphere and enclosure temperature (right).

The SUN model was compared to a CFD simulation of a large hollow spherical enclosure  $9 \times D_p$  in diameter, filled with pebbles from the bulk region of a packed pebble bed. The diameter of the pebbles were slightly reduced from 60mm to 59mm around the same centroids to eliminate contact. The conduction of each pebble was made extremely high ( $k_{cond} = 10\,000\text{W/m/K}$ ) to ensure isothermal surfaces of each pebble and a pebble at the center of the enclosure was heated to  $1189^\circ\text{C}$  while a heat extraction rate of  $1946.8\text{W}$  was uniformly distributed around the outer spherical shell surface. The results were found to be within 4% of the CFD results when a fixed temperature for the central pebble and the enclosure heat removal rate were specified while the results were within 0.4% when the central pebble and the enclosure temperature were specified. The results are summarised in figure 2.2. More detail regarding this study can be found in Rousseau et al. (2012).

The SUN model was adapted by Van der Meer (2011) to accommodate a cylindrical coordinate system, and the modified model was dubbed the CSUN model. It was tested against measured results from the High Temperature Test Unit (HTTU) testing facility, but only for the bulk region of the bed. The inlet and outlet planes for the model were 'sectioned' from the HTTU results and the values at that sections used as input and output values. A section from a typical annular packing is shown together with specifications of the CSUN model used to compare against the HTTU results in figure 2.3 while the comparison of the results is shown in figure 2.4. The CSUN results compared favourably with the HTTU test results for two different cases although it was under  $1000^\circ\text{C}$  and thus not at very high temperatures, which was one of the aims of the study. The CSUN was also compared to other heat transfer models for theoretical cases of the HTTU up to  $1600^\circ\text{C}$ .

### 2.3.1 The Current Study's Initial Progress with SUN Model

The SUN model still needed to be adapted for generic applications of a packed bed, since the current SUN model was sphere-centered. After further development the SUN model as

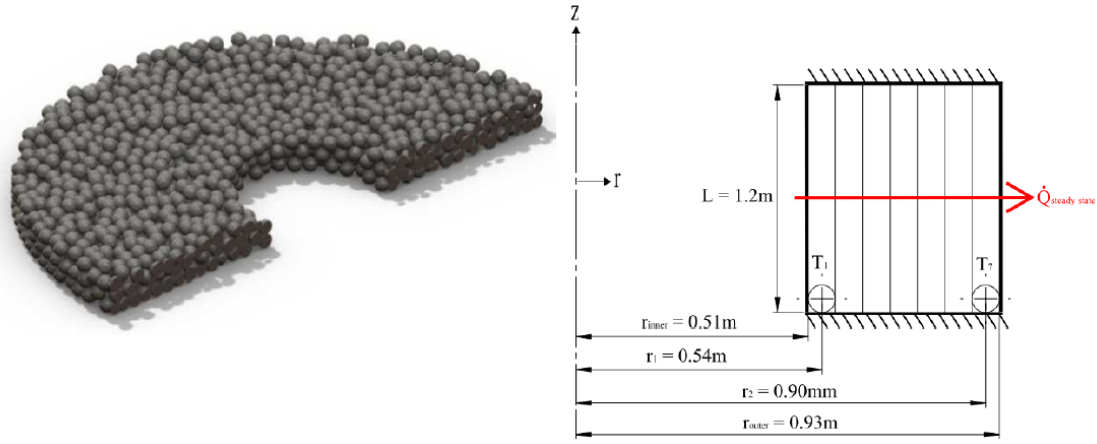


FIGURE 2.3: A typical section from an annular packed bed (left) and the CSUN model setup of the HTTU (Van der Meer, 2011).

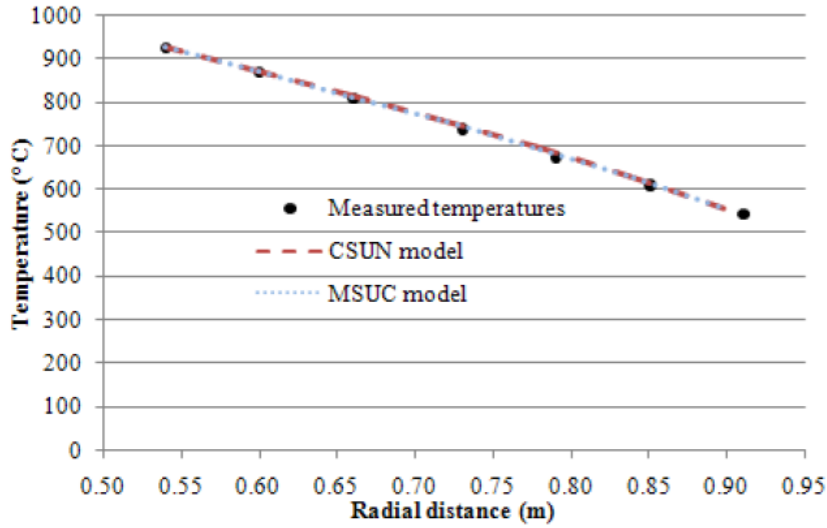


FIGURE 2.4: Results comparison between the CSUN model and the HTTU test in the bulk region for the 82.7kW case (Van der Meer, 2011).

presented by Pitso (2011) and Rousseau et al. (2012) was adapted for generic application in a random bed. The computational grid was adjusted to accommodate a generic bed where a sphere will not necessarily be at the center of the focus area (as shown in figure 2.5), with the assumption that the packing density would remain the same. The volumetric area density was adapted to:

$$A_p''' = (1 - \varepsilon_p) \frac{6}{D_p} \quad (2.2)$$

The view factor from generic zone  $i$  to generic zone  $j$  was derived as:

$$F_{i,j} = \frac{\pi}{6(1 - \varepsilon_p)} \frac{D_{p*}^2}{D_p^2} \sum_{k=1}^7 (\beta_{i,j,k} F_{0,k*}) \quad (2.3)$$

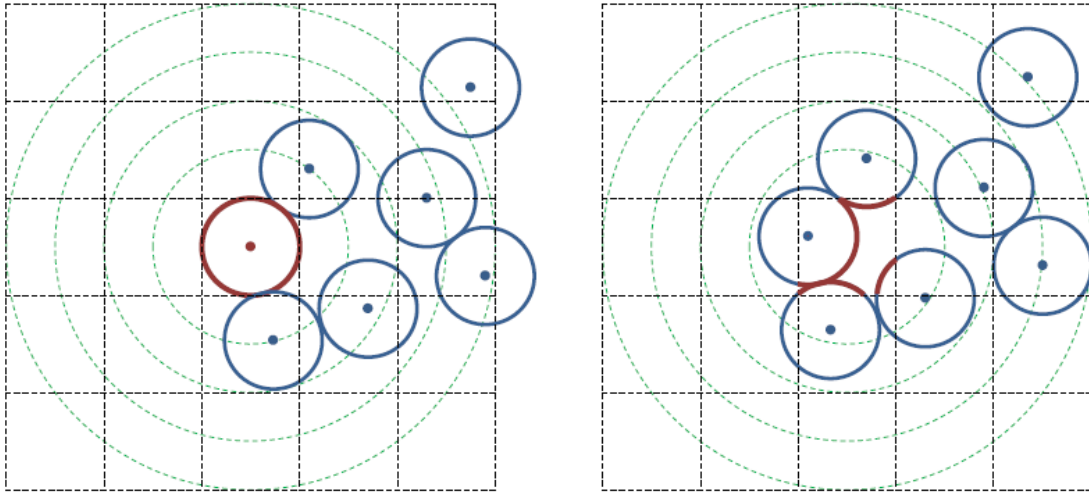


FIGURE 2.5: Demonstration of the computational grid with a sphere-centered control volume (left) and a generic control volume (right).

If a bulk porosity of 0.39 was implemented into eq. [2.3] it was revealed that the sum of the view factors did not sum to 1, but rather to  $\approx 0.83$  indicating that there was internal radiation (radiation from the spheres inside the control volume onto itself) present. This was logical considering the generic control volume shown in figure 2.5. The derived direct exchange factor for any generic control volume  $i$  radiating to any other generic control volume  $j$  in the bulk region can be calculated using:

$$A_i F_{i,j} = \frac{\pi D_p^2}{D_p^3} V_{CV} \sum_{k=1}^7 (\beta_{i,j,k} F_{0,k*}) \quad (2.4)$$

The results of this modified SUN model was compared to the results of the same CFD simulation as was used in Rousseau et al. (2012), with the results shown in figure 2.6. Two cases were simulated: The first case where the central zone's temperature and the enclosure's heat are prescribed and the second where both the central source and the enclosure's temperature are prescribed. Both cases were within four percent of the CFD results based on its temperature profile and within one percent based on its heat results.

A smoothing algorithm was also developed to smooth out the errors caused by subdivision of the enclosure to ensure adherence to the reciprocity rule. The procedure required perturbation values for each exchange to be added to the originally calculated view factor value using eq. [2.3]:

$$F_{i,j} = F_{i,j}^0 + F_{i,j}^* \quad (2.5)$$

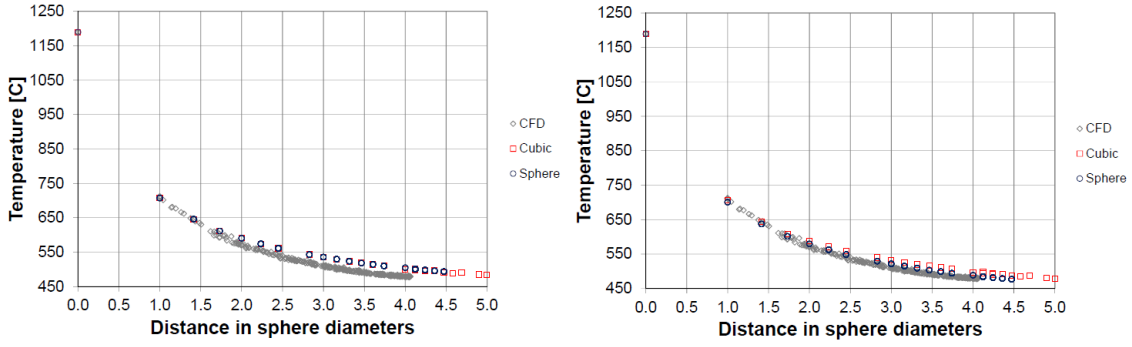


FIGURE 2.6: The results of the adapted SUN model compared to CFD results with the inner temperature and enclosure heat prescribed (left) and for inner and enclosure temperature prescribed (right).

With eq. [2.5] forcing reciprocity for each exchange, as given in eq. [2.6]

$$A_i F_{i,j} = A_j F_{j,i} \quad \forall \begin{pmatrix} i = 1, n \\ j = 1, n \end{pmatrix} \quad (2.6)$$

The view factors of a control volume onto itself need not be considered which gives  $m = \sum_{ii=1}^{n-1} ii$  errors squared, and with eq. [2.5] into eq. [2.6] the following algorithm is obtained:

$$\varepsilon_{R,l}^2 = [A_i (F_{i,j}^0 + F_{i,j}^*) - A_j (F_{j,i}^0 + F_{j,i}^*)]^2 \quad \forall \begin{pmatrix} i = 1, n-1 \\ j = i+1, n \end{pmatrix} \quad (2.7)$$

With  $l = \sum_{k=1}^{i-1} (n-k) + j - i$ . In order to minimise the sum of all reciprocity errors squared  $\sum_{l=1}^m \varepsilon_{R,l}^2$  we need to find  $n(n-1)$  values of  $F_{i,j}^*$  by solving  $n(n-1)$  linear equations of the form

$$A_i^2 F_{i,j}^* - A_i A_j F_{j,i}^* = -A_i^2 F_{i,j}^0 + A_i A_j F_{j,i}^* \quad \forall \begin{pmatrix} i = 1, n \\ j = 1, n \\ j \neq i \end{pmatrix} \quad (2.8)$$

The error redistribution algorithm ensured faster convergence for larger subdivisions of the control volumes saving considerable simulation time. This is demonstrated in figure 2.7.

Although the initial generic implementation looked promising it was decided to abandon further development of the model due to questions regarding the validity in applying view factors derived from a sphere-centered emitting system to a generic system. Since the ease and accuracy of the SUN network approach showed promise, it was decided to pursue

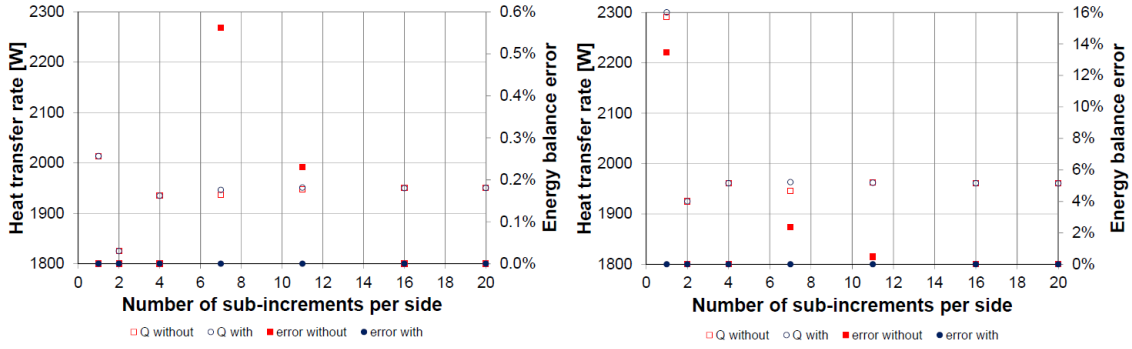


FIGURE 2.7: The results using the error redistribution procedure for the cubic model case (left) and the near-spherical model case (right)

another network-based approach but without the pitfalls of the SUN approach, namely the Zonal Approach.

It must also be noted that Cheng and Yu (2013) developed a model which calculated the effective thermal conductivity in a packed pebble bed using the Voronoi network model. Their model, however, only included radiation heat transfer to adjacent particles which meant that long range radiation was not taken into account. The SUN model can be suitable for implementation into such an approach since it keeps the sphere-centered approach for each control volume.

### 2.3.2 The Zonal Approach

The Zonal Approach is in principle better suited for use in a random bed where the location of each ball is not necessarily known but where the bed properties like porosity, emissivity etc. is known. In the Zonal Approach the enclosure and the medium is divided into isothermal zones, and the exchange of each zone to all the other zones is calculated and noted in a matrix. The radiative transfer equation is then reduced to the form:

$$Ax = b \quad (2.9)$$

With  $A$  the matrix containing the direct exchange areas,  $x$  the vector containing the unknowns to be solved and  $b$  the specified conditions which is either the blackbody radiation  $E_{bi}$  if temperature is specified or  $Q_i$  if heat is specified. The Zonal Approach is already widely used in engineering solutions for calculating radiant heat transfer as is noted in Viskanta and Menguc (1987) and Bordbar and Hyppänen (2007) but no publication could be found where it has been attempted to apply it to a packed pebble bed filled with mono-sized spheres.

The Zonal Approach was originally introduced by (Hottel and Cohen (1958)). Some of the model's key features are:

- The surface and volume of the enclosure is divided into zones, each having a uniform distribution of the temperature and radiation properties;
- The direct exchange areas between the surface and volume elements are evaluated to obtain the total exchange areas;
- This approach accounts for the radiative interaction between all of the cells in the system;
- It has a much shorter solution time than the flux models and the ray tracing approaches;
- This method is difficult to incorporate in complex geometries, due to the number of different direct exchange areas which are unique to the geometry that will arise;
- The main application of the Zonal Approach is to model the thermal radiation inside boiler furnaces. Figure 2.8 shows an example of a furnace subdivided into surface and volume zones. Note the relatively large zones.

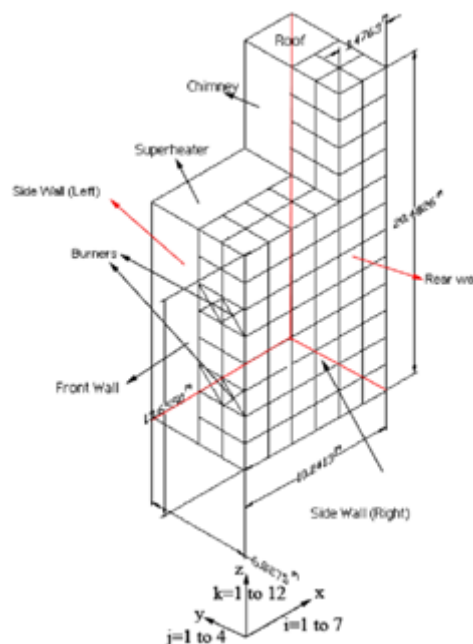


FIGURE 2.8: An example of the application of the Zonal Approach to a furnace, with the surface and volume zones shown (Bordbar and Hyppänen, 2007).

The Zonal Approach will be discussed in more detail in the next chapter.

## **2.4 Summary**

In this chapter an overview of the different thermal radiation modeling approaches was given. The shortcomings of the current thermal radiation component of the Multi-Sphere Unit Cell (MSUC) model was discussed, the Spherical Unit Nodalisation (SUN) model together with its developments was discussed and the reasons behind selecting the Zonal Approach was given.

## 3 The Zonal Approach Applied to a Packed Pebble Bed

### 3.1 Introduction

The Zonal Approach (or zonal model, zonal method) is a network-type approach in which a participating medium is fully enclosed in an enclosure, and in the absence of a participating medium there will only be an enclosure. The enclosure is then divided into  $N$  surface zones and the participating medium (if present) is then divided into  $K$  volume zones. The exchange between all the zones is then calculated using direct exchange areas, and these direct exchange areas are then implemented in solving the unknown heat fluxes or zone temperatures. It was originally developed to solve the thermal radiation in coal-fired furnaces (Modest, 2003). In the first section of this chapter the basic Zonal Approach will be discussed, and in the next section its implementation for a packed pebble bed will be shown. First the direct-exchange areas for an enclosure with a participating medium will be derived and then the energy balance necessary to solve the system of equations to obtain the heat transfer in the system will be given.

After discussing the basic principles and direct exchange areas of the Zonal Approach it will be adapted to a bed filled with mono-sized spheres. This will include an enclosure filled with spheres organised in a structured fashion as well as a random packed bed. The main difference between a coal-fired furnace and a random packed bed is the transmissivity of the bed. The pulverised fuel inside a coal fired furnace is very fine, typically smaller than  $50\text{ }\mu\text{m}$ , has a low volume fraction and subsequently has a low attenuation factor. The packed pebble bed, with comparatively large particle sizes of 60mm in diameter, is very densely packed and subsequently has a large attenuation factor. Since the zonal approach was originally intended for use with transparent and semi-transparent porous media, the applicability of the use of an attenuation factor to represent the energy absorption through the bed will be investigated in the following sections. The direct exchange areas between surface and volume zones will be derived for a packed pebble bed with mono-sized spheres.



## 3.2 Background

The zonal approach was first developed by Hottel and Cohen (1958) and is used to calculate radiation heat transfer and temperature distribution in a system containing an enclosure filled with an absorbing, emitting and scattering medium. It is a numerical approach which is an extension of the net radiation method for surface exchange. The system is subdivided into a finite number of elements or zones, where the surface and volume zones' dimensions must be such that each zone can be assumed isothermal. The radiation exchange between two zones is given by direct exchange areas (DEA), which represent the system's optical and geometric properties. Using the DEA an energy balance for the radiation exchange is performed for each zone. This leads to a set of simultaneous equations for the unknown temperatures and heat fluxes which can be solved by matrix inversion. The Zonal Approach is normally used to calculate the heat transfer inside coal fired furnaces or similar systems, where the participating medium is a gray diffuse and scattering gas (Howell and Siegel, 1992; Modest, 2003; Viskanta and Menguc, 1987).

## 3.3 Radiative exchange without a participating medium

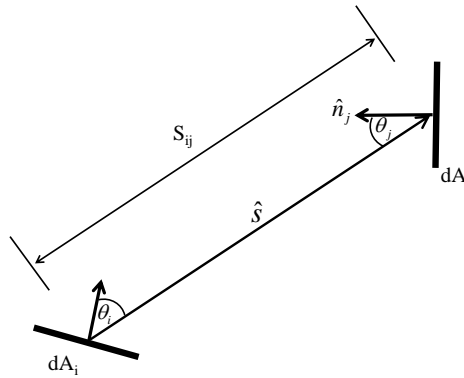


FIGURE 3.1: Radiation exchange between two differential surfaces.

Before deriving the direct-exchange areas for a system with a participating medium, the relations for net radiation between  $N$  isothermal surface zones will first be derived.

Direct exchange areas are related to view factors by the following equation:

$$\overline{s_i s_j} = \overline{s_j s_i} = A_i F_{i \rightarrow j} = A_j F_{j \rightarrow i} \quad (3.1)$$

Direct exchange areas differ from view factors in that it has the dimension of area. This ensures that reciprocity is more easily applied, and it is accepted practice to use direct exchange areas in the Zonal Approach. In the absence of a participating medium, the

direct exchange areas between two grey, diffuse surfaces can be calculated as:

$$\overline{s_i s_j} = \int_{A_i} \int_{A_j} \frac{\cos \theta_i \cos \theta_j}{\pi S_{ij}^2} dA_j dA_i \quad (3.2)$$

The net exchange of radiative energy between two surfaces is then given by:

$$Q_{i \leftrightarrow j} = -Q_{j \leftrightarrow i} = s_i s_j (J_i - J_j) \quad i, j = 1, 2, \dots, N \quad (3.3)$$

The net heat flux at zone  $i$  is obtained by summing eq. [3.3] over all  $N$  surface zones:

$$Q_i = A_i q_i = A_i J_i - \sum_{j=1}^N \overline{s_i s_j} J_j \quad i = 1, 2, \dots, N \quad (3.4)$$

Where  $J_i$  is the radiosity of surface  $i$ . In the previous section it was mentioned that in order to use the Zonal Approach, the enclosure must be fully enclosed. The reason for this is to utilise the sum of all the direct exchange factors from surface zone  $i$  for both an error checking mechanism and an energy balance, by using the following equation:

$$\sum_{j=1}^N \overline{s_i s_j} = \sum_{j=1}^N F_{i \rightarrow j} A_i = A_i \quad (3.5)$$

Since the enclosure is fully closed, we can see from eq. [3.5] that  $\sum_{i=1}^N F_{i \rightarrow j} = 1$ .

## 3.4 Radiative exchange with a participating medium

### 3.4.1 Derivation of surface to volume direct exchange area

In this section the direct-exchange areas between surface and volume zones for an enclosure with a participating medium will be derived. When the void of the enclosure is filled with a participating medium, there is now not only radiative exchange between surface zones only, but also from surface to volume zones and volume to volume zones. The participating medium also causes attenuation of the thermal radiation as the radiation moves through the enclosure. The exchange between a differential surface and volume element is illustrated in figure 3.2.

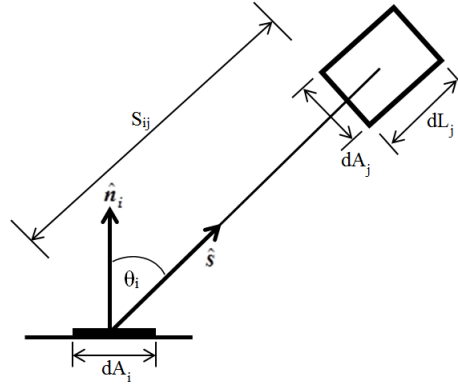


FIGURE 3.2: Radiation exchange from a differential surface to a differential volume element.

The radiation intensity at  $dA_i$  is  $I_i$ . The projected area of  $dA_i$  normal to the direction vector  $\hat{s}$  at any distance away from  $i$  is:

$$dA_{i,projected} = \cos \theta_i dA_i \quad (3.6)$$

Without attenuation the rate at which radiation leaves  $dA_i$  and is intercepted by  $dA_j$  can be expressed as:

$$d\dot{Q}_{i \rightarrow j} = I_i \cos \theta_i dA_i d\Omega_{i \rightarrow j} \quad (3.7)$$

Where  $\Omega_{i \rightarrow j}$  is the solid angle subtended by  $dA_j$  when viewed from  $dA_i$ . Therefore:

$$d\Omega_{i \rightarrow j} = \frac{dA_j}{S_{ij}^2} \quad (3.8)$$

Eq. [3.7] now becomes:

$$d\dot{Q}_{i \rightarrow j} = \frac{I_i \cos \theta_i dA_i dA_j}{S_{ij}^2} \quad (3.9)$$

However, due to attenuation only a portion of the radiation reaches  $dA_j$ :

$$d\dot{Q}_{i \rightarrow j} = I_i e^{-\kappa S_{ij}} \frac{\cos \theta_i dA_i dA_j}{S_{ij}^2} \quad (3.10)$$

Of this only a portion is absorbed in  $dV_j$  namely  $\kappa dL_j$ :

$$\begin{aligned} d\dot{Q}_{i \rightarrow j} &= I_i e^{-\kappa S_{ij}} \frac{\cos \theta_i dA_i \kappa dL_j dA_j}{S_{ij}^2} \\ d\dot{Q}_{i \rightarrow j} &= I_i e^{-\kappa S_{ij}} \frac{\cos \theta_i}{S_{ij}^2} \kappa dA_i dV_j \end{aligned} \quad (3.11)$$

For opaque, grey, diffuse surfaces the total radiant energy leaving the surface per unit area at all possible wavelengths in all possible directions is equal to the radiosity  $J_i$ . The total radiative intensity is defined as the radiative energy flow per unit time per unit area normal to the ray per solid angle at all possible wavelengths.

Therefore:

$$\begin{aligned}
 J_i(\bar{r}) &= \int_{2\pi} I(\bar{r}; \hat{s}) \hat{n} \cdot \hat{s} d\Omega \\
 J_i(\bar{r}) &= \int_{2\pi} I(\bar{r}; \hat{s}) \cos \theta d\Omega \\
 J_i(\bar{r}) &= \int_0^{2\pi} \int_0^{\pi/2} I(\bar{r}, \theta; \Psi) \cos \theta \sin \theta d\theta d\Psi
 \end{aligned} \tag{3.12}$$

For a diffuse surface, the radiation intensity is independent of direction, therefore:

$$\begin{aligned}
 J_i(\bar{r}) &= \bar{I}(\bar{r}) \int_{2\pi} \int_{\pi/2} \cos \theta \sin \theta d\theta d\Psi \\
 J_i(\bar{r}) &= \frac{\bar{I}(\bar{r})}{2} \int_0^{2\pi} [\sin^2 \theta]_0^{\pi/2} d\Psi \\
 J_i(\bar{r}) &= \frac{\bar{I}(\bar{r})}{2} \int_0^{2\pi} d\Psi \\
 J_i(\bar{r}) &= \pi \bar{I}(\bar{r}) \\
 \bar{I}(\bar{r}) &= \frac{J_i(\bar{r})}{\pi}
 \end{aligned} \tag{3.13}$$

The rate at which the radiation leaves  $dA_i$  and reaches  $dA_j$  can now be expressed as:

$$dQ_{i \rightarrow j} = e^{-\kappa S_{ij}} \frac{\cos \theta_i}{\pi S_{ij}^2} \kappa dA_i dV_j \cdot J_i \tag{3.14}$$

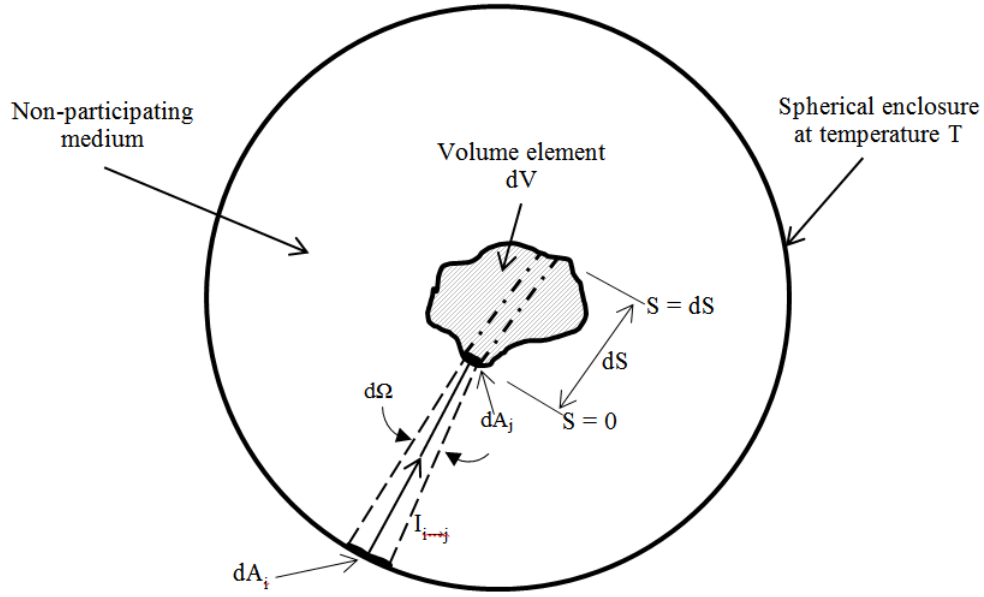


FIGURE 3.3: Radiation exchange between the surface of a hollow sphere and a differential volume element.

Integrating eq. [3.14], we get:

$$\begin{aligned}
 Q_{i \rightarrow j} &= \left[ \int_{V_j} \int_{A_i} e^{-\kappa S_{ij}} \frac{\cos \theta_i}{\pi S_{ij}^2} \kappa dA_i dV_j \right] J_i \\
 Q_{i \rightarrow j} &= \overline{s_i g_j} J_i \\
 \overline{s_i g_j} &= \int_{V_j} \int_{A_i} e^{-\kappa S_{ij}} \frac{\cos \theta_i}{\pi S_{ij}^2} \kappa dA_i dV_j
 \end{aligned} \tag{3.15}$$

Where  $\overline{s_i g_j}$  in eq. [3.15] gives the direct-exchange area for an enclosure with a participating medium.

### 3.4.2 Derivation of the emission of an isothermal volume

Before deriving the volume-to-surface and volume-to-volume direct exchange areas (i.e. the exchange in an enclosure from an isothermal volume zone's point of view) the emission of an isothermal volume must first be derived. Consider a volume element inside a hollow sphere as shown in figure 3.3. The sphere is filled with a non-participating medium and the volume element consists of a participating medium. The shell of the sphere is isothermal.

Let the radiation intensity at  $dA_i$  be  $I_i$ . Then the intensity leaving  $dA_i$  which is intercepted by  $dA_j$  without reflections is given by:

$$I_{i \rightarrow j} = I_i \cos \theta_i dA_i \quad (3.16)$$

The intensity received at  $dA_j$  decreases as it is absorbed through the participating medium over a distance of  $dS$ :

$$dI_{abs} = -I_{i \rightarrow j} \kappa dS \quad (3.17)$$

The use of the absorption coefficient implies that the effect of the induced emission is also included. The energy absorbed by the subvolume  $dA_j dS$  from the incident radiation from  $dA_i$  is:

$$dQ_{abs} = -dI_{i \rightarrow j} dA_j d\Omega \quad (3.18)$$

$$dQ_{abs} = I_{i \rightarrow j} \kappa dS dA_j d\Omega$$

The energy emitted by  $dA_i$  which is absorbed by the entire volume element  $dV$  can be found by integrating over  $dV$ :

$$dQ_{i \rightarrow j} = I_{i \rightarrow j} \kappa d\Omega \int_{dV} dA_j dS \quad (3.19)$$

$$dQ_{i \rightarrow j} = I_{i \rightarrow j} \kappa dV d\Omega$$

Where  $d\Omega$  is the solid angle subtended by  $dA_i$  as viewed from  $dV$ .

The energy transferred from the entire surface of the spherical shell to the volume element  $dV$  will be obtained if we integrate over all solid angles:

$$dQ_{sphere \rightarrow j} = I_{i \rightarrow j} \kappa dV \int_0^{4\pi} d\Omega \quad (3.20)$$

$$dQ_{sphere \rightarrow j} = 4\pi I_{i \rightarrow j} \kappa dV$$

$dV$  must emit the same amount of energy as the sphere shell to maintain equilibrium inside the enclosure:

$$dQ_{j \rightarrow sphere} = 4\pi \kappa I_{i \rightarrow j} dV \quad (3.21)$$

And remembering that  $I = J_i/\pi$  (eq. [3.13]), we get:

$$dQ_{j \rightarrow sphere} = 4\kappa J_i dV \quad (3.22)$$

Eq. [3.22] is valid for a medium with a refraction index of  $n \approx 1$  (i.e. for a gas). If the refractive index of the medium is not equal to unity, the spectral volumetric emission is modified by an  $n^2$  factor, so that the equation becomes:

$$dQ_{j \rightarrow \text{sphere}} = 4\kappa n^2 J_i dV \quad (3.23)$$

### 3.4.3 Derivation of volume to surface direct exchange area

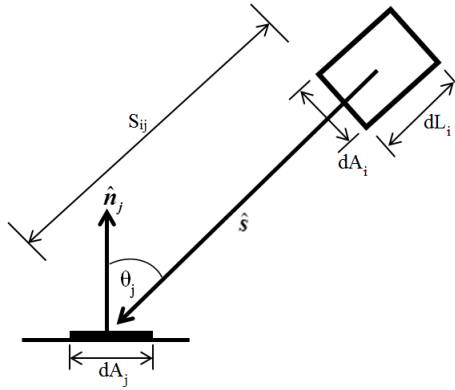


FIGURE 3.4: Radiation exchange from a differential volume to a differential surface element.

The radiation emitted from  $dV_i$  in all  $4\pi$  directions is  $4\kappa n^2 J_i dV$ . Without attenuation the rate at which radiation leaves  $dV_i$  and is intercepted by  $dA_j$  can be expressed as:

$$d\dot{Q}_{i \rightarrow j} = 4\kappa n^2 J_i dV \times d\Omega_{i \rightarrow j} \quad (3.24)$$

The solid angle subtended by area  $dA_j$  is:

$$\begin{aligned} d\Omega_{i \rightarrow j} &= \frac{A_{p,j}}{A_{p,i}} \\ d\Omega_{i \rightarrow j} &= \frac{dA_j \cos \theta_j}{S_{ij}^2 \int_0^{2\pi} \int_0^\pi \sin \theta d\theta d\psi} \\ d\Omega_{i \rightarrow j} &= \frac{dA_j \cos \theta_j}{4\pi S_{ij}^2} \end{aligned} \quad (3.25)$$

The rate at which radiation leaves  $dV_i$  and is intercepted by  $dA_j$  without attenuation then becomes:

$$d\dot{Q}_{i \rightarrow j} = \frac{4\kappa n^2 J_i dV_i}{4\pi} \times \frac{\cos \theta_j dA_j}{S_{ij}^2} \quad (3.26)$$

Due to attenuation, only a portion will reach  $dA_j$ :

$$\begin{aligned} d\dot{Q}_{i \rightarrow j} &= e^{-\kappa S} \frac{4\kappa n^2 J_i dV_i}{4\pi} \times \frac{\cos \theta_j dA_j}{S_{ij}^2} \\ d\dot{Q}_{i \rightarrow j} &= e^{-\kappa S} \kappa n^2 \frac{\cos \theta_j}{\pi S_{ij}^2} dA_j dV_i \times J_i \end{aligned} \quad (3.27)$$

And this is equal to:

$$d\dot{Q}_{i \rightarrow j} = \overline{g_i s_j} J_i \quad (3.28)$$

### 3.4.4 Derivation of volume to volume direct exchange area

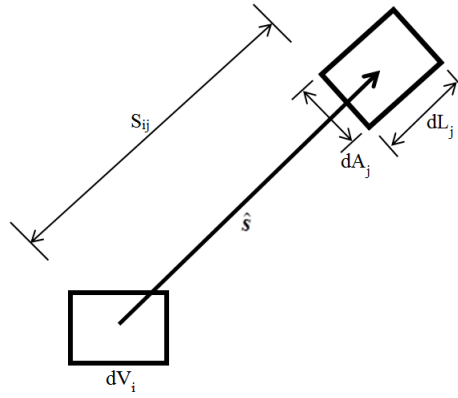


FIGURE 3.5: Radiation exchange between two differential volume elements.

The radiation emitted from  $dV_i$  in all  $4\pi$  directions is  $4\kappa n^2 J_i dV$ . Without attenuation the rate at which radiation leaves  $dV_i$  and is intercepted by  $dA_j$  can be expressed as:

$$d\dot{Q}_{i \rightarrow j} = 4\kappa n^2 J_i dV_i \times d\Omega_{i \rightarrow j} \quad (3.29)$$

The solid angle subtended by area  $dA_j$  is:

$$\begin{aligned} d\Omega_{i \rightarrow j} &= \frac{A_{p,j}}{A_{p,i}} \\ d\Omega_{i \rightarrow j} &= \frac{dA_j}{S_{ij}^2 \int_0^{2\pi} \int_0^\pi \sin \theta d\theta d\psi} \\ d\Omega_{i \rightarrow j} &= \frac{dA_j}{4\pi S_{ij}^2} \end{aligned} \quad (3.30)$$



The rate at which radiation leaves  $dV_i$  and is intercepted by  $dA_j$  without attenuation then becomes:

$$d\dot{Q}_{i \rightarrow j} = 4\kappa n^2 J_i dV_i \times \frac{dA_j}{4\pi S_{ij}^2} \quad (3.31)$$

Due to attenuation only a portion will reach  $dA_j$ :

$$d\dot{Q}_{i \rightarrow j} = e^{-\kappa S} \times 4\kappa n^2 J_i dV_i \times \frac{dA_j}{4\pi S_{ij}^2} \quad (3.32)$$

Volume  $dV_j = dA_j \times dL_j$  also absorbs some of the radiation over  $dL_j$ :

$$\begin{aligned} d\dot{Q}_{i \rightarrow j} &= e^{-\kappa S} \times 4\kappa n^2 J_i dV_i \times \frac{dA_j}{4\pi S_{ij}^2} \times \kappa dL_j \\ d\dot{Q}_{i \rightarrow j} &= e^{-\kappa S} \frac{\kappa^2 n^2}{\pi S_{ij}^2} dV_j dV_i \times J_i \end{aligned} \quad (3.33)$$

And this is equal to:

$$d\dot{Q}_{i \rightarrow j} = \overline{g_i g_j} J_i \quad (3.34)$$

### 3.5 Energy balances for the Zonal Approach

According to Modest (2003) the energy balance for a surface zone  $Q_{si}$  in a system with an enclosure containing a grey absorbing/emitting medium with  $N$  surface zones and  $K$  volume zones can be written as:

$$Q_{si} = \varepsilon_i \left( A_i E_{bsi} - \sum_{j=1}^N \overline{s_j s_i} J_j - \sum_{k=1}^K \overline{g_k s_i} E_{bgk} \right), \quad i = 1, 2, \dots, N. \quad (3.35)$$

For an isothermal enclosure the following relationship is obtained:

$$\sum_{j=1}^N \overline{s_j s_i} + \sum_{k=1}^K \overline{g_k s_i} = A_i \quad i = 1, 2, \dots, N. \quad (3.36)$$

Eq. [3.35] shows that the net energy of a surface zone is equal to the total radiated energy of that surface zone minus the fraction absorbed by the other surface and volume zones in the system. Similarly, an energy balance can be written on a volume zone as:

$$Q_{gi} = 4\kappa V_i E_{bgi} - \sum_{j=1}^N \overline{s_j g_i} J_j - \sum_{k=1}^K \overline{g_k g_i} E_{bgk}, \quad i = 1, 2, \dots, K. \quad (3.37)$$

And again by looking at an isothermal enclosure:

$$\sum_{j=1}^N \overline{s_j g_i} + \sum_{k=1}^K \overline{g_k g_i} = 4\kappa V_i \quad i = 1, 2, \dots, K. \quad (3.38)$$

The energy balances over the surface and volume zones gives a system of  $N + K$  equations, with  $J_{si}$  and  $Q_{si}$  ( $i = 1, 2, \dots, N$ ) unknowns as well as  $Q_{gi}$  ( $i = 1, 2, \dots, K$ ) or  $E_{gi}$  ( $i = 1, 2, \dots, K$ ) unknowns. According to Modest (2003) the  $Q_{si}$  for the surface zones can be eliminated using eqns. (3.39) and (3.40):

$$Q_{si} = A_i q_{si} \quad i = 1, 2, \dots, N. \quad (3.39)$$

$$q_{si} = \frac{\varepsilon_i}{1 - \varepsilon_i} (E_{bsi} - J_{si}) \quad (3.40)$$

If  $Q_{si}$  is eliminated with the above equations, it then reduces to a system of  $N + K$  equations and  $N + K$  unknowns. A system of the form  $\mathbf{Ax} = \mathbf{b}$  with  $(N + K)$  equations can then be setup, and solved for  $\mathbf{x}$  through matrix inversion, where  $\mathbf{x}$  represents the unknown heat  $Q_{si}$  or radiosities  $J_{si}$  for the surface zones and the unknown heat  $Q_{gi}$  of blackbody radiation  $E_{bgi}$  for the volume zones.

## 3.6 Adapting the Zonal Approach for Surface Exchange

### 3.6.1 Background

Up to this point it was assumed that the participating medium used in the derivations of the direct exchange areas was a transparent or semi-transparent medium, as used in the classic Zonal Approach. From this point on the Zonal Approach will be adapted for use with a packed pebble bed containing mono-sized spheres. As mentioned in the previous section, the extinction coefficient  $\beta$  is the sum of the attenuation factor  $\kappa$  and the scattering coefficient  $\sigma_s$  for a bed filled with a gray absorbing and emitting medium like pulverised coal. An enclosure that is filled with an absorbing and emitting gas or a semi-transparent solid or liquid is referred to as radiative transport in a participating medium which is also accompanied by surface radiation transport. The radiative properties necessary for evaluating thermal radiation for a semi-transparent medium is absorptance, reflectance, emission, attenuation and scattering. For surfaces it is only absorptance, reflectance and emission. According to Modest (2003) the interaction between electromagnetic radiation and the particles contained in the volume zones are dictated by the relative size between the particles and the wavelength of the radiation. The size parameter can be given as:

$$x = \frac{\pi D}{\lambda} \quad (3.41)$$

From this size parameter three different regimes can be identified:

1. If  $x \ll 1$  then Rayleigh scattering is used.
2. If  $x \approx O(1)$  then Mie scattering is used.
3. If  $x \gg 1$  then the surface can be treated as a normal surface and geometric optics can be used to obtain the properties.

It is clear that in the current case, with a pebble diameter of  $D_p = 0.06\text{m}$  the size order between a pebble and the (mostly) infrared wavelengths will yield a value for  $x$  much larger than 1, implying that the exchange to and from the volume zones containing the pebbles can be treated as surface exchange. Keeping this in mind, the emissive power of a surface can be written as:

$$\begin{aligned} I_s &= \varepsilon A_s E_{bs} \\ I_s &= \varepsilon A_s \sigma T_s^4 \end{aligned} \quad (3.42)$$

### 3.6.2 Exchange for a volume zone containing one centralised sphere

For a simple case where a rectangular bed with a structured packing of equally spaced mono-sized spheres we can subdivide the volume into equal cubic volume zones containing one centralised sphere, as shown in figure 3.6. The cubic volume zone will have dimensions of  $D_p^3$  and the sphere inside the volume zone will have a diameter of  $D_p$  and is shown in figure 3.7. Since the emission will be from the sphere inside the cubic volume (and not from the entire cubic volume like the classic Zonal Approach), the emitting area in eq. [3.42] can be substituted as:

$$I_b = \varepsilon \cdot \pi D_p^2 \cdot \sigma T_s^4 \quad (3.43)$$

#### 3.6.2.1 Surface to surface direct exchange areas

The surface to surface direct exchange areas (DEA) will remain the same (as is shown in figure 3.1) as for the general Zonal Approach since the enclosure surfaces remain the same, with an attenuation factor representing the loss in emitting intensity due to absorption as the thermal radiation travels through the bed. The surface to surface exchange can be written as the heat flux leaving zone  $I$  arriving at zone  $j$  which equals the intensity

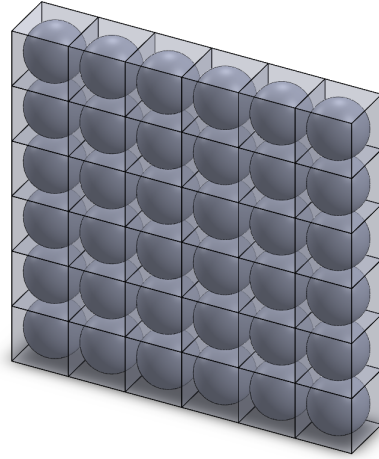


FIGURE 3.6: A representation of a cubic structured bed subdivided by equally sized volume and surface zones.

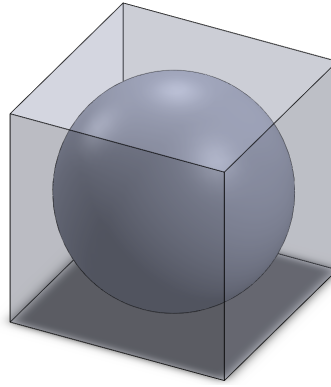


FIGURE 3.7: A representation of a volume zone for a cubic structured bed containing one centralised sphere.

leaving  $dA_i$  into the direction of  $dA_j$  times the area normal to the ray times the solid angle subtended by  $dA_j$  as seen from  $dA_i$  times the fraction transmitted, or:

$$Q_{i \rightarrow j} = \frac{J_i}{\pi} \times dA_i \cos \theta_i \times \frac{dA_j}{S^2} \quad (3.44)$$

The surface to surface DEA can be derived from eq. [3.44] to be:

$$\overline{s_i s_j} = \int_{A_i} \int_{A_j} e^{-\kappa S} \frac{\cos \theta_i \cos \theta_j}{\pi S^2} dA_j dA_i \quad (3.45)$$

With:  $J_i$  the radiosity, remembering that the radiosity of an emitting surface is  $J_i = \pi I$ , where  $I$  is the emitting intensity,  $dA$  is the differential surface area,  $\Theta$  is the angle between the line connecting the two zones' centroids and the surface normal,  $S$  is the distance between the two surfaces and  $\kappa$  is the attenuation factor.

### 3.6.2.2 Volume to surface direct exchange areas

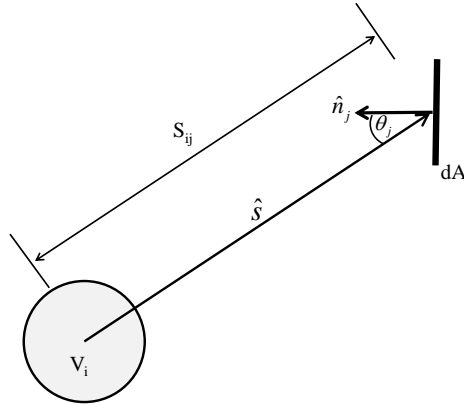


FIGURE 3.8: Radiation exchange between a sphere and a surface element.

From Modest (2003) we know that the volume to surface direct exchange areas (DEA) for the Zonal Approach containing grey gases can be calculated by:

$$\overline{g_i s_j} = \int_{V_i} \int_{A_j} e^{-\kappa S} \frac{\cos \theta_j}{\pi S^2} \kappa dA_j dV_i \quad (3.46)$$

Eq. [3.46] is derived from the heat flux emanating from a volume zone  $i$  which is intercepted by a surface zone  $j$ , and is illustrated in figure 3.8. This can be written as the energy emitted from  $dV_i$  in all  $4\pi$  directions times fraction leaving towards the surface zone element  $dA_j$  times fraction transmitted, or:

$$Q_{i \rightarrow j} = (4\kappa E_{bi} dV_i) \times \left( \frac{dA_j \cos \theta_j}{4\pi S^2} \right) \times (e^{-\kappa S}) \quad (3.47)$$

If we apply the logic of eq. [3.47], but remembering we have to derive the direct exchange area for a sphere-centred control volume, as shown in figure 3.8, and that eq. [3.43] represents the emissive power of a volume zone in a structured bed, we get:

$$Q_{i \rightarrow j} = (A_{sphere} E_{bi}) \times \left( \frac{dA_j \cos \theta_j}{4\pi S^2} \right) \times (e^{-\kappa S}) \quad (3.48)$$

And the DEA for a sphere-centred control volume will then be:

$$\overline{g_i s_j}^{SC} = e^{-\kappa S} \frac{\cos \theta_j}{4\pi S^2} (dA_j) (A_{sphere}) \quad (3.49)$$

To double-check the derivation resulting in eq. [3.49], we can approach the derivation from the point-of-view that it is a surface-to-surface exchange (which it is, strictly speaking). If we first remember, from the derivation of the radiation intensity for all surfaces, from Modest (2003) we have:

$$I_r = J_i/\pi \quad (3.50)$$

So the heat flux leaving zone  $i$  arriving at zone  $j$  will be equal to the intensity leaving  $dA_i$  towards  $dA_j$  x area normal to the ray x solid angle subtended by  $dA_j$  as seen from  $dA_i$  x fraction transmitted, or:

$$Q_{i \rightarrow j} = \left( \frac{J}{\pi} \right) \times (A_{circle}) \times \left( \frac{dA_j \cos \theta_j}{S^2} \right) \times e^{-\kappa s} \quad (3.51)$$

The area  $A_{circle}$  is the cross-sectional area of the sphere, which will be the effective area that is normal to the ray, and which will also be the effective area that is visible from  $dA_j$ . Since  $A_{circle} = \pi r^2 = \pi D^2/4$ , implying that  $A_{circle} = A_{sphere}/4$  we can rewrite eq. [3.51] as:

$$Q_{i \rightarrow j} = \left( \frac{J}{\pi} \right) \times \left( \frac{A_{sphere}}{4} \right) \times \left( \frac{dA_j \cos \theta_j}{S^2} \right) \times e^{-\kappa s} \quad (3.52)$$

Or if we derive it the other way around with the enclosure surface as  $A_i$  and the sphere as  $j$ , we get for the heat flux:

$$\begin{aligned} Q_{i \rightarrow j} &= \left( \frac{J}{\pi} \right) \times (dA_j \cos \theta_j) \times \left( \frac{A_{circle}}{S^2} \right) \times e^{-\kappa s} \\ \therefore Q_{i \rightarrow j} &= \left( \frac{J}{\pi} \right) \times (dA_j \cos \theta_j) \times \left( \frac{A_{sphere}}{4S^2} \right) \times e^{-\kappa s} \end{aligned} \quad (3.53)$$

All three the derivations for the exchange between a sphere-centered volume zone and an enclosure's surface zone results in the same expression:

$$\overline{g_i s_j}^{SC} = e^{-\kappa s} \frac{\cos \theta_j}{4\pi S^2} dA_j A_{sphere} \quad (3.54)$$

### 3.6.2.3 Volume to volume direct exchange areas

The volume to volume direct exchange area for the Zonal Approach is given by:

$$\overline{g_i g_j} = \int_{V_i} \int_{V_j} e^{-\kappa S} \frac{\kappa^2}{\pi S^2} dV_j dV_i \quad (3.55)$$

Eq. [3.55] is derived from the heat flux emanating from a volume zone  $i$  which is intercepted by a volume zone  $j$ , and is illustrated in figure 3.5. This can be written as the energy emitted from  $dV_i$  in all  $4\pi$  directions times the fraction leaving towards the front surface of volume zone  $j$ , which is denoted by  $dA_j$  times the fraction transmitted times the fraction

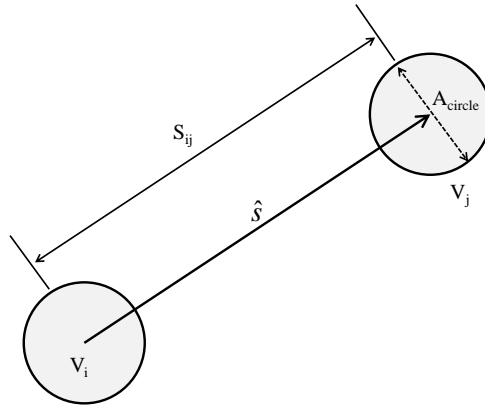


FIGURE 3.9: Radiation exchange between two spheres.

absorbed over the thickness of the volume zone  $j$ , or:

$$Q_{i \rightarrow j} = (4\kappa E_{bi} dV_i) \times \left( \frac{dA_j}{4\pi S^2} \right) \times (e^{-\kappa S}) \times (\kappa dS_j) \quad (3.56)$$

If one looks at figure 3.5 one can see that for the derivation the volume zone  $j$  was rotated so that its front surface  $dA_j$  is normal to the incident radiation which will eliminate any  $\cos \theta_j$  term because the surface normal  $\hat{n}_j$  is co-linear with the incident radiation making  $\cos \theta_j = \cos(0^\circ) = 1$ . For the sphere-centred control volume this will naturally also occur since a sphere's projected area ( $A_{circle} = \pi r^2$ ) will never change no matter the rotation, i.e. it will always be co-linear with the surface normal. The final part of eq. [3.56] denotes absorption of the incident radiation from control volume  $i$  which will not happen in the current case of a sphere-centred or random-packed control volume, since we are not dealing with control volumes filled with grey gases with a refractive index of  $n \approx 1$ , with transmissivities  $\tau_r \ll 1$  and which are capable of absorbing incident radiation through attenuation ( $\kappa$ ). The current study's sphere-centred and random control volumes only contain surfaces from spheres which can absorb and reflect incident rays from its surfaces.

If the same logic for a volume-volume control volume is applied to the sphere-centred volume zones of the structured bed as was used in eq. [3.56] and as shown in figure 3.9, we get for the heat emanating from a volume zone  $i$  which is intercepted by a volume zone  $j$  will be equal to the energy emitted from zone  $i$  in all  $4\pi$  directions times the fraction leaving towards zone  $j$  (which is written as the fraction of the projected surface of zone  $j$  divided by the total surface area of the emitted radiation from zone  $i$  at the position of

zone  $j$ ) times the fraction transmitted, or:

$$\begin{aligned} Q_{i \rightarrow j} &= (A_{sphere} J_i) \times \left( \frac{A_{circle}}{4\pi S^2} \right) \times (e^{-\kappa s}) \\ \therefore Q_{i \rightarrow j} &= (A_{sphere} J_i) \times \left( \frac{A_{sphere}}{16\pi S^2} \right) \times (e^{-\kappa s}) \end{aligned} \quad (3.57)$$

Eq. [3.57] was derived as heat and not as heat flux leaving zone  $i$  as for the enclosure surfaces. If we want to double-check the derivation of eq. [3.57], we can re-derive it in terms of heat fluxes instead of heat as with the enclosure's surface zones. To get the heat flux leaving zone  $i$  which is intercepted by zone  $j$  equals the intensity leaving zone  $I$  in the direction of zone  $j$  times the area of zone  $i$  normal to the ray times the solid angle of zone  $j$  times the fraction transmitted, or:

$$\begin{aligned} q_{i \rightarrow j} &= \left( \frac{J_i}{\pi} \right) \times (A_{circle}) \times \left( \frac{A_{circle}}{S^2} \right) \times (e^{-\kappa s}) \\ \therefore q_{i \rightarrow j} &= \left( \frac{J_i}{\pi} \right) \times \left( \frac{A_{sphere}}{4} \right) \times \left( \frac{A_{sphere}}{4S^2} \right) \times (e^{-\kappa s}) \end{aligned} \quad (3.58)$$

Where eq. [3.58] is the same as eq. [3.57], resulting in a direct-exchange area for volume-volume exchange of:

$$\overline{g_i g_j} = e^{-\kappa S} \frac{1}{4\pi S^2} A_j A_i \quad (3.59)$$

### 3.6.3 Evaluating the Direct-Exchange Areas

The direct exchange areas as given in section 3.6.2 eqns. [3.45], [3.46] and [3.55] requires numerical integration as it contains differential surface elements. Since the aim of the Zonal Approach is simplicity and faster computational times, the emission from the volume zones were derived from the emission of a full sphere and not surface patches on the sphere. The size of the surface and volume zones were selected as the size of a sphere, i.e.  $1 \times D_p^2$  for the surface zones and  $1 \times D_p^3$  for the volume zones. The surface to surface, surface to volume and volume to volume exchange were evaluated against analytical solutions to ascertain its accuracy for the current application.

#### 3.6.3.1 Surface-to-Surface Exchange Evaluation

The surface-to-surface exchange between two parallel surface zones without a participating medium as given in eq. [3.45] were evaluated against a correlation from Hamilton and Morgan (1952), given in eq. [3.60] and illustrated in figure 3.10. The correlation states that if the approximation method is used the accuracy can be improved by subdividing the



surface zone into any number of finite subdivisions. For the current application the surface and volume zones will not be subdivided but evaluated using its current sizes which can cause large numerical integration errors if the zone's size is large compared to the enclosure. The two opposing surfaces were each  $1 \times D_p^2$  (or  $(0.06)^2\text{m}$ ) in size. The DEA versus distance is shown in figure 3.11, and it is three times larger than the analytical correlation at close distance ( $0.5D_p = 0.03\text{m}$ ) and converges at larger distances ( $> 1 \times D_p = 0.06\text{m}$ ). Since the parallel opposing surface areas will be generally at least  $1D_p = 0.06\text{m}$  from each other this correlation is usable in its current form.

$$F_{1-2} = \frac{2}{\pi XY} \left\{ \ln \left[ \frac{(1+X^2)(1+Y^2)}{1+X^2+Y^2} \right]^{1/2} + X\sqrt{1+Y^2} \tan^{-1} \frac{X}{\sqrt{1+Y^2}} \right. \\ \left. + Y\sqrt{1+X^2} \tan^{-1} \frac{Y}{\sqrt{1+X^2}} - X \tan^{-1} X - Y \tan^{-1} Y \right\} \quad (3.60)$$

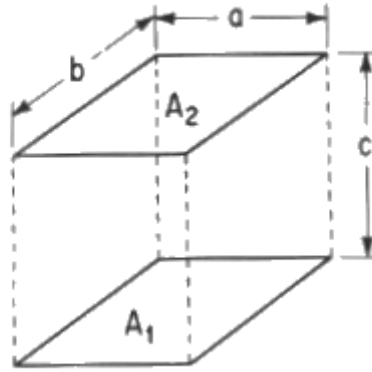


FIGURE 3.10: Figure to be used together with eq. [3.60] to calculate the exchange between two identical parallel plates, from Howell and Mengüç (2011).

### 3.6.3.2 Volume-to-Surface Exchange Evaluation

When comparing eq. [3.49] with an analytical solution obtained from Feingold and Gupta (1970) and illustrated in eq. [3.61] and figure 3.13. For a sphere to a rectangular surface perpendicular to the line through the sphere centre, the derivation over-predicts the DEA roughly by a factor of two. A possible explanation is that the derivation assumes that the emission sphere evaluated at the receiving zone's position (given by  $4\pi S^2$ ) doesn't enclose the surface zone, the surface zone is just tangent to it (as illustrated in figure 3.12). The correlation requires that the emission absorbed by the surface zone is equal to the surface area of the surface zone divided by the imaginary surface area of the spherical emission at the surface zone's position and with this implies that the surface zone's surface area

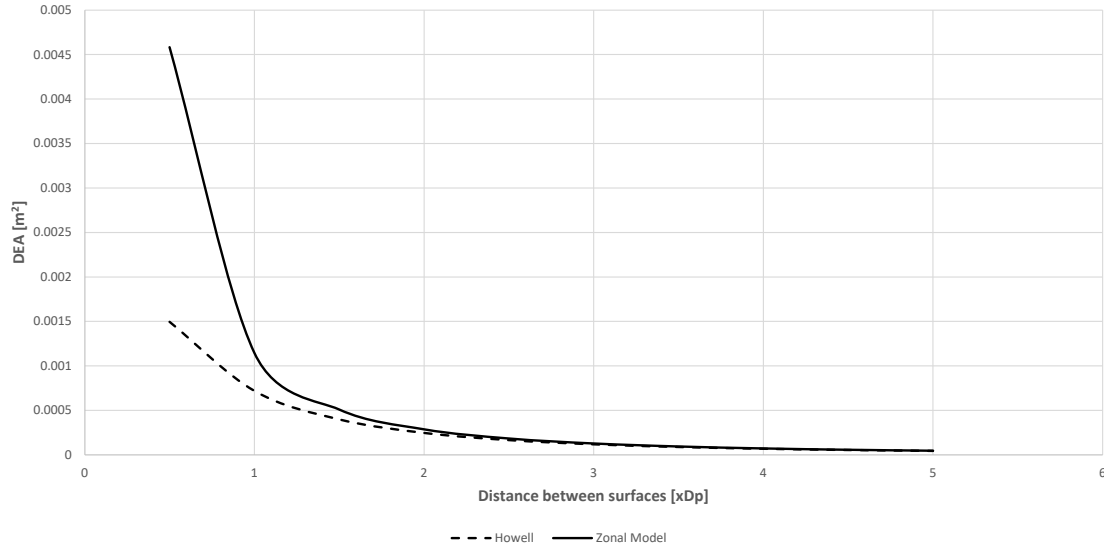


FIGURE 3.11: Surface-to-surface exchange plot of derived Zonal correlation and analytical correlation from Hamilton and Morgan, 1952.

is at least approximately covered by the emission sphere. This effect will especially be true for short distances  $S$  between the sphere and surface zone, but as the distance (and subsequently the effective emission from the sphere, given by  $4\pi S^2$ ) increases to  $1.5 \times D_p$  between the centre of the zones, the effect decreases until it is negligible. Unfortunately the bulk of the heat exchange occurs at short distances of  $S$ , necessitating the specification of more accurate values for spheres and surfaces adjacent to each other. These values can either be from analytical solutions or from ray tracing, which will be more accurate for specific cases with a participating medium present.

$$F_{1-2} = \frac{1}{2\pi} \left\{ \sin^{-1} \left[ \frac{2B_1^2 - (1-B_1^2)(B_1^2+B_2^2)}{(1+B_1^2)(B_1^2+B_2^2)} \right] + \sin^{-1} \left[ \frac{2B_2^2 - (1-B_2^2)(B_1^2+B_2^2)}{(1+B_2^2)(B_1^2+B_2^2)} \right] \right\} \quad (3.61)$$

$$\text{with : } B_1 = b_1/a$$

$$B_2 = b_2/a$$

### 3.6.3.3 Volume-to-Volume Exchange Evaluation

The volume-to-volume zone exchange is equal to the total energy emitted by a sphere in all  $4\pi$  directions times the amount intercepted by the other sphere times the amount transmitted, or:

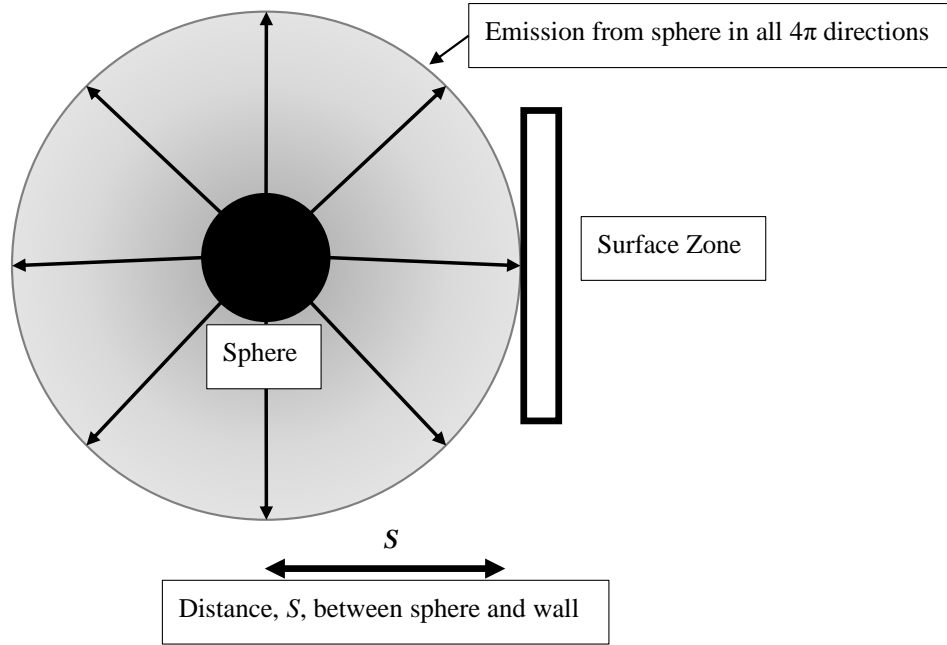


FIGURE 3.12: Volume-to-surface emission for a sphere to a flat surface.

$$Q_{i \rightarrow j} = A_i E_{bi} \times \frac{A_j}{4\pi S^2} \times e^{-\kappa S}$$

$$\therefore \overline{g_i g_{ij}} = e^{-\kappa S} \frac{1}{4\pi S^2} A_j A_i \quad (3.62)$$

With:  $A_i = \pi D_p^2$  (sphere surface area)

and  $A_j = (\pi/4) D_p^2$  (Projected sphere area = cross-sectional area of sphere).

It must be noted that there was a technical note produced by the National Aeronautics and Space Administration (Campbell and McConnell, 1968) where the configuration factors and DEA's for sphere-to-sphere and cones-to-spheres were derived, given in eq. [3.63]. Their conclusion was that the base equation to be used for the sphere-to-sphere exchange was the same as for the exchange between two infinitesimal surfaces, or:

$$A_i F_{ij} = \int_{A_j} \int_{A_i} \frac{\cos \theta_i \cos \theta_j}{\pi S^2} dA_j dA_i \quad (3.63)$$

With eq. [3.63] applying integration for each surface patch on the sphere with regards to its orientation to the second sphere. The integration takes place in all  $4\pi$  directions in spherical coordinates. This approach, although very accurate and not unlike the ray tracing approaches employed by surface-to-surface solvers in modern CFD codes, is not suitable for application inside a packed bed where simplicity and speed is important since

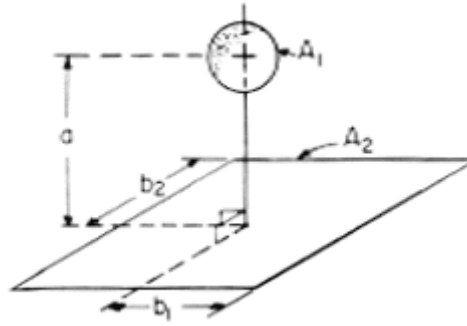


FIGURE 3.13: Figure to be used together with eq. [3.61] to calculate the exchange between a sphere and a perpendicular plate, from Howell and Mengüç (2011).

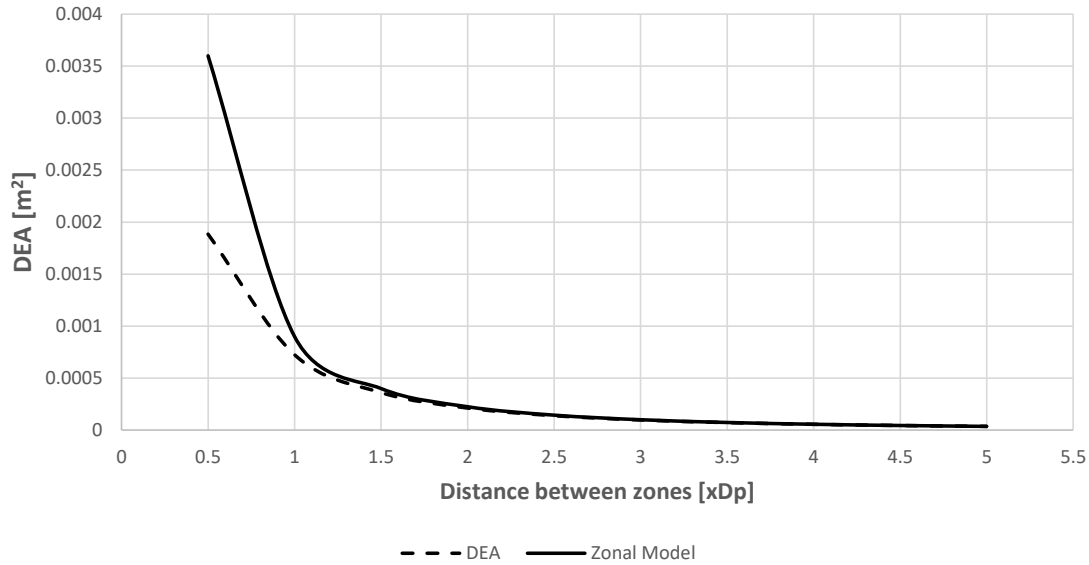


FIGURE 3.14: Volume-to-surface exchange plot of derived Zonal correlation and analytical correlation from Feingold and Gupta (1970).

the calculation between each patch on each sphere inside the bed will be cumbersome and time consuming.

In order to evaluate the accuracy of the assumptions for the volume-to-volume DEA's, it can be compared to a semi-analytical solution from Juul (1976). The correlation is given in eq. [3.64] and based on the geometry shown in figure 3.15. The comparison between the derived volume-to-volume DEA and the correlation by Juul (1976) is shown in figure 3.16. There is a very good agreement between the derived exchange for the Zonal Approach given in eq. [3.62] and the correlation by Juul (1976).

$$F_{1-2} = \frac{1}{2} \left\{ 1 - \left[ 1 - \frac{1}{(S + R + 1)^2} \right]^{1/2} \right\} \quad (3.64)$$

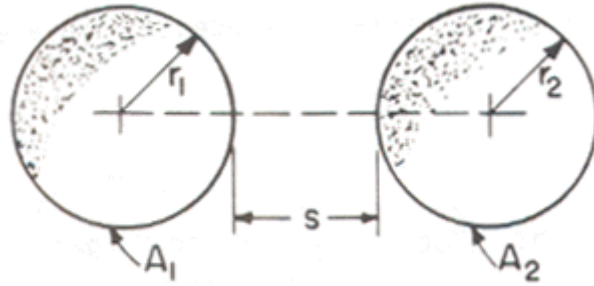


FIGURE 3.15: Figure to be used together with eq. [3.64] to calculate the exchange between two spheres, from Howell and Mengüç (2011).

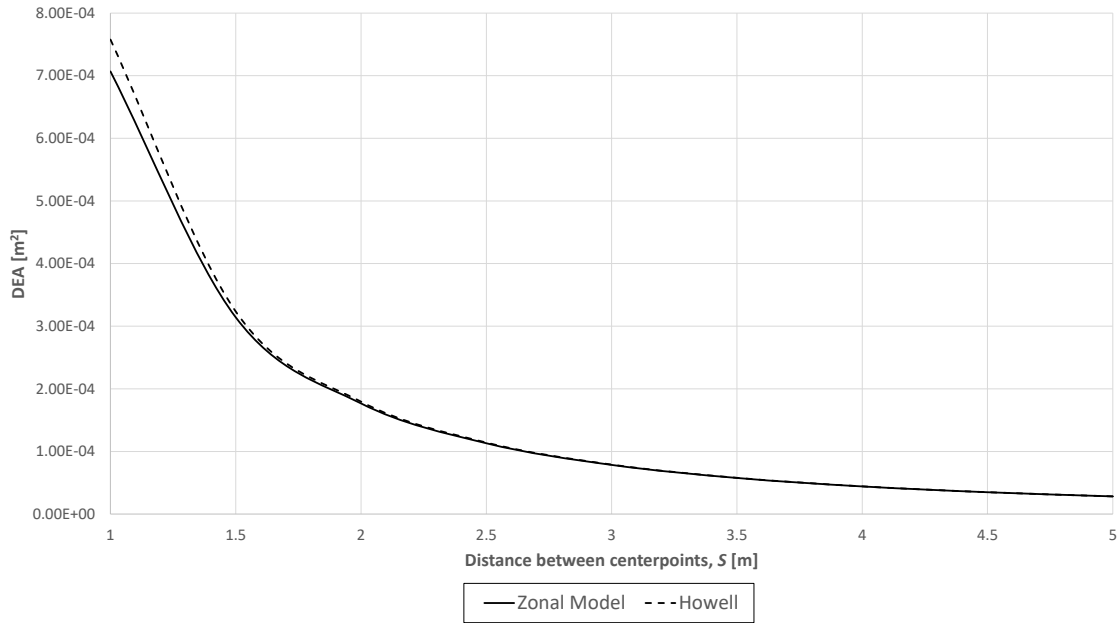


FIGURE 3.16: Volume-to-volume exchange comparing the derived correlation from eq. [3.62] to the semi-analytical solution presented by Juul (1976)

### 3.6.4 Exchange of a volume zone containing random-packed spheres

#### 3.6.4.1 Surface area inside a random-packed volume zone

The previous sections discussed the derivation of the different DEA's for enclosures filled with a structured packing consisting of control volumes with a centralised sphere. In this section it will be expanded to random-packed beds. A volume zone from a random-packed bed with the same cubic dimensions as for the structured volume zone (i.e.  $1 \times D_p^3$ ) usually contains bits and pieces of spheres due to its random nature, as illustrated in figure 3.17.



FIGURE 3.17: A representation of a volume zone one sphere diameter per side for a random bed from the bulk region.

In order to ascertain the total amount of emitted radiation, the total surface area inside a single random-packed control volume must first be determined.

For a random bed, the total volume of a control volume can be given as:

$$V_{CV} = D_p^3 \quad (3.65)$$

The actual volume that the spheres in a random bed will occupy in this control volume is dependent on the porosity  $\alpha$  of the bed in that specific region, and can be given by:

$$V_{S,CV} = (1 - \alpha)V_{CV} \quad (3.66)$$

In order to obtain the effective surface area able to emit from this control volume, we first need to obtain the number of spheres inside this control volume:

$$n_{balls} = \frac{V_{S,CV}}{V_{Sphere}} \quad (3.67)$$

$$n_{balls} = \frac{(1 - \alpha)V_{CV}}{\pi/6 D_p^3} \quad (3.68)$$

Now the total effective surface area able to emit from this control volume can be calculated:

$$A_{Random} = A_{Sphere} \times n_{balls} \quad (3.69)$$

$$A_{Random} = \pi D_p^2 \times \frac{(1 - \alpha)V_{CV}}{\pi/6 D_p^3} \quad (3.70)$$

$$A_{Random} = \frac{6(1 - \alpha)}{D_p} V_{CV} \quad (3.71)$$

Eq. [3.71] represents the total surface area inside a random-packed control volume as a function of porosity.

### 3.6.4.2 Internal radiation inside a random-packed volume zone

A control volume in a random-packed bed not only emits outward to the rest of the bed, but the spheres inside the control volume also absorb some of the emitted radiation (i.e. internal radiation). This can clearly be seen by looking at a typical random-packed volume zone as shown in figure 3.17. Since this internal radiation is unknown, we will derive the internal radiation relative to the radiation of a known control volume: the single sphere-centred control volume as discussed in section 3.6.2 and shown in figure 3.7. We know the net heat from a control volume  $i$  to another control volume  $j$  can be given as:

$$Q_{ij} = A_i F_{ij} (J_i - J_j) \quad (3.72)$$

Where  $A_i F_{ij}$  is the direct exchange area and  $J$  is the radiosity. If we compare a sphere-centred control volume to a random-packed control volume with the same net heat and radiosities, it implies that the direct exchange areas of both are also the same. This leads to:

$$A_{Sphere} F_{ij}^{SC} = A_{Random} F_{ij}^R \quad (3.73)$$

With  $SC$  denoting the sphere-centred control volume and  $R$  denoting the random-packed control volume. When we begin to develop this equation, we get:

$$\pi D_p^2 F_{ij}^{SC} = \frac{6(1-\alpha)}{D_p} \cdot V_{CV} \cdot F_{ij}^R \quad (3.74)$$

$$F_{ij}^R = \frac{\pi D_p^2}{6(1-\alpha) D_p^2} F_{ij}^{SC} \quad (3.75)$$

$$F_{ij}^R = \frac{\pi}{6(1-\alpha)} F_{ij}^{SC} \quad (3.76)$$

The end result for eq. [3.76] denotes the view factor of the random-packed control volume in terms of the sphere-centred control volume. For example, for the bulk region of the random bed the porosity,  $\alpha$ , is 0.39. When substituting this in eq. [3.76] we get for the bulk region:

$$F_{ij}^R = \frac{\pi}{6(1-0.39)} F_{ij}^{SC} \quad (3.77)$$

$$F_{ij}^R = 0.8584 F_{ij}^{SC} \quad (3.78)$$

This implies that only the equivalent of 85.84% of a single sphere's view factor escapes outside this random-packed control volume, even though the direct exchange areas for both

the sphere-centred control volume and the random-packed control volume are equal. Its implications will be seen in the derivation of the energy balance in a later section.

### 3.6.4.3 Direct exchange areas for a volume zone from a random-packed bed

The direct exchange areas for a volume zone from a random-packed bed will be written in terms of the DEA of a volume zone with one centralised sphere. Since the direct exchange areas can be obtained from view factors by multiplying it with the relevant surface area, we can use eq. [3.76] and add the relevant surface areas to the equation to obtain:

$$A_{Random} F_{ij}^R = A_{Random} \frac{\pi}{6(1-\alpha)} F_{ij}^{SC} \quad (3.79)$$

$$A_{Random} F_{ij}^R = A_{Random} \frac{\pi}{6(1-\alpha)} \left( \frac{\overline{g_i s_i}^{SC}}{A_{Sphere}} \right) \quad (3.80)$$

$$\overline{g_i s_i}^R = A_{Random} \frac{\pi}{6(1-\alpha)} \left( \frac{\overline{g_i s_i}^{SC}}{A_{Sphere}} \right) \quad (3.81)$$

And similarly for the volume-to-volume DEA it is:

$$\overline{g_i g_i}^R = A_{Random} \frac{\pi}{6(1-\alpha)} \left( \frac{\overline{g_i g_i}^{SC}}{A_{Sphere}} \right) \quad (3.82)$$

The internal radiation can now be calculated from the direct exchange areas between the viewed zone and the other external surface and volume zones. For a system with  $N$  surface zones and  $K$  volume zones, the internal radiation for volume zone  $i$  is:

$$\overline{g_i g_i}^R = A_{Random} - \left( \sum_{j=1}^N \overline{g_i s_j}^R + \sum_{k=1}^K \overline{g_i g_k}^R \right) \quad (3.83)$$

## 3.7 Smoothing of the direct exchange areas

Due to the accumulated error in estimating the direct exchange areas via the above-mentioned methods, it is essential to ensure an energy balance according to section 3.8. An efficient method is to use a Least-Squares Smoothing algorithm employing Lagrange multipliers as developed by Larsen and Howell (1986). The full technique will not be shown here but it is discussed in detail in Larsen and Howell (1986). The Least-Squares Smoothing Technique using Lagrange multipliers assembles all the direct exchange areas in one matrix to



form a symmetric  $(N + K) \times (N + K)$  matrix (for  $N$  area zones and  $K$  volume zones):

$$X = \begin{bmatrix} \overline{ss} & \overline{sg} \\ \overline{sg}^T & \overline{gg} \end{bmatrix} \quad (3.84)$$

Reciprocity dictates that the  $i^{th}$  row or column must sum to  $c_i$ , where:

$$\sum_{j=1}^{N+K} x_{ij} = c_i \quad (3.85)$$

With:

$$\begin{aligned} c_i &= A_i & i &\leq N \\ c_i &= A_{Sphere} & i > N \text{ (For volume zone with a single central sphere)} \\ c_i &= A_{Random} & i > N \text{ (For volume zone from random bed)} \end{aligned}$$

Since this is rarely the case for the initial assumptions of the direct exchange areas due to numerical integration errors, an adjusted value for  $x_{ij}$  is needed, which is given by:

$$x_{ij}^* = x_{ij} + w_{ij}(\lambda_i + \lambda_j) \quad (3.86)$$

Where  $w_{ij}$  is a weight which allows certain penalties to be arbitrarily assigned to adjust certain factors, and  $\lambda$  is the Lagrangian multiplier. The Lagrangian multiplier can be obtained from solving the following equation:

$$R \bar{\lambda} = \bar{\delta} \quad (3.87)$$

Where:

$$\begin{aligned} r_{ij} &= w_{ij}, \quad i \neq j \\ r_{ii} &= w_{ii} + \sum_{j=1}^{N+K} w_{ij} \\ \delta_i &= c_i - \sum_{j=1}^{N+K} x_{ij} \end{aligned}$$

The error is given by:

$$\sum_{i=1}^M (\lambda_i^{p+1} - \lambda_i^p)^2 < 10^{-10} \quad (3.88)$$

An over-relaxation factor can be added to accelerate the solution of eq. [3.87], and it is recommended to ensure that the error is minimised to at least below  $10^{-10}$ .

### 3.8 Energy balance for an enclosure filled with mono-sized spheres

The energy balance for the enclosure walls will remain the same as for the classic Zonal Approach, i.e.:

$$\sum_{j=1}^N \overline{s_i s_j} + \sum_{k=1}^K \overline{s_i g_k} = A_i, \quad \forall i = 1, 2, \dots, N. \quad (3.89)$$

The energy balance for the volume zones of the structured bed with a control volume containing one centralised sphere will now become:

$$\sum_{j=1}^N \overline{g_i s_j} + \sum_{k=1}^K \overline{g_i g_k} = A_{sphere}, \quad \forall i = 1, 2, \dots, K. \quad (3.90)$$

The energy balance for the volume zone of a random packed bed, according to eq. [3.76], will now become:

$$\sum_{j=1}^N \overline{g_i s_j} + \sum_{k=1}^K \overline{g_i g_k} = A_{Random}, \quad \forall i = 1, 2, \dots, K. \quad (3.91)$$

### 3.9 Solving for the radiosities and temperatures

After obtaining the direct exchange areas for the  $N$  surface zones and  $K$  volume zones, the net heat emitted by each zone can now be determined. The net heat for the surface zones can be written as:

$$Q_{si} = \varepsilon_{si} \left( A_i E_{bsi} - \sum_{j=1}^N \overline{s_j s_i} J_{sj} - \sum_{k=1}^K \overline{g_k s_i} J_{gk} \right) \quad i = 1, 2, \dots, N. \quad (3.92)$$

And the net heat for the volume zones can be written as:

$$Q_{gi} = \varepsilon_{gi} \left( A_{g_i} E_{bgi} - \sum_{j=1}^N \overline{s_j g_i} J_{sj} - \sum_{k=1}^K \overline{g_k g_i} E_{bgk} \right) \quad i = 1, 2, \dots, K. \quad (3.93)$$

Since it was explained in chapter 2 that the volume zones are treated as surfaces due to the relative large size of the spheres compared to the wavelength of the electromagnetic radiation, eqns. (3.92) and (3.93) can be simplified by combining them for all  $N + K$

zones in the system:

$$Q_i = \varepsilon_i \left( A_i E_{bi} - \sum_{j=1}^{N+K} \overline{s_j s_i} J_j \right) \quad i = 1, 2, \dots, N + K. \quad (3.94)$$

According to Modest (2003), the radiosity of a surface zone can be written in terms of its black body radiation, net heat and emissivity:

$$J_i = E_{bi} - \frac{1 - \varepsilon_i}{A_i \varepsilon_i} Q_i \quad (3.95)$$

By substituting eq. (3.95) into eq. (3.94), it yields:

$$Q_i = \varepsilon_i A_i E_{bi} - \varepsilon_i \sum_{j=1}^{N+K} \overline{s_j s_i} E_{bj} + \varepsilon_i \frac{1 - \varepsilon_j}{A_j \varepsilon_j} \sum_{j=1}^{N+K} \overline{s_j s_i} Q_j \quad i = 1, 2, \dots, N + K. \quad (3.96)$$

The heat transfer and black-body radiation terms can be grouped together to obtain:

$$\left( Q_i - \varepsilon_i \frac{1 - \varepsilon_j}{A_j \varepsilon_j} \sum_{j=1}^{N+K} \overline{s_j s_i} Q_j \right) = \left( \varepsilon_i A_i E_{bi} - \varepsilon_i \sum_{j=1}^{N+K} \overline{s_j s_i} E_{bj} \right) \quad i = 1, 2, \dots, N + K. \quad (3.97)$$

In order to generalise eq. [3.97] even more, a Kronecker delta term  $\delta_{ij}$  will be added to apply a value of 1 to the necessary term when  $i = j$  and to apply a value of 0 when  $i \neq j$  to ensure the diagonal of the matrix containing the coefficients is correctly populated. Eq. [3.97] then becomes:

$$\sum_{j=1}^{N+K} \left( \frac{\delta_{ij}}{\varepsilon_i} - \frac{1 - \varepsilon_j}{A_j \varepsilon_j} \overline{s_j s_i} \right) Q_j = \sum_{j=1}^{N+K} (A_i \delta_{ij} - \overline{s_j s_i}) E_{bj} \quad i = 1, 2, \dots, N + K. \quad (3.98)$$

Since either the temperature or the heat will be specified for a particular zone and not both simultaneously, a 'switch' in the form of a coefficient  $c_i$  can be added to the equation to discriminate between the black-body radiation and the heat, depending on what was specified:

$$\begin{aligned} & \sum_{j=1}^{N+K} \left[ c_j \left( \frac{\delta_{ij}}{\varepsilon_i} - \frac{1 - \varepsilon_j}{A_j \varepsilon_j} \overline{s_j s_i} \right) Q_j \right] - \sum_{j=1}^{N+K} [(1 - c_j) (A_i \delta_{ij} - \overline{s_j s_i}) E_{bj}] \\ &= - \sum_{j=1}^{N+K} \left[ (1 - c_j) \left( \frac{\delta_{ij}}{\varepsilon_i} - \frac{1 - \varepsilon_j}{A_j \varepsilon_j} \overline{s_j s_i} \right) Q_j \right] \\ &+ \sum_{j=1}^{N+K} [c_j (A_i \delta_{ij} - \overline{s_j s_i}) E_{bj}] \quad i = 1, 2, \dots, N + K. \end{aligned} \quad (3.99)$$

With:

$$\begin{aligned} c_i &= 1 \text{ when } T_i \text{ is specified;} \\ c_i &= 0 \text{ when } Q_i \text{ is specified.} \end{aligned}$$

A system of the form  $\mathbf{Ax} = \mathbf{By}$  can be written from eq. [3.99], with  $\mathbf{A}$  and  $\mathbf{B}$  being  $K \times K$  matrices containing the coefficients for the two  $K \times 1$  vectors  $\mathbf{x}$  and  $\mathbf{y}$  containing the temperature and heat variables to be solved. Matrix  $\mathbf{A}$  is:

$$\sum_{j=1}^{N+K} \left[ c_j \left( \frac{\delta_{ij}}{\varepsilon_i} - \frac{1 - \varepsilon_j}{A_j \varepsilon_j} \overline{s_j s_i} \right) \right] - \sum_{j=1}^{N+K} [(1 - c_j) (A_i \delta_{ij} - \overline{s_j s_i})] \quad i = 1, 2, \dots, N + K. \quad (3.100)$$

Vector  $\mathbf{x}$  is:

$$c_i Q_i + (1 - c_i) E_{bi} \quad i = 1, 2, \dots, N + K. \quad (3.101)$$

Matrix  $\mathbf{B}$  is:

$$- \sum_{j=1}^{N+K} (1 - c_j) \left( \frac{\delta_{ij}}{\varepsilon_i} - \frac{1 - \varepsilon_j}{A_j \varepsilon_j} \overline{s_j s_i} \right) + \sum_{j=1}^{N+K} c_j (A_i \delta_{ij} - \overline{s_j s_i}) \quad i = 1, 2, \dots, N + K. \quad (3.102)$$

Vector  $\mathbf{y}$  is:

$$(1 - c_i) Q_i + c_i E_{bi} \quad i = 1, 2, \dots, N + K. \quad (3.103)$$

The system can be solved via matrix inversion:

$$\mathbf{x} = \mathbf{A}^{-1} \mathbf{B} \mathbf{y} \quad (3.104)$$

The applicable heat or temperature can then be extracted from the solved vector  $\mathbf{x}$ , depending on what was specified:

$$E_{bi} = x_i \text{ if } c_i = 0, \text{ or} \quad (3.105)$$

$$Q_i = x_i \text{ if } c_i = 1. \quad (3.106)$$

The temperature can then be calculated from the black-body radiation from:

$$T_i = \sqrt[4]{E_{bi} / \sigma} \quad (3.107)$$

### 3.10 Deriving the attenuation factor

In order to obtain the attenuation factor  $\kappa$  as used in the direct-exchange area equations for a bed filled with large mono-sized spheres for both a structured and a random packing, the view factor between the front and rear surfaces can be obtained for both an empty and a filled enclosure. The view factor between the front and rear surfaces is directly related to the radial attenuation factor (front to rear) in that it reflects the amount of emission leaving the front surface that actually reaches the rear surface. The attenuation factor is an important part of the Zonal Approach since it dictates the amount of energy transferred to the participating medium. The relation between the view factor and the attenuation factor will be illustrated in this section.

The definition of the direct-exchange factor between two surfaces is given by Modest (2003) as:

$$\overline{s_i s_j} = A_i F_{ij} \quad (3.108)$$

It can be rewritten to obtain:

$$F_{ij} = \frac{\overline{s_i s_j}}{A_i} \quad (3.109)$$

The direct-exchange area between two surface zones can now be substituted from eq. [3.45] into eq. [3.109]:

$$F_{ij} = \frac{1}{A_i} \int_{A_i} \int_{A_j} e^{-\kappa_{ij} S} \frac{\cos \theta_i \cos \theta_j}{\pi S^2} dA_j dA_i \quad (3.110)$$

$$F_{ij} \approx e^{-\kappa_{ij} S} \frac{1}{A_i} \int_{A_i} \int_{A_j} \frac{\cos \theta_i \cos \theta_j}{\pi S^2} dA_j dA_i \quad (3.111)$$

$$F_{ij} = e^{-\kappa_{ij} S} \frac{\overline{s_i s_j^*}}{A_i} \quad (3.112)$$

Where  $\overline{s_i s_j^*}$  denotes the direct-exchange area between the front and rear surfaces of an empty enclosure, i.e. without attenuation. Eq. [3.112] can be rewritten as:

$$F_{ij} = e^{-\kappa_{ij} S} F_{ij}^* \quad (3.113)$$

Where  $F_{ij}^*$  is the view factor between the front surface  $i$  and rear surface  $j$  in an empty enclosure, i.e. without attenuation. Eq. [3.113] also implies:

$$A_i F_{ij} = e^{-\kappa_{ij} S} A_i F_{ij}^* \quad (3.114)$$

$$\overline{s_i s_j} = e^{-\kappa_{ij} S} \overline{s_i s_j^*} \quad (3.115)$$

Since the view factor is distance dependent the attenuation factor can be derived at different cross-sectional positions in the bed which will make the attenuation factor dependent on

the distance from the front wall of the enclosure. The attenuation factor between a cross-sectional plane at distance  $i$  from the front wall and a cross-sectional plane at a distance  $j$  from the front wall will be:

$$\kappa_{ij} = \frac{1}{S} \int_0^S \kappa dS \quad (3.116)$$

The attenuation factor can be obtained using the above-mentioned method by using ray-tracing from a surface-to-surface solver from a typical CFD package such as Star-CCM+ to obtain the front-to-rear view factor both with and without attenuation.

### 3.11 Conduction Coupled to Radiation

Calculating thermal radiation only is mostly a theoretical exercise. Conduction is tied to thermal radiation inside a pebble bed and its essential to be able to couple the two heat transfer modes together in order to simulate heat transfer inside a packed pebble bed. The heat equation for thermal radiation only was given by eq. [3.94] as:

$$Q_{EJ,i} = \varepsilon_i A_i E_{bi} - \varepsilon_i \sum_{j=1}^N \overline{s_j s_i} J_j \quad (3.117)$$

With:

- $\varepsilon_i$  the emissivity for surface zone  $i$ .
- $A_i$  the surface area for surface zone  $i$ .
- $E_{bi}$  the black-body radiation for surface zone  $i$ .
- $\overline{s_j s_i}$  the direct-exchange area between surface zone  $i$  and surface zone  $j$ .
- $J_i$  the radiosity for surface zone  $j$ .

The Zonal Approach is a type of network approach, so it should correspond with the general heat equation derived from a thermal network for radiation, illustrated in figure 3.18, which is:

$$Q_{EJ,i} = \frac{E_{bi} - J_i}{(1 - \varepsilon_i)/\varepsilon_i A_i} = \sum_{j=1}^N \frac{J_i - J_j}{1/A_i F_{ij}} \quad (3.118)$$

With  $F_{ij}$  the view factor from zone  $i$  to zone  $j$ .

The left-hand side of the equation implies that  $E_{bi} - J_i$  is the driving potential over the surface resistance  $\frac{1-\varepsilon_i}{\varepsilon_i A_i}$ , while the right-hand side of the equation implies that the net heat of zone  $i$  is the sum of the differences of the radiosities between zone  $i$  and the other zones

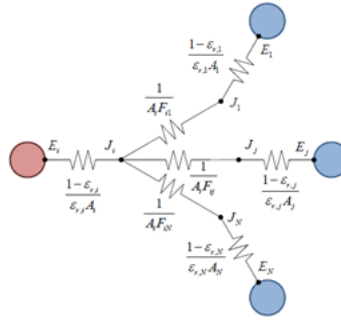


FIGURE 3.18: Thermal radiation network from surface  $i$  (Rousseau et al., 2012).

(which serves as the driving potential) while the space resistance between the two zones is the direct-exchange areas.

Let eq. [3.118] serve as the starting point:

$$\frac{E_{bi} - J_i}{(1 - \varepsilon_i)/\varepsilon_i A_i} = \sum_{j=1}^N \frac{J_i - J_j}{1/A_i F_{ij}} \quad (3.119)$$

Remembering that  $A_i F_{ij} = \overline{s_j s_i}$  is the direct-exchange areas, and by expanding the right-hand side, eq. [3.119] becomes:

$$\frac{E_{bi} - J_i}{(1 - \varepsilon_i)/\varepsilon_i A_i} = \sum_{j=1}^N \overline{s_i s_j} J_i - \sum_{j=1}^N \overline{s_i s_j} J_j \quad (3.120)$$

By expanding the left-hand side of eq. [3.120] it becomes:

$$\frac{\varepsilon_i A_i E_{bi}}{(1 - \varepsilon_i)} - \frac{\varepsilon_i A_i J_i}{(1 - \varepsilon_i)} = \sum_{j=1}^N \overline{s_i s_j} J_i - \sum_{j=1}^N \overline{s_i s_j} J_j \quad (3.121)$$

Multiplying by  $(1 - \varepsilon_i)$ :

$$\begin{aligned}
 \varepsilon_i A_i E_{bi} - \varepsilon_i A_i J_i &= (1 - \varepsilon_i) \sum_{j=1}^N \overline{s_i s_j} J_i - (1 - \varepsilon_i) \sum_{j=1}^N \overline{s_i s_j} J_j \\
 \varepsilon_i A_i E_{bi} - \varepsilon_i A_i J_i &= \sum_{j=1}^N \overline{s_i s_j} J_i - \varepsilon_i \sum_{j=1}^N \overline{s_i s_j} J_i - \sum_{j=1}^N \overline{s_i s_j} J_j + \varepsilon_i \sum_{j=1}^N \overline{s_i s_j} J_j \\
 \varepsilon_i A_i E_{bi} - \varepsilon_i \sum_{j=1}^N \overline{s_i s_j} J_j &= \sum_{j=1}^N \overline{s_i s_j} J_i - \varepsilon_i \sum_{j=1}^N \overline{s_i s_j} J_i - \sum_{j=1}^N \overline{s_i s_j} J_j + \varepsilon_i A_i J_i \\
 \varepsilon_i A_i E_{bi} - \varepsilon_i \sum_{j=1}^N \overline{s_i s_j} J_j &= \left( \sum_{j=1}^N \overline{s_i s_j} J_i - \sum_{j=1}^N \overline{s_i s_j} J_j \right) + \left( \varepsilon_i A_i J_i - \varepsilon_i \sum_{j=1}^N \overline{s_i s_j} J_i \right)
 \end{aligned} \tag{3.122}$$

Remembering that  $\sum_{j=1}^N \overline{s_i s_j} = A_i$  and that  $\overline{s_i s_j} = \overline{s_j s_i}$  due to reciprocity, eq. [3.122] now becomes:

$$\begin{aligned}
 \varepsilon_i A_i E_{bi} - \varepsilon_i \sum_{j=1}^N \overline{s_i s_j} J_j &= \left( \sum_{j=1}^N \overline{s_i s_j} J_i - \sum_{j=1}^N \overline{s_i s_j} J_j \right) + \left( \varepsilon_i A_i J_i - \varepsilon_i \sum_{j=1}^N \overline{s_i s_j} J_i \right) \\
 \varepsilon_i A_i E_{bi} - \varepsilon_i \sum_{j=1}^N \overline{s_j s_i} J_j &= \left( \sum_{j=1}^N \overline{s_i s_j} J_i - \sum_{j=1}^N \overline{s_i s_j} J_j \right) + (\varepsilon_i A_i J_i - \varepsilon_i A_i J_i) \\
 \varepsilon_i A_i E_{bi} - \varepsilon_i \sum_{j=1}^N \overline{s_j s_i} J_j &= \left( \sum_{j=1}^N \overline{s_i s_j} J_i - \sum_{j=1}^N \overline{s_i s_j} J_j \right)
 \end{aligned} \tag{3.123}$$

This shows that the general equation used by the Zonal Approach for the heat balance or zone  $i$ , as shown in eq. [3.117], is consistent with the well-known heat equation derived from the thermal radiation network for zone  $i$ , as shown in eq. [3.118] and can be used interchangeably as needed.

Figure 3.18 showed the thermal network for radiation only. Conduction connects to the surface node and can thus be summed with the thermal radiation heat to obtain the total heat equation (Incropera et al., 2007). This is illustrated in figure 3.19. Eq. [3.117], [3.118] and [3.119] all describe the energy balance at the nodal point  $J_i$ , but when conduction is present the energy balance must be described at the surface node, which is nodal point  $E_{bi}$ . The combined heat equation for radiation and conduction now become:

$$Q_i = \frac{E_{bi} - J_i}{(1 - \varepsilon_i)/\varepsilon_i A_i} + \sum_{k=1}^m \frac{1}{R_{ik}} (T_i - T_k) \tag{3.124}$$



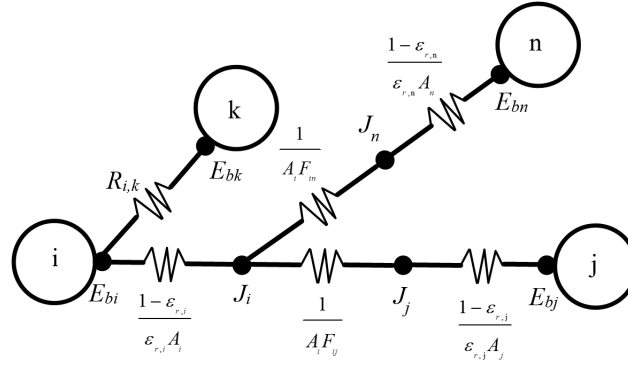


FIGURE 3.19: Combined conduction and radiation network.

Isolating the radiosity of surface  $i$ , eq. [3.124] now becomes:

$$J_i = E_{bi} - \frac{\varepsilon_i A_i}{(1 - \varepsilon_i)} \left[ Q_i - \sum_{k=1}^m \frac{1}{R_{ik}} (T_i - T_k) \right] \quad (3.125)$$

Combining eq. [3.118] and eq. [3.124] it becomes:

$$\begin{aligned} Q_i &= Q_{EJ,i} + \sum_{k=1}^m \frac{1}{R_{ik}} (T_i - T_k) \\ Q_{EJ,i} &= Q_i - \sum_{k=1}^m \frac{1}{R_{ik}} (T_i - T_k) \end{aligned} \quad (3.126)$$

Eq. [3.126] can be substituted in eq. [3.117] to obtain:

$$Q_i - \sum_{k=1}^m \frac{1}{R_{ik}} (T_i - T_k) = \varepsilon_i \left( A_i E_{bi} - \sum_{j=1}^N \overline{s_j s_i} J_j \right) \quad (3.127)$$

By substituting eq. [3.125] in eq. [3.127] it leads to:

$$Q_i - \sum_{k=1}^m \frac{1}{R_{ik}} (T_i - T_k) = \varepsilon_i \left( A_i E_{bi} - \sum_{j=1}^N \overline{s_j s_i} \left\{ E_{bj} - \frac{\varepsilon_j A_j}{(1 - \varepsilon_j)} \left[ Q_j - \sum_{k=1}^m \frac{1}{R_{jk}} (T_j - T_k) \right] \right\} \right) \quad (3.128)$$

Finally by rearranging eq. [3.128] the combined conduction-radiation heat equation becomes:

$$\begin{aligned}
0 = & \left\{ -Q_i + \varepsilon_i \sum_{j=1}^N \left[ \frac{\varepsilon_j A_j}{\overline{s_j s_i} (1 - \varepsilon_j)} Q_j \right] \right\} + \left\{ \sum_{k=1}^m \left[ \frac{1}{R_{ik}} (T_i - T_k) \right] \right. \\
& \left. - \varepsilon_i \sum_{j=1}^N \left[ \frac{\varepsilon_j A_j}{\overline{s_j s_i} (1 - \varepsilon_j)} \sum_{k=1}^m \left( \frac{1}{R_{jk}} (T_j - T_k) \right) \right] \right\} + \left( \varepsilon_i A_i E_{bi} - \varepsilon_i \sum_{j=1}^N \overline{s_j s_i} E_{bj} \right)
\end{aligned} \quad (3.129)$$

For ease of implementation eq. [3.129] can be split into three parts. Part 1 represents the combined heat term for conduction and radiation; Part 2 represents the thermal radiation temperature component; and part 3 represents the conduction temperature component, or:

$$\begin{aligned}
\text{Part1} &= \left( -Q_i + \varepsilon_i \sum_{j=1}^N \left[ \frac{\varepsilon_j A_j}{\overline{s_j s_i} (1 - \varepsilon_j)} Q_j \right] \right) \\
\text{Part1} &= \sum_{j=1}^N \left( -\delta_{ij} + \varepsilon_i \left[ \frac{\varepsilon_j A_j}{\overline{s_j s_i} (1 - \varepsilon_j)} \right] \right) Q_j
\end{aligned} \quad (3.130)$$

$$\begin{aligned}
\text{Part2} &= \left( \varepsilon_i A_i E_{bi} - \varepsilon_i \sum_{j=1}^N \overline{s_j s_i} E_{bj} \right) \\
\text{Part2} &= \sum_{j=1}^N (\varepsilon_i A_i \delta_{ij} - \varepsilon_i \overline{s_j s_i}) E_{bj}
\end{aligned} \quad (3.131)$$

$$\text{Part3} = \left( \sum_{k=1}^m \left[ \frac{1}{R_{ik}} (T_i - T_k) \right] - \varepsilon_i \sum_{j=1}^N \left\{ \frac{\varepsilon_j A_j}{\overline{s_j s_i} (1 - \varepsilon_j)} \sum_{k=1}^m \left[ \frac{1}{R_{jk}} (T_j - T_k) \right] \right\} \right) \quad (3.132)$$

In order to simplify Part 3 the conduction heat transfer associated with a node can be written as:

$$Q_{ci} = \sum_{k=1}^m \frac{1}{R_{ik}} (T_i - T_k)$$

Eq. [3.132] can then be rewritten as:

$$\begin{aligned}
\text{Part3} &= Q_{ci} - \varepsilon_i \sum_{j=1}^N \left( \frac{\varepsilon_j A_j}{\overline{s_i s_j} (1 - \varepsilon_j)} Q_{cj} \right) \\
&= \sum_{j=1}^N \left( \delta_{ij} - \varepsilon_i \overline{s_i s_j} \frac{\varepsilon_j A_j}{1 - \varepsilon_j} \right) Q_{cj}
\end{aligned} \quad (3.133)$$

### 3.12 MSUC Conduction Component

The thermal resistance can be described by the conduction component of the MSUC model. The MSUC model was specifically derived to describe the effective thermal conductivity of a packed pebble bed reactor and the objective of the current thermal radiation model was to replace the preliminary thermal radiation component included in the MSUC model with a more fundamental approach presented in this study. The MSUC model can be viewed in detail in Van Antwerpen (2009) and Van Antwerpen et al. (2012).

The conduction component for the MSUC model is calculated using an effective thermal resistance. This effective thermal resistance consists of various thermal resistances in parallel and series in different regions, illustrated in figure 3.20. It is based on two half-spheres which is subdivided into three radial positions: The inner-, middle- and outer positions. Each of these unique regions represents different heat transfer mechanisms and when joined together forms the joint thermal resistance  $R_j$ .

Two different types of networks can be set up: A rough contact network (RCN) and a Hertzian contact network (HCN), depending on the spheres' smoothness and Brinell hardness numbers. The HCN assumes smooth solid surfaces. The networks can be applied to three different packing regions in a random packed bed which are the wall-, near-wall- and bulk regions as shown in figure 3.21.

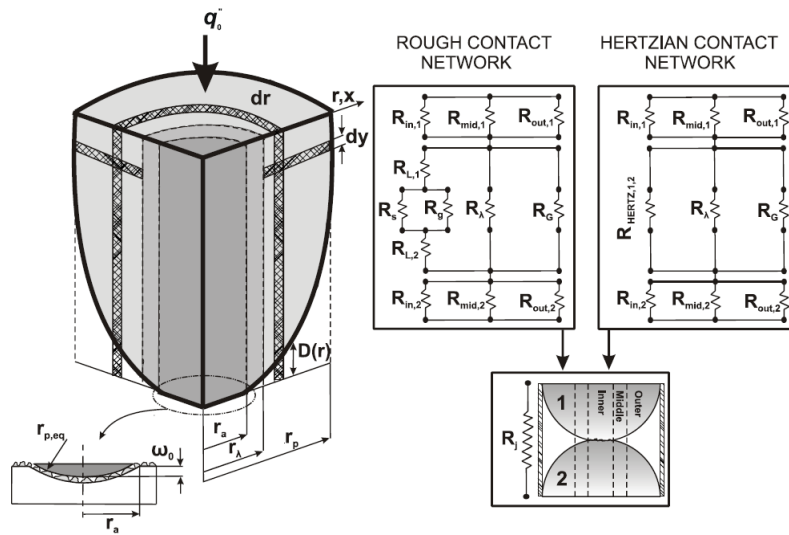


FIGURE 3.20: Different conduction thermal resistances of the MSUC model (Van Antwerpen et al., 2012).

A summary of the different thermal resistances shown in figure 3.20 for the RCN are:

- The inner solid material resistance  $R_{in,1,2}$  which is a summation of  $R_{in,1}$  and  $R_{in,2}$ .

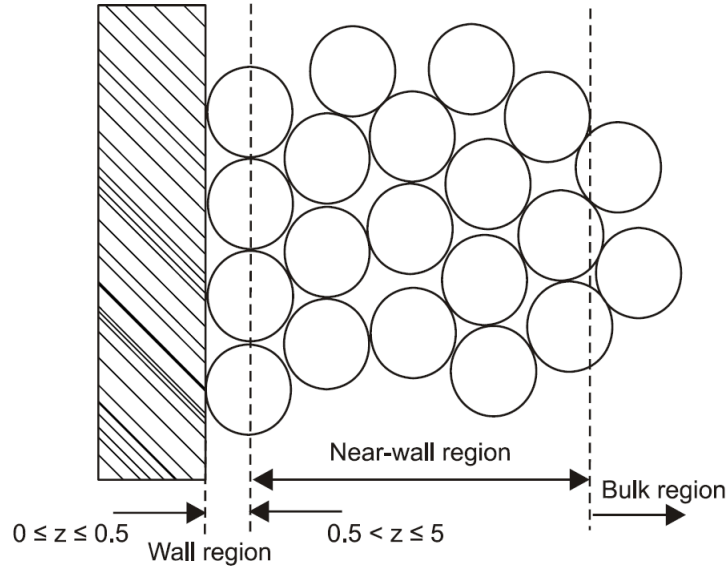


FIGURE 3.21: The different packing regions inside the annulus of a random packed pebble bed.

- The macro-contact constriction/spreading resistance  $R_{L,1,2}$  which is a summation of  $R_{L,1}$  and  $R_{L,2}$ .
- The micro-contact constriction/spreading resistance  $R_{S,1,2}$  which is a summation of  $R_{S,1}$  and  $R_{S,2}$ .
- The interstitial gas resistance in the micro-gap  $R_g$ .
- The middle solid material resistance  $R_{mid,1,2}$  which is a summation of  $R_{mid,1}$  and  $R_{mid,2}$ .
- The resistance of the interstitial gas in the Knudsen regime, also known as the Smoluchowski effect of the micro-gap  $R_\lambda$ .
- The outer solid material resistance  $R_{out,1,2}$  which is a summation of  $R_{out,1}$  and  $R_{out,2}$ .
- Resistance of the interstitial gas in the macro-gap  $R_G$

For the HCN the resistances  $R_{L,1,2}$ ,  $R_S$  and  $R_g$  are replaced by the Hertzian micro-contact  $R_{HERTZ,1,2}$ .

The combined conduction-radiation model forms a system of non-linear equations with regards to the temperature. Unlike the case where only thermal radiation is present the system can't be directly solved for the unknown black-body radiation terms due to the conduction component containing a first-order temperature component, necessitating the black-body term to be solved as a fourth-order temperature component. An iterative solver

such as the Newton-Raphson method can be employed to solve the simultaneous conduction and radiation heat transfer equation given in eq. [3.129].

### **3.13 Summary**

In this chapter the basic Zonal Approach was discussed. The relevant shortcomings in applying the Zonal Approach to a packed bed filled with mono-sized spheres were identified and the model was adapted by addressing these shortcomings for both a structured and a random-packed bed by adapting the Zonal Approach for surface exchange. The surface exchange was first done for an enclosure filled with a structured bed after which it was adapted for a random packed bed. An updated energy balance based on the adapted direct exchange areas was also proposed. The solution methodology of the thermal radiation was discussed as well as its coupling to the conduction component of the MSUC model.

## 4 Comparison of Thermal Radiation Results

### 4.1 Introduction

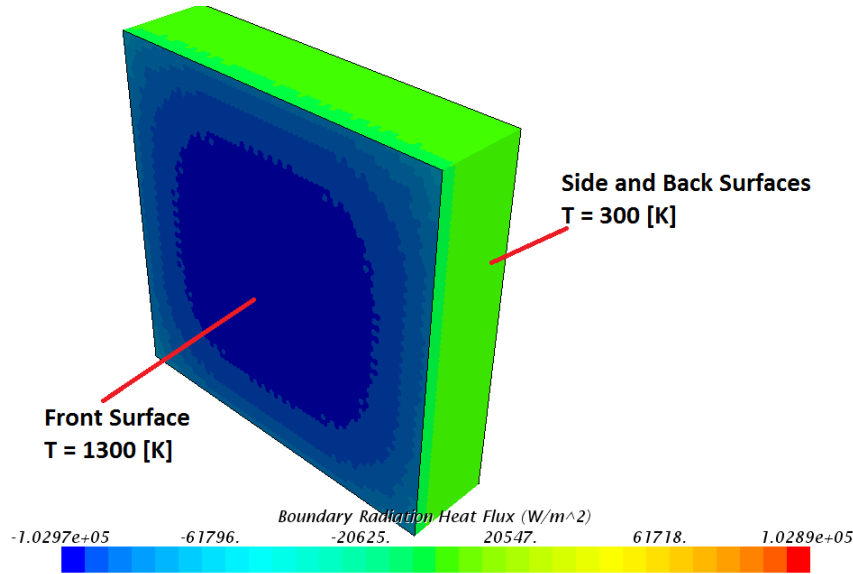
In this chapter the results of the Zonal Approach will be compared with the simulated results of an industry-standard Computational Fluid Dynamics (CFD) solver Star-CCM+ for the cases involving only thermal radiation and with the experimental results of the Near-wall Effective Thermal Conductivity Transfer Facility (NWTCTF). The first part of this chapter will look at thermal radiation only, while conduction will be added to the Zonal Approach in the second part of the chapter. First an enclosure without a participating medium will be evaluated to establish the validity of the exchange model. Thereafter an enclosure with a structured bed, an enclosure filled with the bulk region of a random bed and an enclosure filled with the wall- and near-wall region of the bed will be evaluated and compared with the CFD solver. Finally the conduction component of the Multi-Sphere Unit Cell Model (MSUC) will be added to the Zonal Approach and its results will be compared with the experimental results of both the simple cubic and random packing experimental setups.

### 4.2 Solving the model without a participating medium

Before applying the Zonal Approach to an enclosure with a participating medium, it is a good idea to first test the model on an empty enclosure. An enclosure of dimensions  $16 \times 16 \times 4D_p$  and an enclosure of  $10 \times 10 \times 10D_p$  was set up in Star-CCM+ and compared to the zonal model's results. Figure 4.1 shows the model within Star-CCM+. The thermal radiation heat transfer was solved within Star-CCM+ using a surface-to-surface solver. The boundary conditions for the  $16 \times 16 \times 4D_p$  enclosure was a front temperature of 1300K and side and rear surface temperatures of 300K. For the  $10 \times 10 \times 10D_p$  enclosure the front surface temperature was 1200K while the side surfaces were adiabatic and the rear surface was 300K. The results are shown in table 4.1. The difference in results between the two models were negligible and it was assumed the surface exchange solved properly.

TABLE 4.1: Results comparison between Zonal Approach without a participating medium and Star-CCM+.

		Front Heat [W]	Rear Heat [W]	Side Heat [W]	Energy Balance [W]	Diff. [%]
16x16x4Dp	Zonal	37371	-22569	-14802	0	0.04
	CFD	37357.28	-22629.22	-14727.6	-0.462	
10x10x10Dp	Zonal	17905	-17905	0	0	0.10
	CFD	17922.28	-17833.38	-88.74	-0.1625	

FIGURE 4.1: A surface-to-surface radiation simulation of an enclosure of dimensions 16x16x4  $D_p$  without a participating medium.

## 4.3 Solving the model with a participating medium

### 4.3.1 Thermal Radiation in a Simple Cubic Bed

#### 4.3.1.1 The Attenuation Factor in a Simple Cubic Bed

The simple cubic structure will form the baseline for the random packing's direct exchange areas from an emission perspective. For this study only the radial (i.e. front to rear or hot surface to cold surface) attenuation factor will be derived. The basis for deriving the attenuation factor is given in eq. [3.113] and requires the calculation of the front to rear view factor in an enclosure both with and without a medium.

The radial view factor was calculated using ray tracing for various rectangular enclosures, differing in cross-sectional size as well as in radial thickness (distance between front to rear). Plots of the attenuation factors are given in figure 4.2.

An interesting phenomenon in a structured bed is that spheres between two exchanging

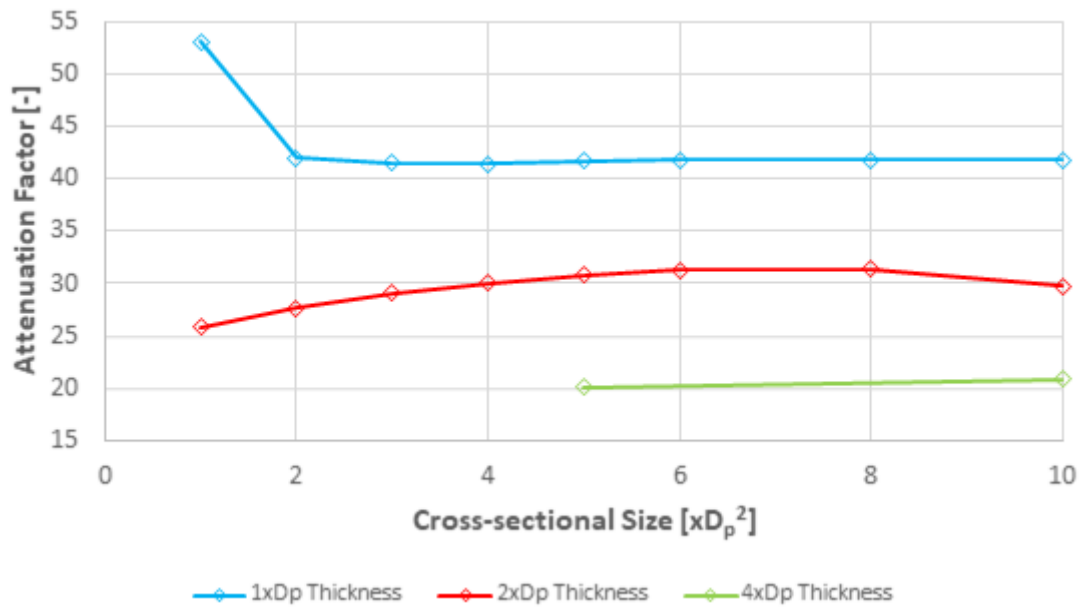


FIGURE 4.2: Attenuation factor for various cross-sectional sizes and various radial thicknesses for a simple cubic bed.

zones (either surface or volume zones) can completely obscure the effect of other zones in between these exchanging zones by blocking the view to those spheres. This will affect the derived attenuation factor since not all spheres in the radial direction will participate in the exchange between zones. Figure 4.2 shows that the radial attenuation factors vary with thickness due to this phenomenon, with the attenuation factor decreasing as the radial thickness increase. This is because the spheres located behind the first row of spheres participate much less in the radial absorption between the front and rear wall.

Only the radial attenuation factor is derived even though exchange with an axial component (i.e. diagonal) also occurs inside the enclosure. All of the above-mentioned influence the derived attenuation factor. It must be kept in mind that although it is possible to account for all the possible effects influencing the attenuation factor, it doesn't necessarily result in simplicity, which is the aim of this study. It will be much simpler if a single effective attenuation factor can be used in a bed if the porosity remains constant. Tables 4.2 to 4.5 shows the attenuation factors for the simple cubic bed (with subdivided control volumes or zones) necessary to match the CFD simulations within 1%. It is evident that a fairly constant attenuation factor for all cases can be chosen to match the simulated results to at least within 20%.

The derivation of the attenuation factor for a simple cubic bed is not as straightforward as it seems due to its structured nature causing phenomena which makes it more difficult to ascertain the attenuation factor. However, an averaged overall attenuation factor can be determined by comparing the Zonal Approach results with the CFD results and adjusting



the attenuation factor in the former accordingly.

#### 4.3.1.2 Comparison of Thermal Radiation Results in a Simple Cubic Bed

The results from various cases of the Zonal Approach was compared to the results from the CFD package Star-CCM+. The surface-to-surface solver within Star-CCM+ was used within a fluid volume (which was non-participating) to ensure that only surfaces was used in order to eliminate the effect of solid conduction. Grey thermal radiation was used. In all cases a surface emissivity of 0.8 was used with a rear surface temperature of 300K, while the front surface temperature was varied. The spheres and the side surfaces of the enclosure was specified as adiabatic.

The first question that was asked was if subdivision of the zones used in the Zonal Approach was necessary. In order to investigate this question the default size of a zone ( $1 \times D_p^2$  for surface zones and  $1 \times D_p^3$  for volume zones) was used first. The results of these simulations are given in tables 4.2 to 4.5, and all these enclosures were  $1 \times D_p$  from front to rear (radial thickness).

The results of the Zonal Approach with no subdivision compared poorly with the results from the CFD simulations even when the attenuation factor was adjusted. Although the thermal radiation results in Rousseau et al. (2012) and Rousseau et al. (2014) compared well to the results simulated in a CFD package using full-sized spheres, it must be remembered that the CFD simulation model was setup as a solid model with the solid conduction of the spheres set to a very high value of  $k_s = 10\,000\text{W/m/K}$ . This was to ensure that all the spheres had isothermal surfaces. Van Antwerpen et al. (2012) mentioned correction factors to compensate for the non-isothermal sphere surfaces which is not ideal. Although isothermal surface temperatures of spheres inside a packed bed can be assumed in certain cases it can't be assumed in all cases, necessitating a model that can accommodate non-isothermal surface temperatures without correction factors. The spheres in a pebble bed reactor will generate heat that will cause a more uniform temperature distribution on the sphere's surface, but this can be seen as a simplification of the suggested model rather than a limiting factor, which ensures a better fundamental approach which can also broaden the scope of application of the model.

A single volume zone is shown in figure 4.3. If the front surface temperature is set to 600K and the rear surface temperature to 300K while the sphere and the side surfaces are kept adiabatic, the front half of the sphere will increase in temperature much more than the rear half of the sphere since only the front half of the sphere 'sees' the front surface. Similarly the same would have happened if the top surface was hot and the rear surface colder while the rest was adiabatic. This implies that emission and reception of incident radiation is direction dependent. In order to accommodate non-isothermal conditions on

TABLE 4.2: Results comparison between the Zonal Approach with and without subdivision of the control volumes and the CFD simulation for a  $1 \times D_p$  radially thick simple cubic bed, with a 600K front surface temperature.

	<b>CFD Front Heat [W]</b>	<b>Zonal No Subd Front Heat [W]</b>	<b>Diff [%]</b>	<b>Zonal With Subd Front Heat [W]</b>	<b>Diff [%]</b>	<b>Matching Atten. <math>\kappa</math></b>
1x1Dp	2.32	10.16	537.9	1.18	-48.8	39.0
5x5Dp	88.034	226.42	357.2	67.527	-23.3	36.5
8x8Dp	239.66	546.15	328.3	178.96	-25.2	35.5
10x10Dp	364.5	833.66	329.0	282.9	-22.3	36.3

TABLE 4.3: Results comparison between the Zonal Approach with and without subdivision of the control volumes and the CFD simulation for a  $1 \times D_p$  radially thick simple cubic bed, with a 1000K front surface temperature.

	<b>CFD Front Heat [W]</b>	<b>Zonal No Subd Front Heat [W]</b>	<b>Diff [%]</b>	<b>Zonal With Subd Front Heat [W]</b>	<b>Diff [%]</b>	<b>Matching Atten. <math>\kappa</math></b>
1x1Dp	17.11	82.94	858.0	9.64	-43.6	41
5x5Dp	690.55	1848.46	367.7	551.27	-20.2	37.5
8x8Dp	1879.51	4458.64	337.34	1461.00	-22.2	36.5
10x10Dp	2864.8	6805.84	337.62	2309.70	-19.4	37.0

TABLE 4.4: Results comparison between the Zonal Approach with and without subdivision of the control volumes and the CFD simulation for a  $1 \times D_p$  radially thick simple cubic bed, with a 1500K front surface temperature.

	<b>CFD Front Heat [W]</b>	<b>Zonal No Subd Front Heat [W]</b>	<b>Diff [%]</b>	<b>Zonal With Subd Front Heat [W]</b>	<b>Diff [%]</b>	<b>Matching Atten. <math>\kappa</math></b>
1x1Dp	85.68	422.63	858.0	49.27	-42.5	41.0
5x5Dp	3479.82	9419.18	367.7	2809.10	-19.3	37.5
8x8Dp	9473.18	22719.80	337.34	7444.90	-21.4	36.8
10x10Dp	14449.00	34680.33	337.62	11769.00	-18.5	37.5

TABLE 4.5: Results comparison between the Zonal Approach with and without subdivision of the control volumes and the CFD simulation for a  $1 \times D_p$  radially thick simple cubic bed, with a 2000K front surface temperature.

	CFD Front Heat [W]	Zonal No Subd Front Heat [W]	Diff [%]	Zonal With Subd Front Heat [W]	Diff [%]	Matching Atten. $\kappa$
1x1Dp	269.64	1337.18	596.0	155.87	-42.2	41.5
5x5Dp	10974.14	29801.86	371.6	8887.90	-19.0	37.5
8x8Dp	29872.64	71884.46	340.7	23555.00	-21.1	36.8
10x10Dp	45579	109727.05	340.7	37238.00	-18.3	37.5

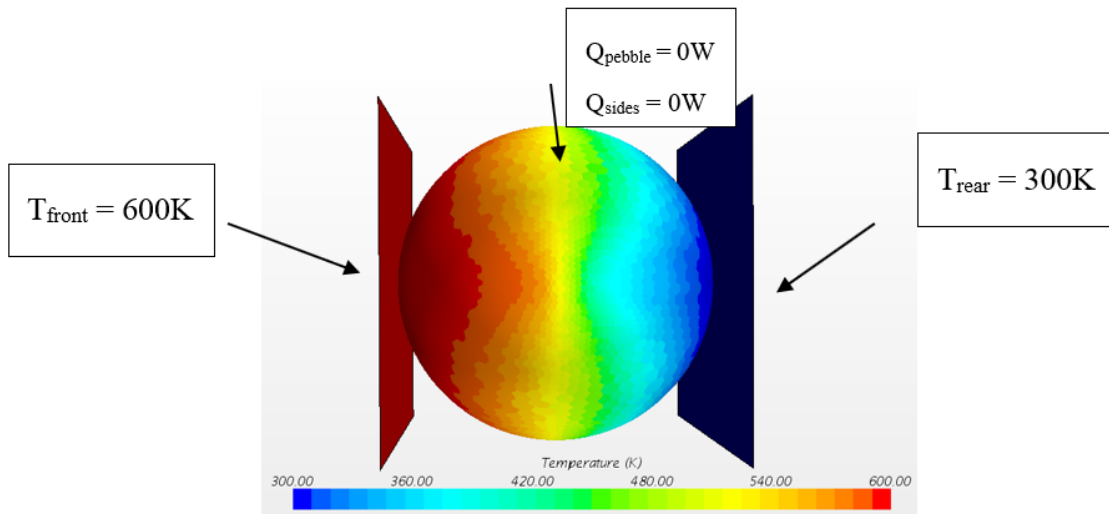


FIGURE 4.3: A single simple cubic control volume or volume zone with a heated front surface and a cold rear surface.

the surface of a sphere it must be subdivided into eight equal sections: four facing forward and four facing backward. The emission of each section will now be an eighth of the original sphere's emission, but only in the direction of its surface normal. When these modifications are made to the Zonal Approach the results resemble the results of the CFD simulations more closely.

Figure 4.4 shows the resultant front to rear temperature plot for the CFD simulation, the Zonal Approach with subdivision and the Zonal Approach without subdivision of the control volumes. Even though the predicted temperature for the Zonal Approach without subdivision is lower than for the Zonal Approach with subdivision, the calculated heat for the Zonal Approach without subdivision is much higher than for the subdivided case due to the sphere emitting in all  $4\pi$  directions as opposed to the subdivided control volume only emitting forward in  $\pi/2$  directions, as can be seen in table 4.2.

For the subdivided zones the effect of a change in cross-sectional size was investigated first.

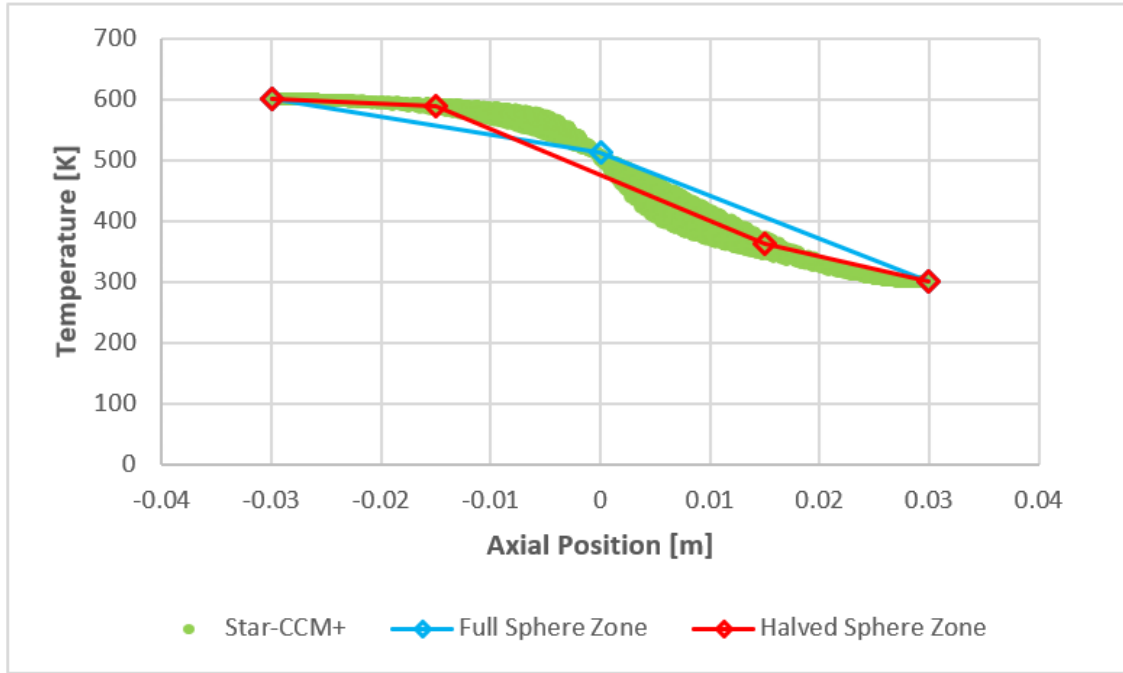


FIGURE 4.4: Temperature plot of the  $1 \times 1 \times 1 D_p$  enclosure comparing the front to rear temperature of the CFD simulation, the subdivided Zonal Approach and the non-subdivided Zonal Approach.

The radial thickness was  $1 \times D_p$  throughout. The cross-sectional size of the enclosure varied between  $1 D_p \times 1 D_p$  and  $10 D_p \times 10 D_p$  and the emissivity was  $\epsilon = 0.8$ . The temperature of the front surface of the enclosure varied between 600K and 2000K. The difference between the results of the Zonal Approach and the results from the CFD model using the derived attenuation factor of  $\kappa = 41.7$  was generally around 20%, with the smallest enclosure under-predicting the results by between 40-50%. When the attenuation factor is adjusted to match the results within 1%, the average attenuation factor for all cross-sectional sizes change to a minimum of  $\kappa = 36.8$  for the 600K case and to a maximum of  $\kappa = 38.3$  for the 2000K case.

The effect of thickness was also investigated by varying the thickness of a  $10 D_p \times 10 D_p$  and a  $5 D_p \times 5 D_p$  cross-sectional enclosure between  $1 \times D_p$  and  $10 \times D_p$ . The temperature varied between 600K and 2000K and the emissivity was  $\epsilon = 0.8$ . The results are shown in tables 4.6 to 4.9. The heat transferred through the bed decreased as the bed thickness increased due to the higher thermal resistance caused by the increase in radial thickness. When the derived attenuation factor of  $\kappa = 41.7$  was used, the results were under-predicted by the Zonal Approach by between 35-40%. The required attenuation factor to match all the different thickness case studies to within 1% of the results from the CFD simulation was  $\kappa = 34.0$ , with the exception of the  $1 \times D_p$  thickness case, which required an attenuation factor of  $\kappa = 37.5$  to match it to within 1%.

TABLE 4.6: Comparison between results from Zonal Approach and CFD model for various radial thicknesses of a simple cubic bed with a front surface temperature of 600K.

	Radial Thickness [xDp]	CFD Front Heat [W]	Zonal With Subd Front Heat [W]	Diff [%]	Matching Atten. $\kappa$
<i>5x5Dp</i>	2	55.04	34.51	-37.2	34.0
	4	33.00	19.46	-40.9	34.0
<i>10x10Dp</i>	2	245.22	148.74	-39.3	34.0
	4	139.32	455.00	229.9	34.0
	10	108.09	248.34	809.5	34.0

TABLE 4.7: Comparison between results from Zonal Approach and CFD model for various radial thicknesses of a simple cubic bed with a front surface temperature of 1000K.

	Radial Thickness [xDp]	CFD Front Heat [W]	Zonal With Subd Front Heat [W]	Diff [%]	Matching Atten. $\kappa$
<i>5x5Dp</i>	2	432.24	281.69	-34.8	34.0
	4	259.45	158.89	-38.8	34.0
<i>10x10Dp</i>	2	1930.80	1214.20	-37.0	34.0
	4	1095.47	3722.30	241.7	34.0
	10	566.45	2027.40	261.8	34.0

TABLE 4.8: Comparison between results from Zonal Approach and CFD model for various radial thicknesses of a simple cubic bed with a front surface temperature of 1500K.

	Radial Thickness [xDp]	CFD Front Heat [W]	Zonal With Subd Front Heat [W]	Diff [%]	Matching Atten. $\kappa$
<i>5x5Dp</i>	2	2178.53	1435.4	-34.1	34.3
	4	1308.58	809.64	-38.1	34.0
<i>10x10Dp</i>	2	9726.09	6187.40	-36.4	34.0
	4	5517.76	18968.00	244.8	35.0
	10	2848.61	10331.00	262.7	34.0

TABLE 4.9: Comparison between results from Zonal Approach and CFD model for various radial thicknesses of a simple cubic bed with a front surface temperature of 2000K.

	Radial Thickness [xDp]	CFD Front Heat [W]	Zonal With Subd Front Heat [W]	Diff [%]	Matching Atten. $\kappa$
<b>5x5Dp</b>	2	6871.62	4541.5	-33.9	34.3
	4	4128.08	2561.7	-37.9	34.0
<b>10x10Dp</b>	2	30669.81	19577.0	-36.2	34.0
	4	17396.22	11255.0	-35.2	35.5
	10	8977.49	32687.0	262.5	34.0

#### 4.3.1.3 Random Bed Attenuation Factor

A random packed bed consisting of mono-sized spheres was packed using the Discrete Element Modelling feature within the Star-CCM+ software package. The bed was a cubic box with dimensions of 30 ball diameters ( $1.8m$ ) per side, shown in figure 4.5. A  $0.45m$  deep square section was cut from the center of one of the bed's sides. This section was then sliced into 15 slices half a ball diameter ( $30mm$ ) thick, and the view factors were calculated from the front to the rear of each side, illustrated in figure 4.6. The spheres were then removed and the view factors were again calculated from the front to the rear of each slice. Eq. [3.113] was used to derive the attenuation factor by using the view factors between the front and rear of each slice with spheres present ( $F_{ij}$ ) and without spheres present ( $F_{ij}^*$ ). It must be noted that only the surface areas between the holes made by the spheres on the front and rear surfaces of each slice were used in calculating the view factors, not the total cross-sectional area. This is illustrated in figure 4.7.

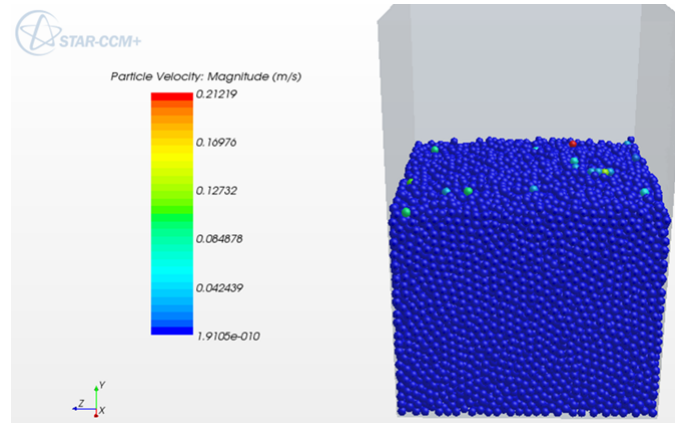


FIGURE 4.5: The  $30 \times 30 \times 30D_p$  bed being packed using the DEM solver of Star-CCM+.

The aim was to obtain the attenuation factor as a function of the distance from the wall.

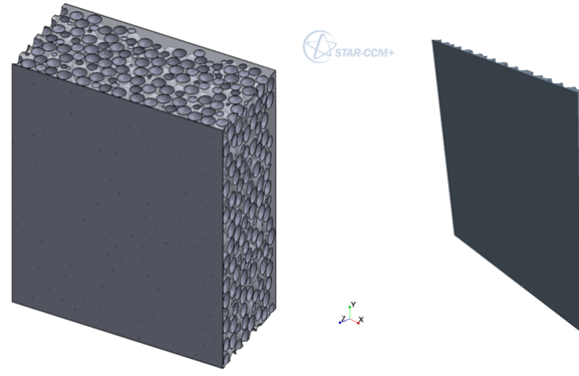


FIGURE 4.6: The section made from the one wall of the packed bed to derive the radial attenuation factors from the wall. One  $0.5 \times D_p$  thick slice is shown on the right.

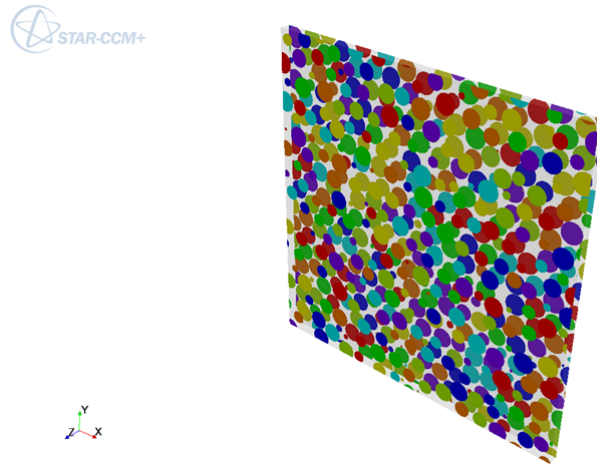


FIGURE 4.7: Empty slice used to calculate the view factor without the spheres present. Notice the holes (colored rings) in the front and rear surfaces.

According to Van Antwerpen et al. (2012) the packing regions of a random bed consist of 3 regions which is illustrated in figure 3.21 and listed as:

1. The wall region, which is from the wall to a distance of  $0.5 \times D_p$  from the wall;
2. The near-wall region, which is between  $0.5 \times D_p$  and  $5 \times D_p$  from the wall;
3. The bulk region, which is farther than  $5 \times D_p$  from the wall.

The cut section was 15 slices deep and each slice was half a ball diameter ( $0.5 \times D_p$ ) thick which meant the cut section was 7.5 ball diameters deep and went through all three regions. A study was done to determine at which cross-sectional area the attenuation factor became independent of the square cross-sectional area. The cross-sectional size was varied between  $1 \times D_p$  per side and  $18 \times D_p$  per side, and it was found that the view factors converged at a cross-sectional area of  $16 \times D_p$  per side. Figure 4.8 gives the view factors for various cross-sectional sizes.

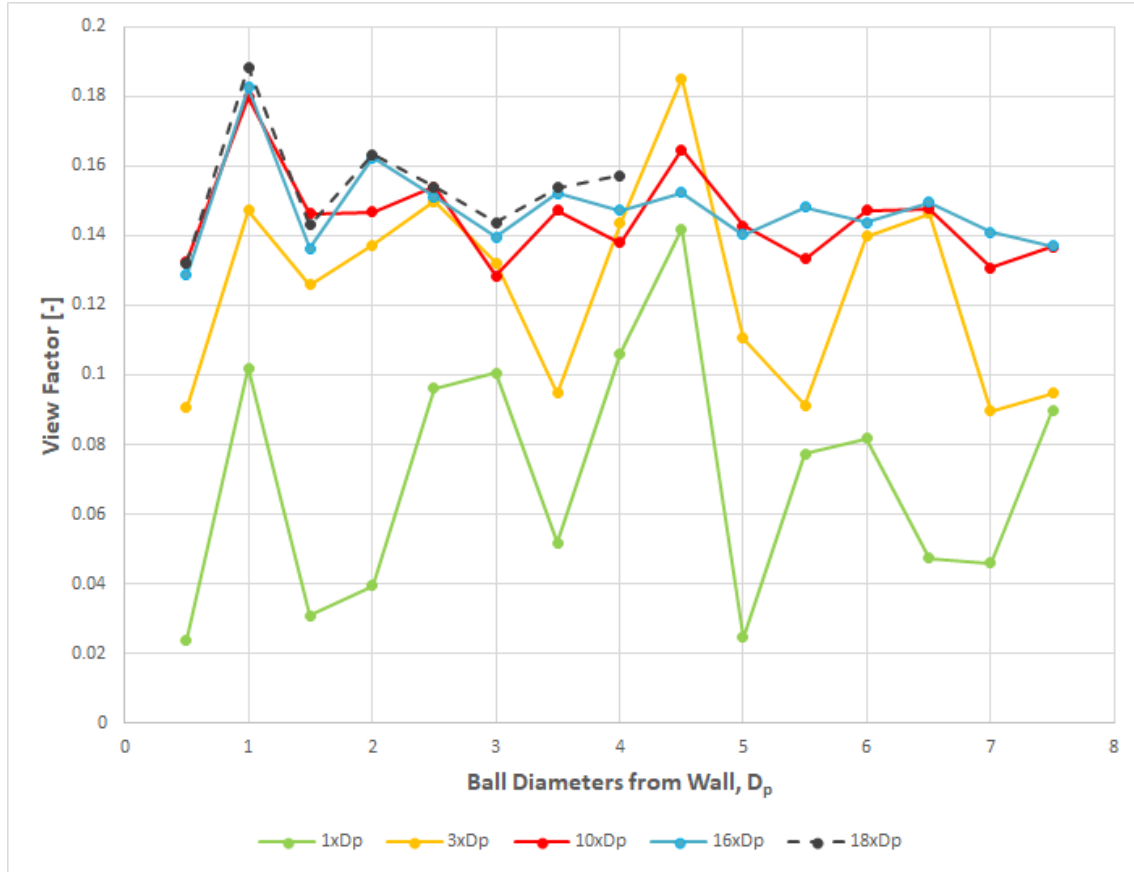


FIGURE 4.8: The view factors obtained from the section cut from the DEM packed bed using ray tracing.

The resultant function for the attenuation factor was obtained by fitting a polynomial curve through the available data points for the wall and near-wall regions. The attenuation factor in the bulk region was constant enough to be represented by a constant value of  $\kappa = 28.5$ . The function describing the attenuation factor at the wall, near-wall and bulk regions is given in 4.1. The attenuation factors for each slice is the effective local attenuation factor between the slice's front and rear surface.

$$\begin{aligned}
 \kappa(z_p) = & -0.5123x^6 + 9.1381x^5 - 64.205x^4 + 224.46x^3 - 404.16x^2 \\
 & + 345.55x - 77.132 \text{ for } z_p \leq 5D_p \\
 \kappa(z_p) = & 28.5 \text{ for } z_p > 5D_p
 \end{aligned} \tag{4.1}$$

#### 4.3.1.4 Comparison of Thermal Radiation Results in a Random Packed Bed

The evaluation of the results from the Zonal Approach was done first for the bulk region of a random packed bed and then for the wall and near-wall region. The radial thermal radiation heat transfer was evaluated similar as in the previous section, with a temperature gradient induced in the radial direction while the spheres and the side-surfaces were kept



adiabatic. The cross-sectional size of the enclosure was  $10 \times 10D_p$  and its radial thickness was  $10 \times D_p$ . The emissivities for the sphere surfaces and the enclosure surfaces were  $\epsilon = 0.8$ . The heated (front) wall temperature was varied between 1200K and 2000K for the bulk region simulations and 600K and 2000K for the wall and near-wall region simulations. The rear wall temperature was kept constant at 300K. As in the previous section only surfaces were used for the enclosure and spheres to eliminate solid conduction. The surface-to-surface radiation solver was used in the CFD software. A reasonable attempt was made at mesh independence, with the available computing resources finally dictating the mesh size.

The results from the Zonal Approach without subdivision of the control volumes or zones compares poorly to the simulation results with a difference in predicted heat of around 160% for all the temperature cases for this enclosure. The predicted heat from the Zonal Approach without subdivision was much higher than the simulated results, suggesting that the thermal resistance was too low. This can again be explained by the fact that the assumption made by using non-subdivided zones is that the surface temperature of the spheres are assumed isothermal which is not the case here.

When using the derived attenuation factor for the bulk region of  $\kappa = 28.5$ , the predicted results from the Zonal Approach with subdivision were within 20% of the results from the CFD simulation. This illustrated the importance of subdividing the zones when not working with isothermal spheres. The drawback of subdivision is the significant increase in solution time. The results for the bulk region are given in table 4.10. The radial temperature plots are given in figures 4.9 to 4.11, with a generally good agreement between the trend of the CFD simulation and the Zonal Approach.

TABLE 4.10: Results comparison between Zonal Approach with and without subdivision of its control volumes and the CFD simulation for a  $10 \times 10 \times 10D_p$  enclosure filled with the bulk region of a random packed bed.

Front Wall Temperature [K]	CFD Front Heat [W]	Zonal No Subd Front Heat [W]	Diff %	Zonal With Subd Front Heat [W]	Diff [%]
<b>1200</b>	1662.67	4201.06	158.9	1895.82	16.8
<b>1500</b>	3959.20	10280.24	159.7	4639.19	17.2
<b>2000</b>	12502.12	32526.23	160.1	14678.00	17.4

The wall region was evaluated next. A  $10 \times 10D_p$  cross-sectional enclosure with a radial thickness of  $5 \times D_p$  was filled with spheres from the wall region of the numerically packed bed mentioned in section 4.3.1.3. The radial thickness of the enclosure was  $5 \times D_p$ . The emissivity for all the enclosure and sphere surfaces were  $\epsilon = 0.8$ . The temperature of the front wall of the enclosure was varied from 1000K to 2000K while the rear temperature

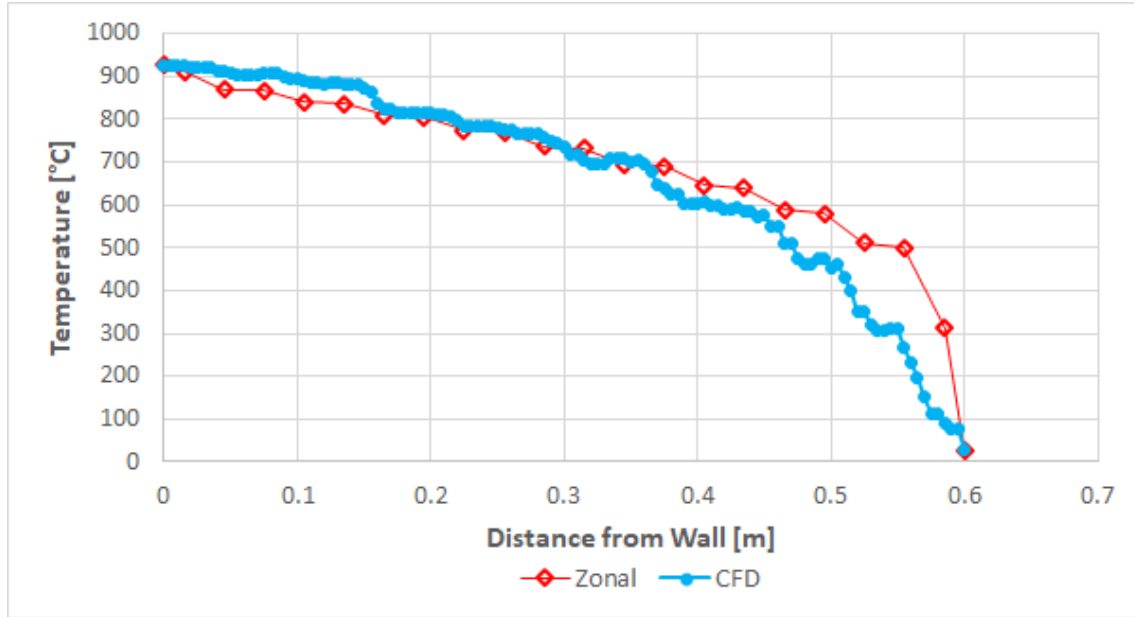


FIGURE 4.9: The radial temperature for the 1200K case for the bulk region packed into a  $10 \times 10 \times 10 D_p$  enclosure for the Zonal Approach with subdivision and the CFD simulation.

of the enclosure was kept constant. The side surfaces of the enclosure and the surfaces of the spheres were adiabatic. As in the previous section only surfaces were used for the enclosure and spheres to eliminate solid conduction. The surface-to-surface radiation solver with steady-state heat transfer was used in the CFD simulation. Only the Zonal Approach with subdivisions applied to its zones were used in the simulation of the wall and near-wall area. The results are shown in table 4.11 and the radial temperature plots are given in figures 4.12 to 4.14. The heat transferred through the bed as calculated by the Zonal Approach was higher than the CFD results by an average of 33.5%. The radial temperature curve predicted by the Zonal Approach compared well to the CFD prediction for about two thirds of the radial distance after which the CFD temperature dropped sharply into a concave curve. It is not sure if this was due to no surfaces in contact with the line probe in that location.

One of the explanations for the over-estimated heat could be due to the attenuation factor being too low close to the wall. If the porosity curve, shown in figure 4.16, containing the PBMR and HTTU porosities is compared to the attenuation factor as derived in figure 4.15, it is clear that the densest part should be  $0.5 \times D_p$  away from the wall instead of  $1 \times D_p$  away from the wall. Since the front wall is the hottest part of the enclosure and it radiates to the spheres directly adjacent to it, such a difference in porosity close to the wall will have a significant effect on the thermal resistance of the bed. It will also have the largest effect on the radial heat transferred through the bed.

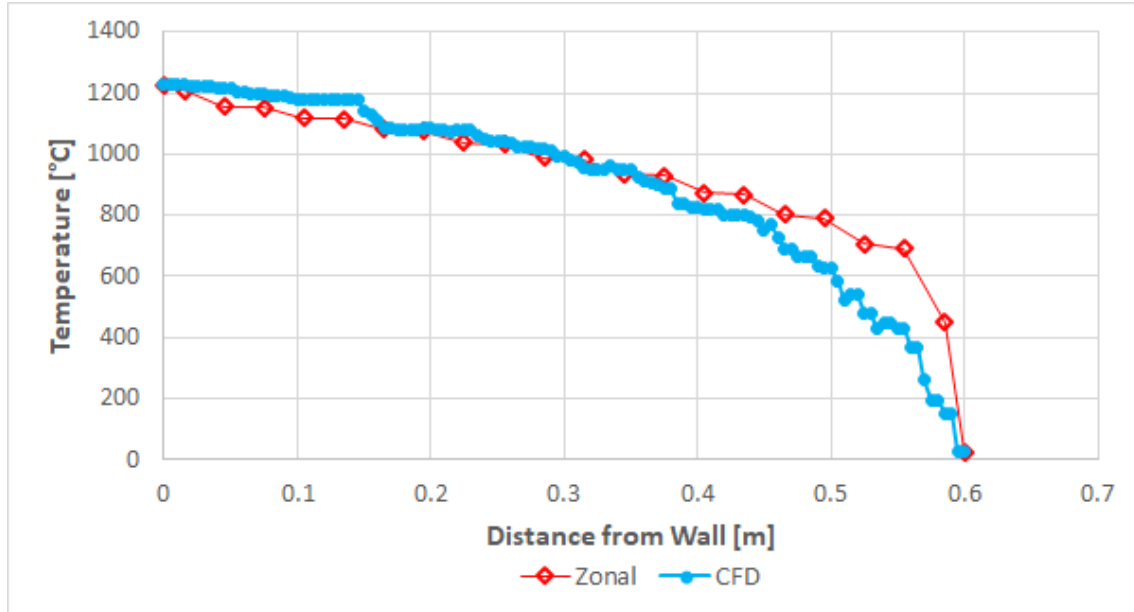


FIGURE 4.10: The radial temperature for the 1500K case for the bulk region packed into a  $10 \times 10 \times 10 D_p$  enclosure for the Zonal Approach with subdivision and the CFD simulation.

TABLE 4.11: The results comparison between the Zonal Approach with subdivision and the CFD simulation for the wall and near-wall region for various front wall temperatures.

Front Wall Temperature [K]	CFD Front Heat [W]	Zonal With Subd Front Heat [W]	Diff [%]
1000	1298.83	1723.40	32.7
1500	6567.25	8781.80	33.7
2000	20732.70	27785	34.0

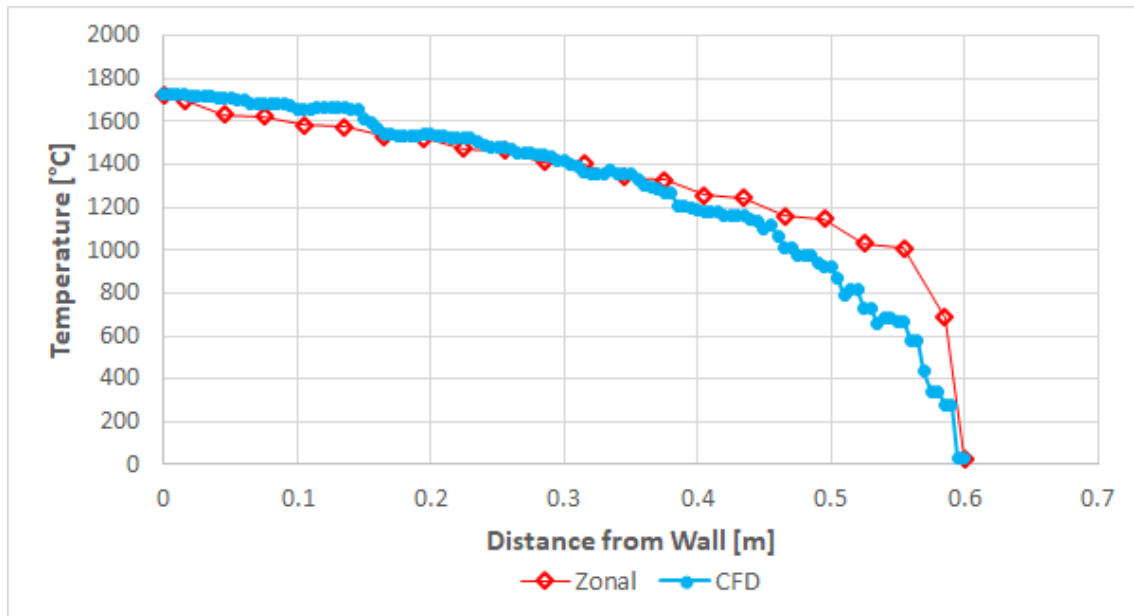


FIGURE 4.11: The radial temperature for the 2000K case for the bulk region packed into a  $10 \times 10 \times 10D_p$  enclosure for the Zonal Approach with subdivision and the CFD simulation.

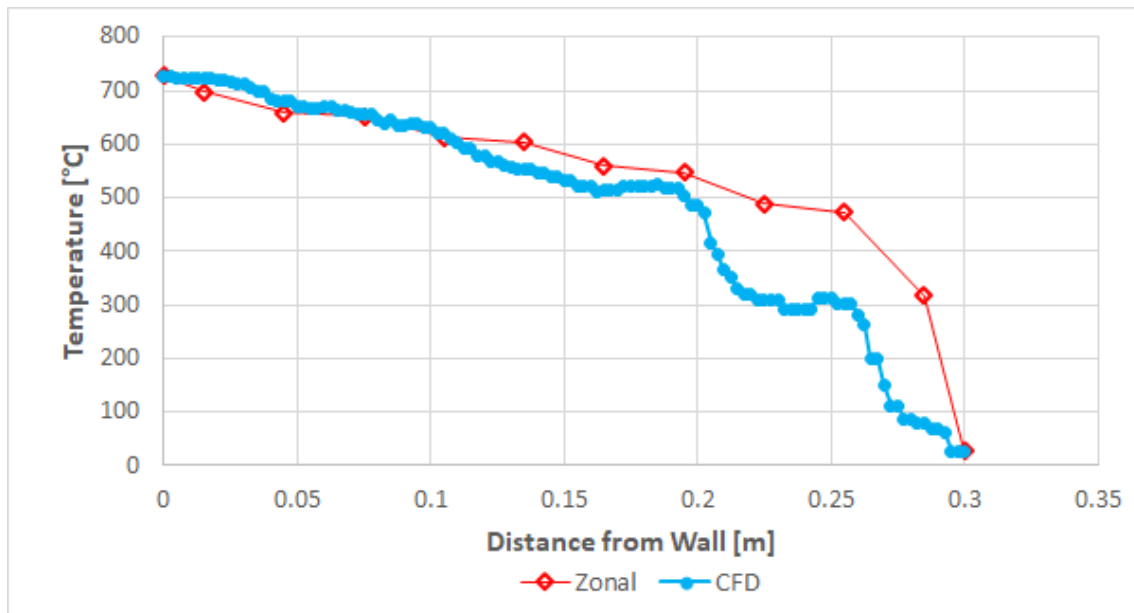


FIGURE 4.12: Comparison of the predicted temperature plots for the Zonal Approach and the CFD simulation at the wall and near-wall region for the 1000K case.

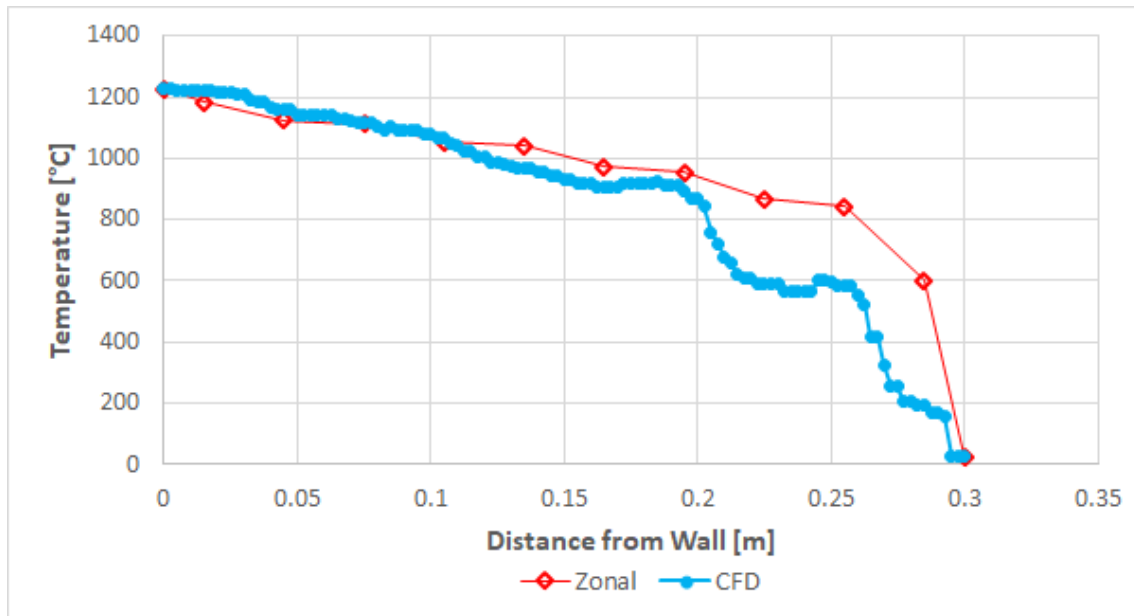


FIGURE 4.13: Comparison of the predicted temperature plots for the Zonal Approach and the CFD simulation at the wall and near-wall region for the 1000K case.

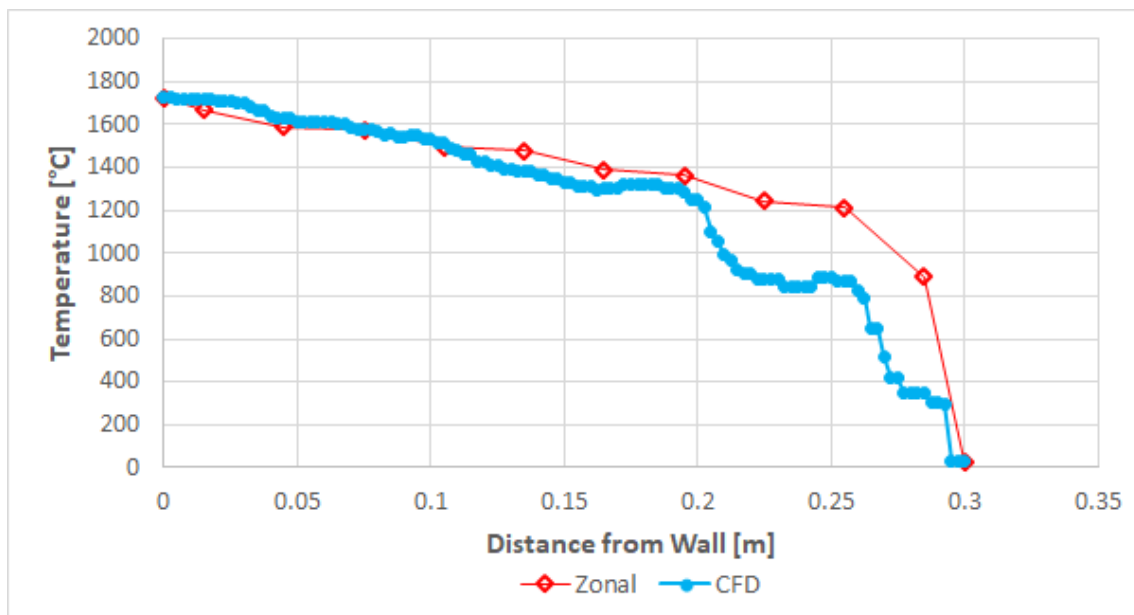


FIGURE 4.14: Comparison of the predicted temperature plots for the Zonal Approach and the CFD simulation at the wall and near-wall region for the 2000K case.

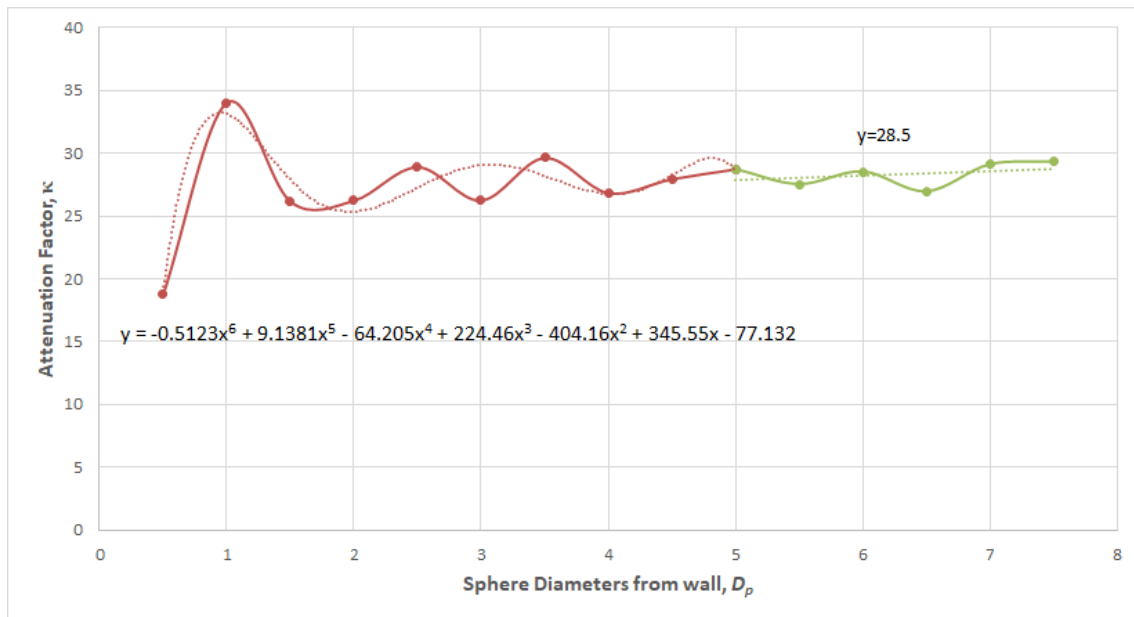


FIGURE 4.15: The derived radial attenuation factor for the wall, near-wall and bulk region.

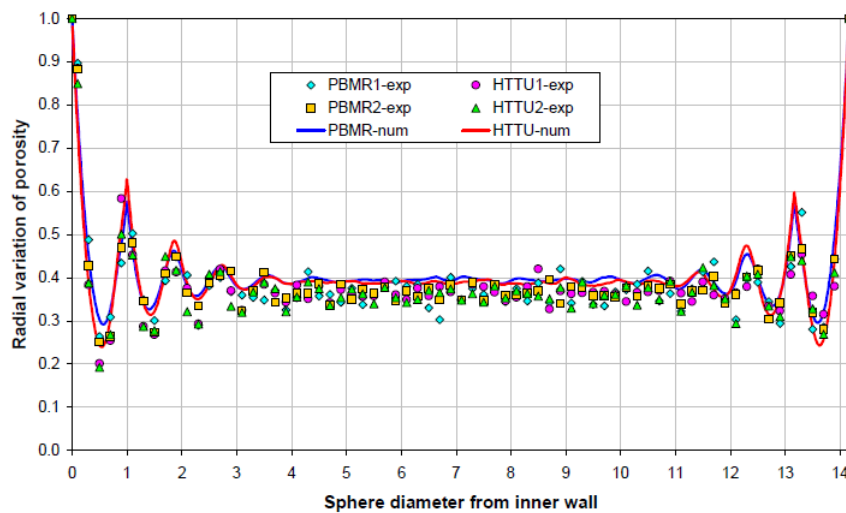


FIGURE 4.16: The radial porosity for an annular random packed bed from various experimental and numerical studies (Toit, 2008).

### 4.3.2 Comparison with the NWTCTF

The last part of this chapter is the addition of the conduction component of the MSUC to the Zonal Approach and the comparison of its results as compared to the test results of the Near-Wall Thermal Conductivity Test Facility (NWTCTF). Two different packing structures will be evaluated, namely the simple cubic structure and the random packed structure.

#### 4.3.2.1 The NWTCTF

The NWTCTF was a test facility at the North-West University in Potchefstroom's Nuclear Engineering Department. The purpose of the facility was to conduct experiments to determine the near-wall conduction and thermal radiation characteristics of a packed bed at temperatures up to 1600°C. The enclosure was cubic with inner wall dimensions of 420mm per wall. The enclosure was filled with machined graphite sphere balls with a diameter of  $D_p = 60\text{mm}$ . Figure 4.17 shows the basic layout of the facility. Several steady-state tests were conducted both with a random packing and with structured packings. The temperature of the graphite radiator was varied between 400-800°C, while the opposite wall consisted of a graphite reflector cooled by a water jacket. The side surfaces was insulated, although some heat loss did occur through the side walls. A more detailed description can be found in De Beer (2014).

#### 4.3.2.2 Comparison with the NWTCTF Simple Cubic Cases

The conduction component of the MSUC model was coupled to the Zonal Approach and solved using the Newton-Raphson iterative solver. For the simple cubic case, the coordinate number (number of spheres in contact with the viewed sphere) was set to  $N_c = 6$ . According to Siu and Lee (2000) the radial heat only has one transport path in a simple cubic structured packing, resulting in a contact angle of  $\beta = 180^\circ$ . A porosity of  $\alpha = 0.5236$  was used. The equation for the solid conductivity of graphite as used by Van Antwerpen et al. (2012) for the HTTU simulations was used, which is:

$$k_s = 147.096 - 0.229541T + 2.06027 \times 10^{-4}T^2 - 7.1529 \times 10^{-8}T^3 [\text{°C}], (\text{W/mK}) \quad (4.2)$$

The hot and cold wall temperatures for the enclosure of the Zonal approach was fixed to the measured steady state results of the NWTCTF. This was to determine the accuracy of the predicted thermal resistance through the bed. Only the Zonal Approach with the subdivided control volumes or zones were used in this section. The total heat loss through the side walls, as measured during the NWTCTF experiments, was applied to the four side walls of the Zonal Approach enclosure. In other words, the heat loss was evenly distributed

over the side walls. The results for the simulations are given in table 4.12. The predicted heat for the front wall was over-estimated in both cases, with a front wall heat of 3150.2W for the 800°C and 2169W for the 600°C case, compared to the experimental results of 2022W and 1045W for the 800°C and 600°C cases respectively. The extracted heat from the cooled wall was predicted as -2729.7W for the 800°C and -1914W for the 600°C, compared to the experimental values of 1677W for the 800°C and 829W for the 600°C case. The axial temperature distribution through the bed for the 800°C case is shown in figure 4.18 and for the 600°C case in figure 4.19. The predicted temperature curves for both cases are much lower than the experimental results, indicating a much lower thermal resistance than what was captured in the experimental results. Due to the flat shape of the temperature curve it was suspected that it might be the conduction component causing the high heat transfer. It was decided to reduce the solid conduction value to about 25% of its initial contribution to inspect the effect of the conduction component on the predicted results.

When the solid conduction was substantially reduced to less than half, the temperature curves gave a better representation of the thermal resistance through the bed and the predicted heat was closer to the measured values. The temperature curves for the 600°C and the 800°C cases are shown in figures 4.20 and 4.21.

#### 4.3.2.3 Comparison with the NWTCTF Random Packed Cases

The random packed bed experiments done in the NWTCTF were also compared to the Zonal Approach coupled with the thermal conduction component of the MSUC model from Van Antwerpen et al. (2012). The derived attenuation factor correlation for the near-wall region given in eq. [4.1] was used. The oscillatory model of De Klerk (2003) was used for the porosity calculation while the model from Reyneke and Du Toit (2010) was used to calculate the porosity in the proximity of two walls. The rest of the model was the same as for the simple cubic model.

The results are summarised in table 4.13. The predicted heat for the 800°C case was 3333W for the front wall and -2942W for the rear wall, while for the 600°C it was 2299 for the front wall and -2003W for the rear wall. The predicted heat for both cases was much lower than the experimental front wall heat of 2042W and rear wall heat of 1657W. The temperature gradient through the bed is given in figures 4.23 to 4.25. The thermal resistance for both temperature cases seems very low in this case as well, and the same adjustment to the solid conduction parameter was made. The predicted front wall heat results after the adjustment of the solid conduction was 2067W and the rear wall heat was 1670W for the 800°C case and for the 600°C case the front heat was predicted as 1127W



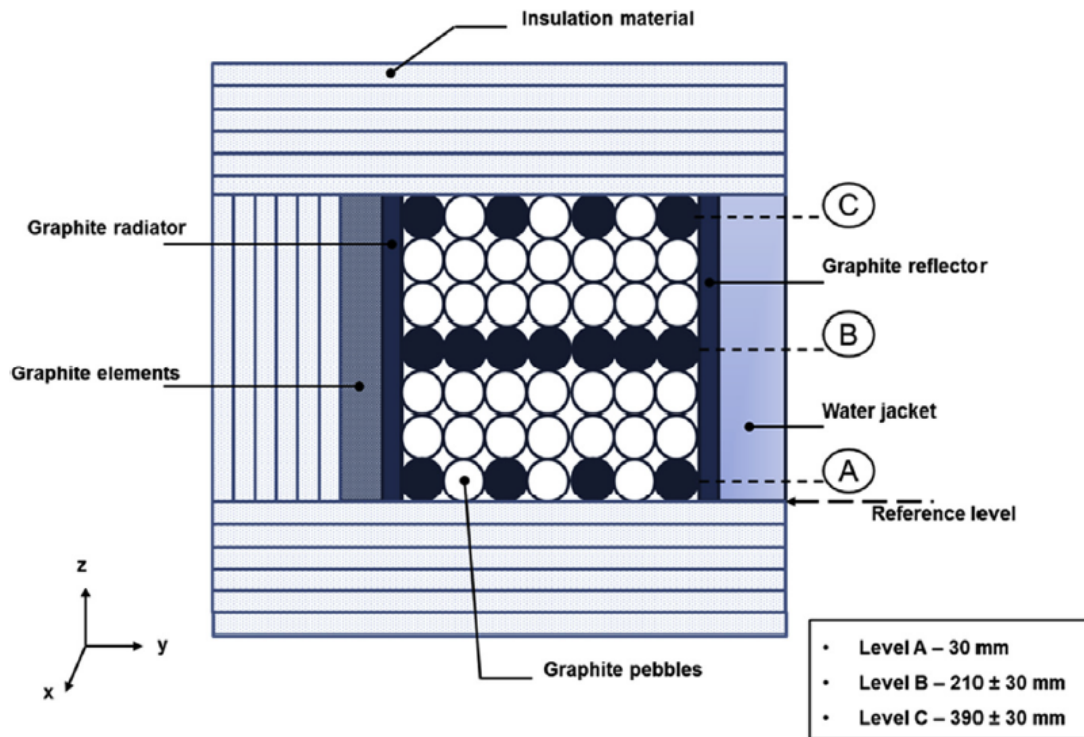


FIGURE 4.17: Basic layout of the NWTCTF (De Beer et al., 2018).

TABLE 4.12: The results predicted by the coupled Zonal-MSUC model compared with the NWTCTF experimental results for the simple cubic bed.

Simple Cubic Bed	Front Heat [W]	Rear Heat [W]	Diff. [%]
<i>800C NWTCTF</i>	2022.0	-1677.3	-
<i>800C Zonal</i>	3150.2	-2729.9	62.8
<i>800 Zonal, <math>k_c</math> adjusted</i>	2022.0	1649.4	-1.7
<i>600C NWTCTF</i>	945.0	703.8	-
<i>600C Zonal</i>	2169.2	-1914.0	172.0
<i>600C, <math>k_c</math> adjusted</i>	1098.1	-868.5	23.4

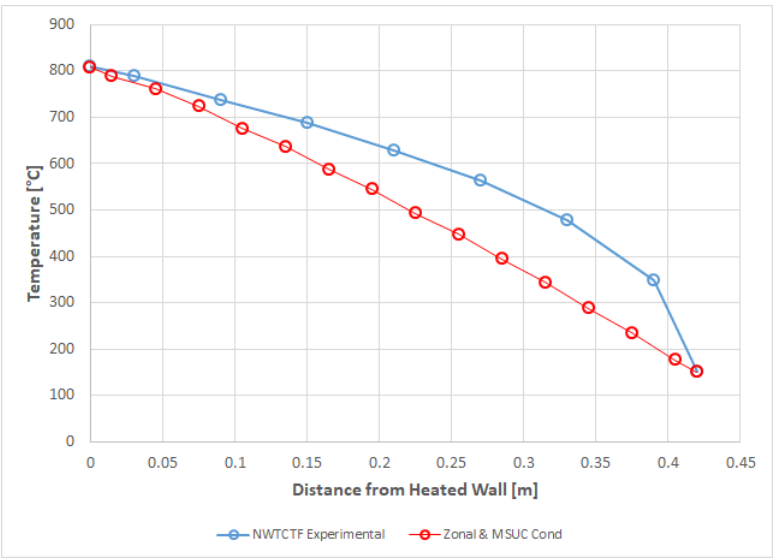


FIGURE 4.18: Comparison between Zonal Approach prediction and NWTCTF experimental results for the 800°C simple cubic bed case.

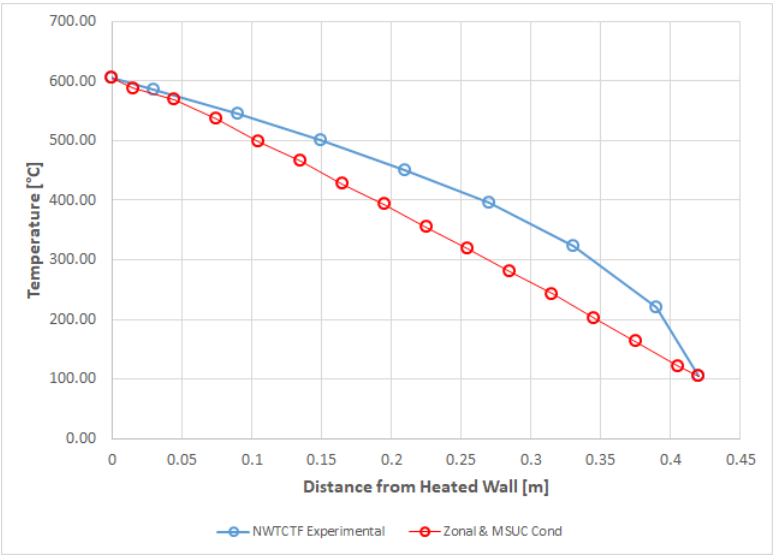


FIGURE 4.19: Comparison between Zonal Approach prediction and NWTCTF experimental results for the 600°C simple cubic bed case.

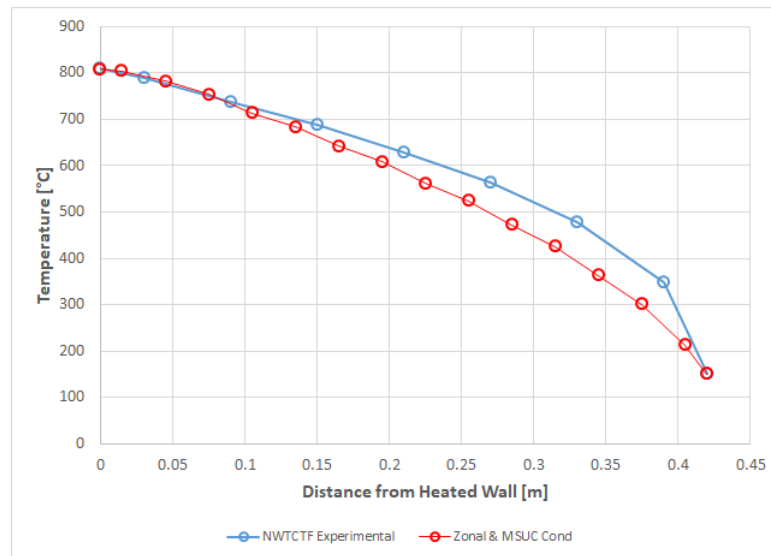


FIGURE 4.20: Comparison between Zonal Approach prediction and NWTCTF experimental results for the 800°C simple cubic bed case with reduced solid conduction.

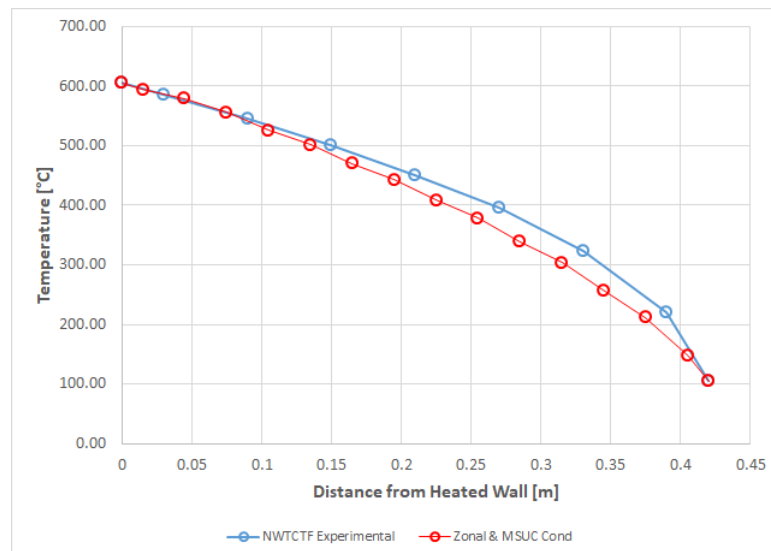


FIGURE 4.21: Comparison between Zonal Approach prediction and NWTCTF experimental results for the 600°C simple cubic bed case with reduced solid conduction.

and for the rear wall -870W. This is much closer to the experimental values. The temperature curves of the predictions with adjusted solid conductivity match the experimental temperature curves much closer. The trends near the cold wall is also very similar.

TABLE 4.13: Summarised results for the Zonal-MSUC model predicted heat of the NWTCTF random packed bed experiments.

<b>Random Packed Bed</b>	<b>Front Heat [W]</b>	<b>Rear Heat [W]</b>	<b>Diff. [%]</b>
<b><i>800C NWTCTF</i></b>	2024.9	-1567.7	-
<b><i>800C Zonal</i></b>	3332.86	-2942.48	64.6
<b><i>800 Zonal, <math>k_c</math> adjusted</i></b>	2067.3	-1670.0	2.1
<b><i>600C NWTCTF</i></b>	871.0	-643.2	-
<b><i>600C Zonal</i></b>	2299.46	-2003.49	164.0
<b><i>600C, <math>k_c</math> adjusted</i></b>	1127.0	-869.9	29.3

It is clear from the results predicted by the coupled Zonal-MSUC radiation-conduction model that the thermal resistance is too low when compared to the NWTCTF experimental results. There can be multiple possible reasons for this but to answer these questions the effects of conduction and radiation must be separated and investigated, which was already started by De Beer et al. (2017). It is also interesting to note that De Beer et al. (2017) stated that the contact resistances between the pebble-pebble and pebble-wall solid interfaces had to be refined for the NWTCTF, indicating that this could also account for the mismatch between the experimental and theoretical conduction values.

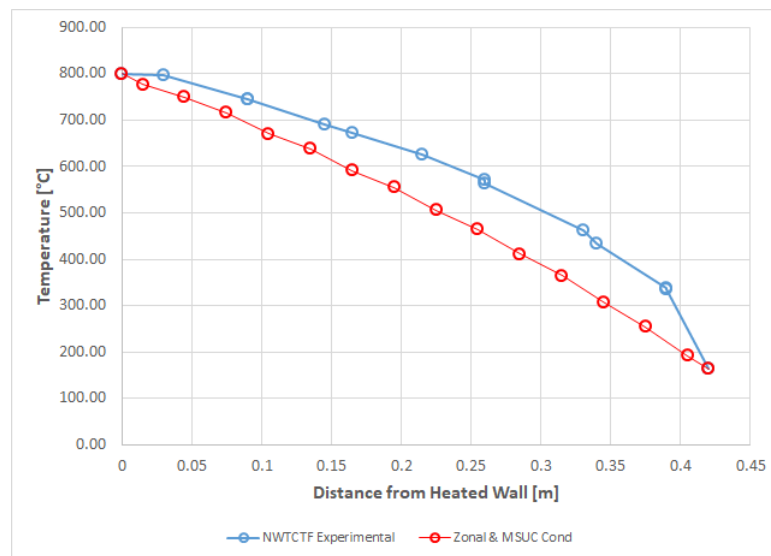


FIGURE 4.22: Comparison between Zonal Approach prediction and NWTCTF experimental results for the 800°C random-packed bed case.

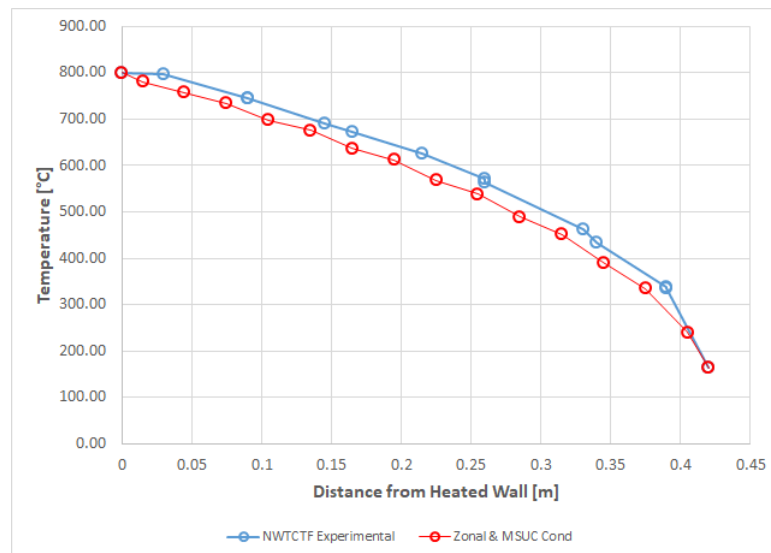


FIGURE 4.23: Comparison between Zonal Approach prediction and NWTCTF experimental results for the 800°C random-packed bed case with reduced solid conduction.

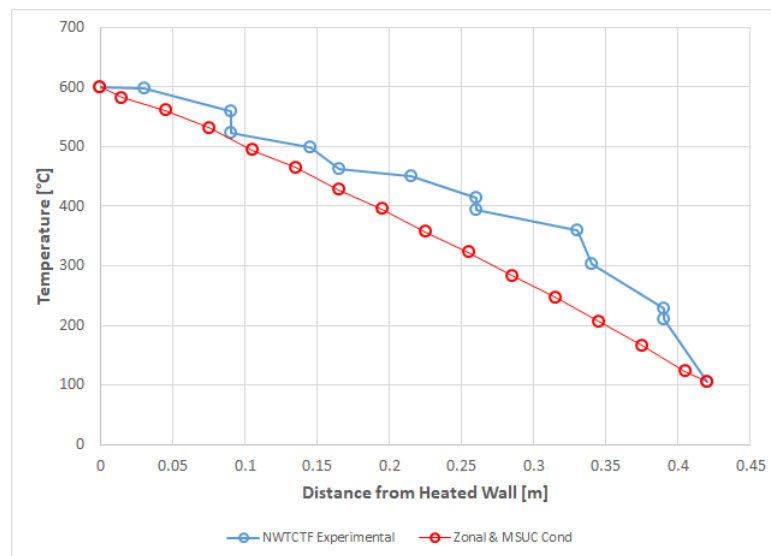


FIGURE 4.24: Comparison between Zonal Approach prediction and NWTCTF experimental results for the 600°C random-packed bed case.

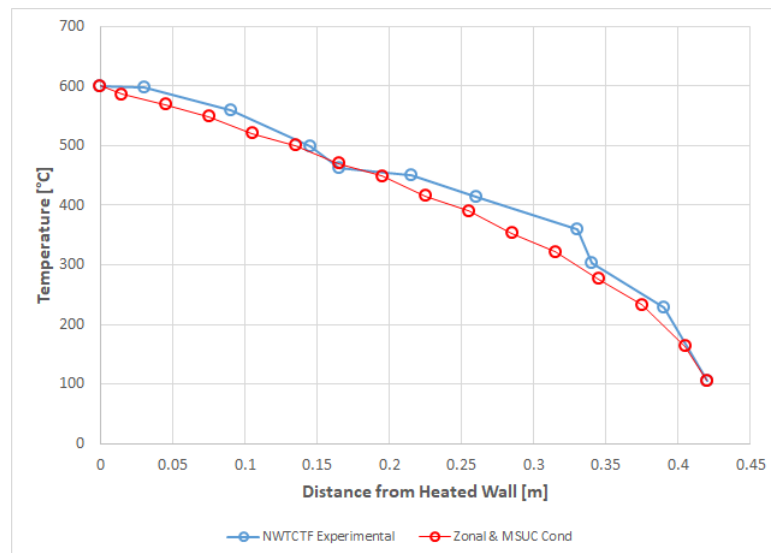


FIGURE 4.25: Comparison between Zonal Approach prediction and NWTCTF experimental results for the 600°C random-packed bed case with reduced solid conduction.

## 4.4 Summary

In this chapter the thermal radiation predictions of the Zonal Approach was compared to simulations done in a standard CFD package as well as compared to test results from the NWTCTF experimental facility. First the attenuation factors for the simple cubic and random packed beds were derived. The attenuation factors were then used to calculate the thermal radiation in various rectangular enclosures and the results were compared to the CFD simulation results. The control volumes of the Zonal Approach were subdivided to accommodate the non-isothermal temperatures on the sphere surfaces and the results generated with the subdivided control volumes compared favourably with the CFD predictions. It was noted that the spheres in a pebble bed reactor would generate heat which would generally cause a more even temperature distribution on the said sphere surface than an inert sphere, but it was also noted that this might not always be the case. Due to this the model needed to be fundamentally correct and that the ability to take non-isothermal surface temperatures into account was important while it would also enhance the model's abilities and its potential applications. The Zonal Approach was then coupled to the conduction component of the MSUC model and was used to predict the results from the experiments of the NWTCTF for both a simple cubic bed and a random packed bed. The thermal resistance predicted by the coupled Zonal-MSUC radiation-conduction model was much lower than the experimental values requiring an adjustment to the solid conduction parameter to match the experimental results from the NWTCTF. It was suggested that the uncertainty surrounding the contact resistance of the solid-solid interfaces for the NWTCTF could explain the difference.

## 5 Conclusions and Recommendations

### 5.1 Summary

The Zonal Approach was applied to a packed bed with mono-sized spheres to model the thermal radiation model. An improved thermal radiation component was needed to replace the current thermal radiation component in the MSUC model, whose long-range thermal radiation component wasn't well defined. The simplicity and long-range exchange capability of a network-type model was required, and the Zonal Approach was suggested. A shortcoming of the Zonal Approach was its difficulty in handling complicated geometry. It was decided to use ray-tracing to characterise the exchange in a packed bed and apply the derived attenuation factors to calculate the direct exchange areas with the Zonal Approach. The emission from a volume zone as well as the direct exchange area correlations for volume-to-surface exchange and for volume-to-volume exchange had to be re-derived for the Zonal Approach. The Zonal Approach was also coupled with the conduction component of the MSUC model.

The radial (front to rear) attenuation factors for a structured simple cubic and a random-packed bed was derived using ray-tracing. The wall-, near-wall- and bulk regions was included for the random packed bed. Due to the structured nature of the simple cubic bed, the front spheres tend to obscure the rear spheres from thermal radiation exchange from directly in front, causing the radial attenuation factor to differ for enclosures with different radial thicknesses and generally under-predicting the attenuation factor for radially thicker enclosures. The predicted radial heat transfer through the bed for the Zonal Approach using the derived attenuation factors differed from 20% for the  $1 \times D_p$  radial thickness enclosures to 260% for the  $10 \times D_p$  radial thickness enclosures. The extremely large difference for the thicker enclosures was due to the lower predicted attenuation factor. When evaluating what attenuation factors was required to fit the CFD simulation results to within 1%, it only differed slightly for the different radial thicknesses, from an average of  $\kappa = 37$  (if excluding the  $1 \times 1 \times 1 D_p$  enclosure) for the  $1 \times D_p$  radial thickness enclosures to  $\kappa = 34$  for the radially thicker enclosures for temperatures between 600K and 2000K.

The attenuation factor in the radial direction as derived from a numerically packed bed for the wall-, near-wall- and bulk regions was done by assessing the view factors between the



front and rear surfaces of slices cut from the bed. The slices were  $0.5 \times D_p$  thick and it was found that a cross-sectional size of  $16 \times 16 D_p$  was sufficient as to be independent of the calculated view factors. When the derived attenuation factors were compared to a radial porosity plot of a packed pebble bed from literature, it was found that the peak attenuation factor (which is a function of the porosity) did not occur at  $0.5 \times D_p$  as suggested by the porosity plot from literature, but occurred at  $1 \times D_p$  from the wall. This difference could cause the thermal resistance closest to the hot wall to be predicted to low, which will result in a higher predicted heat. When the results for the near-wall region from the Zonal Approach were compared to the results from the CFD simulations, it was found that the heat was over-predicted by an average of 33% for the different temperature cases.

The predicted thermal radiation from the Zonal Approach for the bulk region was within 20% of the CFD simulations, with the radial temperature in good agreement with the CFD predictions.

It was clear that a control volume or zone size of  $1 \times 1 \times 1 D_p$  couldn't be used for generalised models. The reason was the assumption that the emitting surface of a sphere, which fitted inside such a control volume, was isothermal and would emit in all  $4\pi$  directions, which was not the case. This was demonstrated by a single control volume with a hot front surface and a cold rear surface, where the hot front surface emitted to the front of the sphere while the rear part of the sphere remained relatively cool. Using non-subdivided control volumes will cause an under-prediction in the thermal resistance which was visible in its results. The only suitable case where a non-subdivided control volume could be used is if the surface temperatures could be assumed to be close to isothermal. It was noted that in practice the spheres from a pebble bed reactor would generate internal heat which could result in a more even sphere surface temperature, but this could not account for all the cases and it was also decided that the model implementation could not be restricted to this condition. It was important to be able to model the thermal radiation fundamentally correct more than one possible cases.

The conduction component was coupled to the Zonal Approach and solved using a Newton-Raphson iterative solver. A simple cubic bed and a random-packed bed was compared to the NWTCTF experimental results. The predicted heat from the Zonal Approach compared generally well to the experimental data, but the temperature curve in the radial direction showed that the thermal resistance in the bed was too low. Since the thermal radiation only model was in good agreement with a known CFD package, it was thought that the conduction model possibly didn't capture the NWTCTF effects very well (its size is much smaller than the HTTU test unit) or there may be other unknown reasons why the experimental setup has a much lower thermal resistance. It was noted that there is on-going research investigating the solid-solid contact resistance between pebble-pebble and

pebble-wall interfaces by De Beer et al. (2017) which could account for the disagreement in conduction predictions.

## 5.2 Conclusions

It can be concluded that the outcomes as defined in section 1.6 were met. The Zonal Approach was adapted to accommodate thermal radiation inside a packed pebble bed filled with mono-sized spheres. The direct-exchange areas were adapted for both a structured and a random-packed bed. The attenuation factor for both these packing structures were derived and tested against an industry-standard CFD code. The study also investigated the practicality of adapting the Zonal Approach for modeling the thermal radiation inside a packed bed by coupling the Zonal Approach to the conduction component of the MSUC model. The results from the coupled model was compared to the experimental results from the NWTCTF. The control volume (zone) sizing was also discussed.

The Zonal Approach showed promise in predicting thermal radiation without solid conduction present, taking into account non-isothermal surface temperatures on the spheres. The results showed that the derivation of the attenuation factors for both the simple cubic and random packed beds still needed some refining but the results were encouraging. The relatively fast solution times even for the Zonal Approach with subdivided control volumes was also encouraging. In general the Zonal Approach showed promise in the calculation of radiative heat transfer in a packed pebble bed filled with mono-sized spheres.

## 5.3 Recommendations for Further Research

- The derivation of the attenuation factors of a packed pebble bed can be further investigated, especially the contributions of the axial components.
- The wall- and near-wall regions can be better refined to improve the accuracy of the predicted radial temperature gradient.
- The Direct-exchange areas for surface-to-volume zones for short distances of less than  $1 \times D_p$  can be further improved.
- The Zonal Approach can be adapted for cylindrical coordinates to calculate the thermal radiation inside cylindrical and annular enclosures.
- The difference in thermal resistance between the results of the Zonal Approach and the NWTCTF experimental results can be investigated and the coupled thermal radiation and conduction model refined. This might require investigating the conduction and radiation contributions separately.

- 
- The Zonal Approach could be expanded to incorporate cylindrical coordinates.
  - The influence of more subdivisions on the predicted radial temperature distribution can also be investigated to ascertain the limit of accuracy for the Zonal Approach.
  - The Zonal Approach can be adapted to solve transient systems, and its ability to model fast transient changes can be investigated.

# Bibliography

- Altaç, Zekeriya and Mesut Tekkalmaz (2011). “Exact Solution of Radiative Transfer Equation for Three-Dimensional Rectangular, Linearly Scattering Medium”. In: *Journal of Thermophysics and Heat Transfer* 25.2, pp. 228–238.
- Asakuma, Yusuke, Yushin Kanazawa, and Tsuyoshi Yamamoto (2014). “Thermal radiation analysis of packed bed by a homogenization method”. In: *International Journal of Heat and Mass Transfer* 73, pp. 97–102.
- Bordbar, Mohammad Hadi and Timo Hyppänen (2007). “Modeling of Radiation Heat Transfer in a Boiler Furnace”. In: *Advanced Studies in Theoretical Physics* 1.12, pp. 571–584.
- Campbell, J.P. and Dudley G. McConnell (1968). *Radiant-Interchange Configuration Factors for Spherical and Conical Surfaces to Spheres, TN D-4457*. Tech. rep. Washington, DC: NASA, p. 26.
- CD-Adapco (2014). *User Guide: STAR-CCM+ Version 9.02*. New York: CD-Adapco.
- Cheng, G Jj and A B Yu (2013). “Particle Scale Evaluation of the Effective Thermal Conductivity from the Structure of a Packed Bed: Radiation Heat Transfer”. In: *Ind. Eng. Chem. Res.* 52, pp. 12202–12211.
- De Beer, M (2014). “Characterisation of thermal radiation in the near - wall region of a packed pebble bed”. Master’s Thesis, p. 197.
- De Beer, M., C. G. Du Toit, and P. G. Rousseau (2017). “A methodology to investigate the contribution of conduction and radiation heat transfer to the effective thermal conductivity of packed graphite pebble beds, including the wall effect”. In: *Nuclear Engineering and Design* 314, pp. 67–81.
- (2018). “Experimental study of the effective thermal conductivity in the near-wall region of a packed pebble bed”. In: *Nuclear Engineering and Design* 339. September, pp. 253–268.

- De Klerk, Arno (2003). "Voidage variation in packed beds at small column to particle diameter ratio". In: *AIChE Journal* 49.8, pp. 2022–2029.
- Dong, Yujie (2018). "Design, Safety Features and Progress of HTR-PM". In: *GEN IV Int. Forum*, pp. 1–42.
- Feingold, A and K G Gupta (1970). "New Analytical Approach to the Evaluation of Configuration Factors in Radiation From Spheres and Infinitely Long Cylinders". In: *Journal of Heat Transfer* 92.1, pp. 69–76.
- Fluent, Inc. (2001). "FLUENT 6.0 User's Guide Volume 2". In: *FLUENT 6.0 User's Guide*. Volume 2. Lebanon: Fluent Inc. Chap. Chapter 11, pp. 11–1 –11–104.
- Fundamenski, WR and PJ Gierszewski (1991). *COMPARISON OF CORRELATIONS FOR HEAT TRANSFER IN SPHERE- PAC BEDS CFFTPG-9181 COMPARISON OF CORRELATIONS FOR HEAT TRANSFER IN SPHERE- PAC BEDS*. Tech. rep. August. Mississauga: Canadian Fusion Fuels Technology Project, p. 43.
- Hamilton, D.C. and W.R. Morgan (1952). *Radiant Interchange Configuration Factors TN 2836*. Tech. rep. NASA, p. 111.
- Hottel, H C and E S Cohen (1958). "Radiant heat exchange in a gas-filled enclosure: Allowance for nonuniformity of gas temperature". In: *AIChE Journal* 4.1, pp. 3–14.
- Howell, John R. and M. Pinar Mengüç (2011). "Radiative transfer configuration factor catalog: A listing of relations for common geometries". In: *Journal of Quantitative Spectroscopy and Radiative Transfer* 112.5, pp. 910–912.
- Howell, John R. and Robert Siegel (1992). *Thermal Radiation Heat Transfer*. Ed. by Mary Prescott and Carolyn V Ormes. Third Edit. Washington, DC: Hemisphere Publishing Corporation, p. 1072.
- Incropera, Frank P. et al. (2007). *Fundamentals of Heat and Mass Transfer*. 6th. Hoboken: John Wiley & Sons, p. 1070.
- Juul, Niels H (1976). "Diffuse radiation configuration view factors between two spheres, and their limits". In: *Letters in Heat and Mass Transfer* 3.3, pp. 205–211.
- Kim, Man Young (2008). "Assessment of the axisymmetric radiative heat transfer in a cylindrical enclosure with the finite volume method". In: *International Journal of Heat and Mass Transfer* 51.21-22, pp. 5144–5153.

- Kovtanyuk, Andrey E, Nikolai D Botkin, and Karl-Heinz Hoffmann (2012). “Numerical simulations of a coupled radiative-conductive heat transfer model using a modified Monte Carlo method”. In: *International Journal of Heat and Mass Transfer* 55.4, pp. 649–654.
- Larsen, M. E. and John R. Howell (1986). “Least squares smoothing of direct exchange areas in zonal analysis”. In: *American Society of Mechanical Engineers. Journal of Heat Transfer* 108.1, pp. 239–242.
- Liemert, André and Alwin Kienle (2011). “Analytical solution of the radiative transfer equation for infinite-space fluence”. In: *Physical Review A - Atomic, Molecular, and Optical Physics* 83.1, pp. 1–4.
- Modest, Michael F (2003). *Radiative Heat Transfer*. Second Edi. San Diego: Elsevier Science (USA), p. 845.
- Pitso, LM (2011). “Characterisation of long range radiation heat transfer in packed pebble beds”. Masters Dissertation. North-West University, p. 54.
- Reyneke, H. J. and C. G. Du Toit (2010). “Modelling the superficial velocity distribution inside an annular packed bed”. In: *7th South African Conference on Computational and Applied Mechanics, SACAM 2010* January, pp. 185–194.
- Rousseau, Pieter G., C. G. du Toit, and M.L. Pitso (2012). “The SUN Model for Radiation Heat Transfer in Packed Pebble Bed Gas Cooled Reactors”. In: *Proceedings of the HTR 2012*. Tokyo.
- Rousseau, Pieter G., Charl G. Toit, and Stefan van der Walt (2014). “Implementation of the Sun Model for Radiation Heat Transfer in Packed Pebble Bed Gas Cooled Reactors”. In: *The 15th International Heat Transfer Conference* 1, pp. 1–15.
- Ruan, L. M. et al. (2006). “Development of a finite element model for coupled radiative and conductive heat transfer in participating media”. In: *Journal of Quantitative Spectroscopy and Radiative Transfer* 102.2, pp. 190–202.
- Siu, W. W.M. and S. K. Lee (2000). “Effective conductivity computation of a packed bed using constriction resistance and contact angle effects”. In: *International Journal of Heat and Mass Transfer* 43.21, pp. 3917–3924.
- Toit, C. G. du (2008). “Radial variation in porosity in annular packed beds”. In: *Nuclear Engineering and Design* 238.11, pp. 3073–3079.

- Van Antwerpen, W., P. G. Rousseau, and C. G. Du Toit (2012). “Multi-sphere Unit Cell model to calculate the effective thermal conductivity in packed pebble beds of mono-sized spheres”. In: *Nuclear Engineering and Design* 247, pp. 183–201.
- Van Antwerpen, Werner (2009). “Modelling the effective thermal conductivity in the near-wall region of a packed pebble bed”. Phd Thesis. North-West University, p. 244.
- Van Antwerpen, Werner, C. G. Du Toit, and Pieter G. Rousseau (2010). “A review of correlations to model the packing structure and effective thermal conductivity in packed beds of mono-sized spherical particles”. In: *Nuclear Engineering and Design* 240.7, pp. 1803–1818.
- Van der Meer, Willem (2011). “Modelling long-range radiation heat transfer in a pebble bed reactor”. Masters Dissertation. North-West University, p. 97.
- Viskanta, R and M P Menguc (1987). “Radiation heat transfer in combustion systems”. In: *Progress in Energy and Combustion Science* 13.2, pp. 97–160.
- Wu, Hao et al. (2016). “Effect of scale on the modeling of radiation heat transfer in packed pebble beds”. In: *International Journal of Heat and Mass Transfer* 101, pp. 562–569.
- (2017). “Numerical simulation of heat transfer in packed pebble beds: CFD-DEM coupled with particle thermal radiation”. In: *International Journal of Heat and Mass Transfer* 110, pp. 393–405.

# A Appendix A: Matlab Model for Radiation-Conduction Model

```

close all
clearvars %global
format shortG
clc

%-----
%-----

%Precalculations for Area A1, Area A2 and Volume V1

slice_size = 7;
slice_number = 7;
zone_area_dimension = 0.5;
zone_volume_dimension = 0.5;
number_iterations = 5;

userview = memory
c = clock

porosity_NWETCTF = csvread('NWETCTF_xy_porosity_subd.csv');
porosity_deklerk = csvread('de_klerk_porosity_subd.csv');
porosity_distance_NW = porosity_NWETCTF(:,1)';
porosity_distance_DK = porosity_deklerk(:,1)';
porosity_x_NW = porosity_NWETCTF(:,2)';
porosity_x_DK = porosity_deklerk(:,2)';
porosity_y_NW = porosity_NWETCTF(:,3)';
porosity_y_DK = porosity_deklerk(:,2)';

%For Area A1 and Area A2
D_pebble = 0.06; %Diameter of pebble in meter
r_pebble = D_pebble/2;
A_pebble = 4*pi*(0.5*D_pebble)^2; %Surface Area of pebble
A_p_section = 0.125*A_pebble; %Surface area of a 1/8th section of a pebble
A1_side_length = slice_size*D_pebble;
A1_number_subd = A1_side_length / (zone_area_dimension*D_pebble);
A1_number_zones = (A1_number_subd)^2;
A1_step = A1_side_length / A1_number_subd;

%-----
%-----

%Added for New Model
porosity = 0.39;
V_cv = A1_step ^ 3;
factor_ss = pi / (6*(1-porosity));
A_pebble = 4*pi*(D_pebble/2)^2;
A_circle = pi*(D_pebble/2)^2;
A_random = 6*(1-porosity) * V_cv / D_pebble; %Random
%-----
%-----

A2_number_subd = A1_number_subd;
A2_side_length = A1_side_length;
A2_number_zones = A1_number_zones;
A2_step = A1_step;

Volume_thickness = slice_number *D_pebble ; %Thickness of the volume of the participating
medium along the x-axis or distance two plates will be from each other, this is in accordance with the set-up of
the CFD simulations

```



```

A3_number_subd = Volume_thickness / (zone_area_dimension*D_pebble);
A3_side_length = A1_side_length;
A3_number_zones = A3_number_subd*A1_number_subd;           %The number of zones is the number of "slices" times the
    number of subdivisions along its length (i.e. 2 subdivisions along its thickness x 32 subdivisions along its 16
    Dp length)
A3_step = A1_step;

%For the volume zones
kappa = 28.5;                                               %Attenuation factor for bulk-region is
    constant, we take the average value for bulk region from CFD simulations from slice 11 to 15

V1_side_length = A1_side_length;
V1_number_subd = V1_side_length / (zone_volume_dimension*D_pebble);
V1_step = V1_side_length/V1_number_subd;
V1_x_number_subd = Volume_thickness / V1_step;
V1_number_zones = V1_number_subd^2 * V1_x_number_subd;      %The total number of zones for the volume
    is the number of zones on the surface area on top of the volume x Number of zones along the thickness of the
    volume
V1_y_number_subd = V1_number_subd;
V1_z_number_subd = V1_number_subd;

%-----

%Area Zones coordinate calculation

%Area A1 – The void-in area of slice
A1_zone_coordinates = zeros(A1_number_zones,4);
A1_zone_normal_vector = zeros(A1_number_zones,4);

counter = 0;                                                %matrix counter

for k = 0:(A1_number_subd-1);
    for j = 0:(A1_number_subd-1);                            %Area 1 starts at
        origin and the x-coordinate stays at 0 for all Areal_zone coordinates
        counter = counter + 1;
        A1_zone_coory = j*A1_step + A1_step/2;              %Coordinates of center of each CV, with the
            bottom corner of the first CV starting at 0,0,0
        A1_zone_coorz = k*A1_step + A1_step/2;
        A1_zone_coordinates(counter,:) = [counter 0 A1_zone_coory A1_zone_coorz];
        A1_zone_normal_vector(counter,:) = [counter 1 0 0];
    end
end

%Area A2 – The Void-out Area of the slice
A2_zone_coordinates = zeros(A2_number_zones,4);
A2_zone_normal_vector = zeros(A2_number_zones,4);

counter = 0;                                                %matrix counter

for k = 0:(A2_number_subd-1);
    for j = 0:(A2_number_subd-1);                            %Area 1 starts at origin and the x-
        coordinate stays at 0 for all Areal_zone coordinates
        counter = counter + 1;
        A2_zone_coory = j*A2_step + A2_step/2;              %Coordinates of center of each CV, with the
            bottom corner of the first CV starting at 0,0,0
        A2_zone_coorz = k*A2_step + A2_step/2;
        A2_zone_coordinates(counter,:) = [counter Volume_thickness A2_zone_coory A2_zone_coorz];
        A2_zone_normal_vector(counter,:) = [counter -1 0 0];
    end
end

%Area A3 – The Left-hand side of the enclosure, i.e. part of the
%"environment" as used in the star-ccm+ simulation
A3_zone_coordinates = zeros(A3_number_zones,4);
A3_zone_normal_vector = zeros(A3_number_zones,4);

counter = 0;                                                %matrix counter

for i = 0:(A3_number_subd-1);                                %Area 1 starts at origin and the x-coordinate
    stays at 0 for all Areal_zone coordinates
    for j = 0:(A1_number_subd-1);
        counter = counter + 1;
        A3_zone_coorex = i*A3_step + A3_step/2;
        A3_zone_coory = j*A3_step + A3_step/2;              %Coordinates of center of each CV, with the
            bottom corner of the first CV starting at 0,0,0
        A3_zone_coordinates(counter,:) = [counter A3_zone_coorex A3_zone_coory 0];
    end
end

```

```

        A3_zone_normal_vector(counter,:) = [counter 0 0 1];
    end
end

%Area A4 – The bottom side of the enclosure, i.e. part of the
%"environment" as used in the star-ccm+ simulation
A4_zone_coordinates = zeros(A3_number_zones,4);
A4_zone_normal_vector = zeros(A3_number_zones,4);

counter = 0; %matrix counter

for i = 0:(A3_number_subd-1); %Area 1 starts at origin and the x-coordinate
    stays at 0 for all Areal_zone coordinates
    for k = 0:(A1_number_subd-1);
        counter = counter + 1;
        A4_zone_coorx = i*A3_step + A3_step/2; %Coordinates of center of each
        CV, with the bottom corner of the first CV starting at 0,0,0
        A4_zone_coorz = k*A3_step + A3_step/2;
        A4_zone_coordinates(counter,:) = [counter A4_zone_coorx 0 A4_zone_coorz];
        A4_zone_normal_vector(counter,:) = [counter 0 1 0];
    end
end

%Area A5 – The Right-hand side of the enclosure, i.e. part of the
%"environment" as used in the star-ccm+ simulation
A5_zone_coordinates = zeros(A3_number_zones,4);
A5_zone_normal_vector = zeros(A3_number_zones,4);

counter = 0; %matrix counter

for i = 0:(A3_number_subd-1); %Area 1 starts at origin and the x-coordinate
    stays at 0 for all Areal_zone coordinates
    for j = 0:(A1_number_subd-1);
        counter = counter + 1;
        A5_zone_coorx = i*A3_step + A3_step/2;
        A5_zone_coory = j*A3_step + A3_step/2; %Coordinates of center of each CV, with the
        bottom corner of the first CV starting at 0,0,0
        A5_zone_coordinates(counter,:) = [counter A5_zone_coorx A5_zone_coory A1_side_length];
        A5_zone_normal_vector(counter,:) = [counter 0 0 -1];
    end
end

%Area A6 – The Top side of the enclosure, i.e. part of the
%"environment" as used in the star-ccm+ simulation
A6_zone_coordinates = zeros(A3_number_zones,4);
A6_zone_normal_vector = zeros(A3_number_zones,4);

counter = 0; %matrix counter

for i = 0:(A3_number_subd-1); %Area 1 starts at origin and the x-coordinate
    stays at 0 for all Areal_zone coordinates
    for k = 0:(A1_number_subd-1);
        counter = counter + 1;
        A6_zone_coorx = i*A3_step + A3_step/2; %Coordinates of center of each CV, with the
        bottom corner of the first CV starting at 0,0,0
        A6_zone_coorz = k*A3_step + A3_step/2;
        A6_zone_coordinates(counter,:) = [counter A6_zone_coorx A1_side_length A6_zone_coorz];
        A6_zone_normal_vector(counter,:) = [counter 0 -1 0];
    end
end

%Creating a complete matrix of the coordinates of the surface zones
A_zone_coordinates(1:A1_number_zones,:) =
    A1_zone_coordinates;
A_zone_coordinates((A1_number_zones+1):2*A1_number_zones,:) =
    A2_zone_coordinates;
A_zone_coordinates((2*A1_number_zones+1):(2*A1_number_zones+A3_number_zones),:) =
    A3_zone_coordinates;
A_zone_coordinates(((2*A1_number_zones+A3_number_zones)+1):(2*A1_number_zones+2*A3_number_zones),:) =
    A4_zone_coordinates;
A_zone_coordinates(((2*A1_number_zones+2*A3_number_zones)+1):(2*A1_number_zones+3*A3_number_zones),:) =
    A5_zone_coordinates;
A_zone_coordinates(((2*A1_number_zones+3*A3_number_zones)+1):(2*A1_number_zones+4*A3_number_zones),:) =
    A6_zone_coordinates;

```

```

%Creating a complete matrix of the coordinates of each point's normal
%vector
A_zone_normal_vector(1:A1_number_zones,:) =
    A1_zone_normal_vector;
A_zone_normal_vector((A1_number_zones+1):2*A1_number_zones,:) =
    A2_zone_normal_vector;
A_zone_normal_vector((2*A1_number_zones+1):(2*A1_number_zones+A3_number_zones)) =
    A3_zone_normal_vector;
A_zone_normal_vector(((2*A1_number_zones+A3_number_zones)+1):(2*A1_number_zones+2*A3_number_zones)) =
    A4_zone_normal_vector;
A_zone_normal_vector(((2*A1_number_zones+2*A3_number_zones)+1):(2*A1_number_zones+3*A3_number_zones)) =
    A5_zone_normal_vector;
A_zone_normal_vector(((2*A1_number_zones+3*A3_number_zones)+1):(2*A1_number_zones+4*A3_number_zones)) =
    A6_zone_normal_vector;

%-----
%-----

%Creating a complete matrix of the coordinates of the volume zones

V_zone_coordinates = zeros(V1_number_zones,4);
V_zone_normal_vector = zeros(V1_number_zones,4);

counter = 0; %matrix counter

for k = 0:(V1_z_number_subd-1);
    for j = 0:(V1_y_number_subd-1);
        for i = 0:(V1_x_number_subd-1);
            %Area 1 starts at origin and the x-
            coordinate stays at 0 for all Area1_zone coordinates
            counter = counter + 1;
            V1_zone_coors = i*V1_step + V1_step/2;
            V1_zone_coory = j*V1_step + V1_step/2; %Coordinates of center of each CV, with the
            bottom corner of the first CV starting at 0,0,0
            V1_zone_coorz = k*V1_step + V1_step/2;
            V_zone_coordinates(counter,:) = [counter V1_zone_coors V1_zone_coory V1_zone_coorz];
            V_zone_normal_vector(counter,:) = [counter ((-1)^counter)*0.57735 ((-1)^(j+1)*0.57735) ((-1)^(k+1)
            *0.57735)];
        end
    end
end

%-----
%-----

%Surface-Surface Direct Exchange Areas

%General Parameters
Total_surface_zones = 2*A1_number_zones+4*A3_number_zones;
A_zone_area = A1_step^2;

%-----
%Direct Exchange Areas from A1
%-----

Direct_Exchange_A1_A2 = zeros(A1_number_zones*A2_number_zones,8);
a1a2_non_zero_matrix = zeros(Total_surface_zones, Total_surface_zones);
theta_matrix = zeros(A1_number_zones,2);

for i = 1:A1_number_zones;

    A1_zone_coors = A_zone_coordinates(i,2); %coordinates for the control volume
    A1_zone_coory = A_zone_coordinates(i,3);
    A1_zone_coorz = A_zone_coordinates(i,4);
    A1_zone_unitvector = A_zone_normal_vector(i,2:4);

    for j = A1_number_zones+1:Total_surface_zones;

        A2_zone_coors = A_zone_coordinates(j,2);
        A2_zone_coory = A_zone_coordinates(j,3);
        A2_zone_coorz = A_zone_coordinates(j,4);
        A2_zone_unitvector = A_zone_normal_vector(j,2:4);

        vector_line_A1_to_A2 = [A2_zone_coors - A1_zone_coors, A2_zone_coory - A1_zone_coory, A2_zone_coorz -
            A1_zone_coorz];
        vector_line_A2_to_A1 = [A1_zone_coors - A2_zone_coors, A1_zone_coory - A2_zone_coory, A1_zone_coorz -
            A2_zone_coorz];
    end
end

```

```

distance_A1_to_A2 = sqrt((A2_zone_coorx - A1_zone_coorx)^2 + (A2_zone_coory - A1_zone_coory)^2 + (
    A2_zone_coorz - A1_zone_coorz)^2);
distance_A2_to_A1 = sqrt((A1_zone_coorx - A2_zone_coorx)^2 + (A1_zone_coory - A2_zone_coory)^2 + (
    A1_zone_coorz - A2_zone_coorz)^2);
cos_theta_A1 = (A1_zone_unitvector(1)*vector_line_A1_to_A2(1) + (A1_zone_unitvector(2)*
    vector_line_A1_to_A2(2)) + A1_zone_unitvector(3)*vector_line_A1_to_A2(3)) / distance_A1_to_A2;
cos_theta_A2 = (A2_zone_unitvector(1)*vector_line_A2_to_A1(1) + (A2_zone_unitvector(2)*
    vector_line_A2_to_A1(2)) + A2_zone_unitvector(3)*vector_line_A2_to_A1(3)) / distance_A1_to_A2;

    ala2_non_zero_matrix(i,j) = exp(-kappa*distance_A1_to_A2) * cos_theta_A1 * cos_theta_A2 * A_zone_area*
        A_zone_area / (pi * distance_A1_to_A2^2);
end

end

%=====
%Direct Exchange Areas from A2
%=====
for i = (A1_number_zones+1):2*A1_number_zones;

    A1_zone_coorx = A_zone_coordinates(i,2); %coordinates for the control volume
    A1_zone_coory = A_zone_coordinates(i,3);
    A1_zone_coorz = A_zone_coordinates(i,4);
    A1_zone_unitvector = A_zone_normal_vector(i,2:4);

    for j = 2*A1_number_zones+1:Total_surface_zones;

        A2_zone_coorx = A_zone_coordinates(j,2);
        A2_zone_coory = A_zone_coordinates(j,3);
        A2_zone_coorz = A_zone_coordinates(j,4);
        A2_zone_unitvector = A_zone_normal_vector(j,2:4);

        vector_line_A1_to_A2 = [A2_zone_coorx - A1_zone_coorx, A2_zone_coory - A1_zone_coory, A2_zone_coorz -
            A1_zone_coorz];
        vector_line_A2_to_A1 = [A1_zone_coorx - A2_zone_coorx, A1_zone_coory - A2_zone_coory, A1_zone_coorz -
            A2_zone_coorz];
        distance_A1_to_A2 = sqrt((A2_zone_coorx - A1_zone_coorx)^2 + (A2_zone_coory - A1_zone_coory)^2 + (
            A2_zone_coorz - A1_zone_coorz)^2);
        distance_A2_to_A1 = sqrt((A1_zone_coorx - A2_zone_coorx)^2 + (A1_zone_coory - A2_zone_coory)^2 + (
            A1_zone_coorz - A2_zone_coorz)^2);
        cos_theta_A1 = (A1_zone_unitvector(1)*vector_line_A1_to_A2(1) + (A1_zone_unitvector(2)*
            vector_line_A1_to_A2(2)) + A1_zone_unitvector(3)*vector_line_A1_to_A2(3)) / distance_A1_to_A2;
        cos_theta_A2 = (A2_zone_unitvector(1)*vector_line_A2_to_A1(1) + (A2_zone_unitvector(2)*
            vector_line_A2_to_A1(2)) + A2_zone_unitvector(3)*vector_line_A2_to_A1(3)) / distance_A1_to_A2;

        ala2_non_zero_matrix(i,j) = exp(-kappa*distance_A1_to_A2) * cos_theta_A1 * cos_theta_A2 * A_zone_area
            *A_zone_area / (pi * distance_A1_to_A2^2);
    end

end

%=====
%Direct Exchange Areas from A3
%=====
for i = (2*A1_number_zones+1):(2*A1_number_zones+A3_number_zones);

    A1_zone_coorx = A_zone_coordinates(i,2); %coordinates for the control volume
    A1_zone_coory = A_zone_coordinates(i,3);
    A1_zone_coorz = A_zone_coordinates(i,4);
    A1_zone_unitvector = A_zone_normal_vector(i,2:4);

    for j = (2*A1_number_zones+A3_number_zones)+1:Total_surface_zones;

        A2_zone_coorx = A_zone_coordinates(j,2);
        A2_zone_coory = A_zone_coordinates(j,3);
        A2_zone_coorz = A_zone_coordinates(j,4);
        A2_zone_unitvector = A_zone_normal_vector(j,2:4);

        vector_line_A1_to_A2 = [A2_zone_coorx - A1_zone_coorx, A2_zone_coory - A1_zone_coory, A2_zone_coorz -
            A1_zone_coorz];
        vector_line_A2_to_A1 = [A1_zone_coorx - A2_zone_coorx, A1_zone_coory - A2_zone_coory, A1_zone_coorz -
            A2_zone_coorz];
        distance_A1_to_A2 = sqrt((A2_zone_coorx - A1_zone_coorx)^2 + (A2_zone_coory - A1_zone_coory)^2 + (
            A2_zone_coorz - A1_zone_coorz)^2);
        distance_A2_to_A1 = sqrt((A1_zone_coorx - A2_zone_coorx)^2 + (A1_zone_coory - A2_zone_coory)^2 + (
            A1_zone_coorz - A2_zone_coorz)^2);
        cos_theta_A1 = (A1_zone_unitvector(1)*vector_line_A1_to_A2(1) + (A1_zone_unitvector(2)*
            vector_line_A1_to_A2(2)) + A1_zone_unitvector(3)*vector_line_A1_to_A2(3)) / distance_A1_to_A2;

```

```

        cos_theta_A2 = (A2_zone_unitvector(1)*vector_line_A2_to_A1(1) + (A2_zone_unitvector(2)*
            vector_line_A2_to_A1(2)) + A2_zone_unitvector(3)*vector_line_A2_to_A1(3)) / distance_A1_to_A2;

        ala2_non_zero_matrix(i,j) = exp(-kappa*distance_A1_to_A2) * cos_theta_A1 * cos_theta_A2 * A_zone_area
            *A_zone_area / (pi * distance_A1_to_A2^2);
    end

end

%=====
%Direct Exchange Areas from A4
%=====
for i = ((2*A1_number_zones+A3_number_zones)+1):(2*A1_number_zones+2*A3_number_zones);

    A1_zone_coors = A_zone_coordinates(i,2); %coordinates for the control volume
    A1_zone_coory = A_zone_coordinates(i,3);
    A1_zone_coors = A_zone_coordinates(i,4);
    A1_zone_unitvector = A_zone_normal_vector(i,2:4);

    for j = (2*A1_number_zones+2*A3_number_zones)+1:Total_surface_zones;

        A2_zone_coors = A_zone_coordinates(j,2);
        A2_zone_coory = A_zone_coordinates(j,3);
        A2_zone_coors = A_zone_coordinates(j,4);
        A2_zone_unitvector = A_zone_normal_vector(j,2:4);

        vector_line_A1_to_A2 = [A2_zone_coors - A1_zone_coors, A2_zone_coory - A1_zone_coory, A2_zone_coors -
            A1_zone_coors];
        vector_line_A2_to_A1 = [A1_zone_coors - A2_zone_coors, A1_zone_coory - A2_zone_coory, A1_zone_coors -
            A2_zone_coors];
        distance_A1_to_A2 = sqrt((A2_zone_coors - A1_zone_coors)^2 + (A2_zone_coory - A1_zone_coory)^2 + (
            A2_zone_coors - A1_zone_coors)^2);
        distance_A2_to_A1 = sqrt((A1_zone_coors - A2_zone_coors)^2 + (A1_zone_coory - A2_zone_coory)^2 + (
            A1_zone_coors - A2_zone_coors)^2);
        cos_theta_A1 = (A1_zone_unitvector(1)*vector_line_A1_to_A2(1) + (A1_zone_unitvector(2)*
            vector_line_A1_to_A2(2)) + A1_zone_unitvector(3)*vector_line_A1_to_A2(3)) / distance_A1_to_A2;
        cos_theta_A2 = (A2_zone_unitvector(1)*vector_line_A2_to_A1(1) + (A2_zone_unitvector(2)*
            vector_line_A2_to_A1(2)) + A2_zone_unitvector(3)*vector_line_A2_to_A1(3)) / distance_A1_to_A2;

        ala2_non_zero_matrix(i,j) = exp(-kappa*distance_A1_to_A2) * cos_theta_A1 * cos_theta_A2 * A_zone_area
            *A_zone_area / (pi * distance_A1_to_A2^2);
    end

end

%=====
%Direct Exchange Areas from A5
%=====
for i = ((2*A1_number_zones+2*A3_number_zones)+1):(2*A1_number_zones+3*A3_number_zones);

    A1_zone_coors = A_zone_coordinates(i,2); %coordinates for the control volume
    A1_zone_coory = A_zone_coordinates(i,3);
    A1_zone_coors = A_zone_coordinates(i,4);
    A1_zone_unitvector = A_zone_normal_vector(i,2:4);

    for j = (2*A1_number_zones+3*A3_number_zones)+1:Total_surface_zones;

        A2_zone_coors = A_zone_coordinates(j,2);
        A2_zone_coory = A_zone_coordinates(j,3);
        A2_zone_coors = A_zone_coordinates(j,4);
        A2_zone_unitvector = A_zone_normal_vector(j,2:4);

        vector_line_A1_to_A2 = [A2_zone_coors - A1_zone_coors, A2_zone_coory - A1_zone_coory, A2_zone_coors -
            A1_zone_coors];
        vector_line_A2_to_A1 = [A1_zone_coors - A2_zone_coors, A1_zone_coory - A2_zone_coory, A1_zone_coors -
            A2_zone_coors];
        distance_A1_to_A2 = sqrt((A2_zone_coors - A1_zone_coors)^2 + (A2_zone_coory - A1_zone_coory)^2 + (
            A2_zone_coors - A1_zone_coors)^2);
        distance_A2_to_A1 = sqrt((A1_zone_coors - A2_zone_coors)^2 + (A1_zone_coory - A2_zone_coory)^2 + (
            A1_zone_coors - A2_zone_coors)^2);
        cos_theta_A1 = (A1_zone_unitvector(1)*vector_line_A1_to_A2(1) + (A1_zone_unitvector(2)*
            vector_line_A1_to_A2(2)) + A1_zone_unitvector(3)*vector_line_A1_to_A2(3)) / distance_A1_to_A2;
        cos_theta_A2 = (A2_zone_unitvector(1)*vector_line_A2_to_A1(1) + (A2_zone_unitvector(2)*
            vector_line_A2_to_A1(2)) + A2_zone_unitvector(3)*vector_line_A2_to_A1(3)) / distance_A1_to_A2;

        ala2_non_zero_matrix(i,j) = exp(-kappa*distance_A1_to_A2) * cos_theta_A1 * cos_theta_A2 * A_zone_area
            *A_zone_area / (pi * distance_A1_to_A2^2);
    end

end

```

```

end

ala2_non_zero_transposed_matrix = ala2_non_zero_matrix';
ala2_matrix = ala2_non_zero_matrix + ala2_non_zero_transposed_matrix;

%-----
%-----

%Volume-Surface Direct Exchange Areas
V1_zone_volume = V1_step^3;
gls1_matrix = zeros(V1_number_zones, Total_surface_zones);

for i = 1:V1_number_zones;

    V1_zone_coorx = V_zone_coordinates(i,2); %coordinates for the control volume
    V1_zone_coory = V_zone_coordinates(i,3);
    V1_zone_coorz = V_zone_coordinates(i,4);
    V1_zone_unitvector = V_zone_normal_vector(i,2:4);

    for j = 1:Total_surface_zones;

        A1_zone_coorx = A_zone_coordinates(j,2);
        A1_zone_coory = A_zone_coordinates(j,3);
        A1_zone_coorz = A_zone_coordinates(j,4);
        A1_zone_unitvector = A_zone_normal_vector(j,2:4);

        vector_line_V1_to_A1 = [A1_zone_coorx - V1_zone_coorx, A1_zone_coory - V1_zone_coory,
                                A1_zone_coorz - V1_zone_coorz];
        vector_line_A1_to_V1 = [V1_zone_coorx - A1_zone_coorx, V1_zone_coory - A1_zone_coory,
                                V1_zone_coorz - A1_zone_coorz];
        distance_V1_to_A1 = sqrt((A1_zone_coorx - V1_zone_coorx)^2 + (A1_zone_coory - V1_zone_coory)^2 + (
                                A1_zone_coorz - V1_zone_coorz)^2);
        distance_A1_to_V1 = sqrt((V1_zone_coorx - A1_zone_coorx)^2 + (V1_zone_coory - A1_zone_coory)^2 + (
                                V1_zone_coorz - A1_zone_coorz)^2);
        cos_theta_A1 = (A1_zone_unitvector(1)*vector_line_A1_to_V1(1) + (A1_zone_unitvector(2)*
                                vector_line_A1_to_V1(2)) + A1_zone_unitvector(3)*vector_line_A1_to_V1(3)) /
                                distance_A1_to_V1;

        %We don't need to physically calculate the angle, only the cos_of_angle, and for vector_A1_to_A2 we need to use
        %zone_A1's normal_vector, since it starts at A1 and points away (like figure 17-2 (Modest) shows)
        %We use the definition of the dot product between two vectors to calculate the cos_of_angle. The size of the normal
        %vector is only 1 due to the geometry of our enclosure
        cos_theta_V1 = dot(V1_zone_unitvector, vector_line_V1_to_A1) / (distance_V1_to_A1 * 1);
        theta_V1 = acos(dot(V1_zone_unitvector, vector_line_V1_to_A1) / (distance_V1_to_A1 * 1));

        if theta_V1 <= 0.5*pi + 0.01

            if distance_V1_to_A1 <= (A1_step/D_pebble)*D_pebble + 0.001
                gls1_sphere = cos_theta_A1*A_zone_area*pi*(0.5*D_pebble)^2 / (8*pi * distance_V1_to_A1
                    ^2);
            else
                gls1_sphere = exp(-kappa*distance_V1_to_A1)* cos_theta_A1*A_zone_area*pi*(0.5*D_pebble
                    )^2 / (8*pi * distance_V1_to_A1^2);
            end
            gls1_matrix(i,j) = A_random * factor_ss * (gls1_sphere / A_p_section); %Convert sphere
            -centred DEA to random bed DEA
        end
    end
end

%-----
%-----

%Volume-volume Direct Exchange Areas
%We only calculate the entries above the diagonal; the rest is symmetrical
gls2_non_zero_matrix = zeros(V1_number_zones, V1_number_zones);

for i = 1:V1_number_zones;

    V1_zone_coorx = V_zone_coordinates(i,2); %coordinates for the control volume
    V1_zone_coory = V_zone_coordinates(i,3);
    V1_zone_coorz = V_zone_coordinates(i,4);
    V1_zone_unitvector = V_zone_normal_vector(i,2:4);

    for j = (i+1):V1_number_zones;

```

```

V2_zone_coors = V_zone_coordinates(j,2);
V2_zone_coory = V_zone_coordinates(j,3);
V2_zone_coorz = V_zone_coordinates(j,4);
V2_zone_unitvector = V_zone_normal_vector(j,2:4);

vector_line_V1_to_V2 = [V2_zone_coors - V1_zone_coors, V2_zone_coory - V1_zone_coory, V2_zone_coorz -
    V1_zone_coorz];
distance_V1_to_V2 = sqrt((V2_zone_coors - V1_zone_coors)^2 + (V2_zone_coory - V1_zone_coory)^2 + (
    V2_zone_coorz - V1_zone_coorz)^2);
cos_theta_V1 = dot(V1_zone_unitvector, vector_line_V1_to_V2) / (distance_V1_to_V2 * 1);
theta_V1 = acos(dot(V1_zone_unitvector, vector_line_V1_to_V2) / (distance_V1_to_V2 * 1));

if theta_V1 <= 0.5*pi + 0.01
    if distance_V1_to_V2 <= (A1_step/D_pebble)*D_pebble + 0.001
        glg2_sphere = pi*(0.5*D_pebble)^2*(pi*(0.5*D_pebble)^2) / (8*pi * distance_V1_to_V2^2);
    else
        glg2_sphere = (exp(-kappa*distance_V1_to_V2)*pi*(0.5*D_pebble)^2*(pi*(0.5*D_pebble)^2)) / (8*
            pi * distance_V1_to_V2^2);
    end
    glg2_non_zero_matrix(i,j) = A_random * factor_ss * (glg2_sphere / A_p_section); %Convert sphere-
        centred DEA to random bed DEA;
end
end
end

%Creating the full volume-volume exchange matrix by summing the two
%non-zero matrices
glg2_non_zero_transp_matrix = glg2_non_zero_matrix';
glg2_matrix = glg2_non_zero_matrix + glg2_non_zero_transp_matrix;

%-----
%-----

%Creating the X_all_matrix which contains all the exchange areas of both
%the volume and surface zones
Total_zones_all = Total_surface_zones + V1_number_zones; %For this program we use both the surface zones and volume
    zones

slg1_matrix = gls1_matrix'; %We create the surface-volume exchange areas which are the transpose of the volume-surface
    direct exchange areas

X_all_matrix = zeros(Total_zones_all, Total_zones_all);

X_all_matrix(1:Total_surface_zones, 1:Total_surface_zones) = ala2_matrix;
X_all_matrix(1:Total_surface_zones, (Total_surface_zones+1):Total_zones_all) = slg1_matrix;
X_all_matrix((Total_surface_zones+1):Total_zones_all, 1:Total_surface_zones) = gls1_matrix;
X_all_matrix((Total_surface_zones+1):Total_zones_all, (Total_surface_zones+1):Total_zones_all) = glg2_matrix;

%-----
%-----

% Calculate the control volume's internal radiation - i.e. the volume
% zones' non-zero diagonals
for i = Total_surface_zones + 1: Total_zones_all

    Sum_zone_volumes = sum(X_all_matrix(i,:));
    DEA_internal = A_random - Sum_zone_volumes;
    X_all_matrix(i,i) = DEA_internal;

end

% %-----
% %-----
%Least Squares Smoothing using Lagrange Multipliers

c_LG = zeros(Total_zones_all,1);
delta_LG = zeros(Total_zones_all,1);
r_LG = zeros(Total_zones_all, Total_zones_all);
w_LG = zeros(Total_zones_all, Total_zones_all);
X_all_matrix_adjusted = zeros(Total_zones_all, Total_zones_all);
Lamda_LG_new = zeros(Total_zones_all,1);
Lamda_Delta = zeros(Total_zones_all,1);

relaxation_factor = 1;

```

---

```

for h = 1:number_iterations;

    Lamda_LG = Lamda_LG_new;

    w_LG = (X_all_matrix).^2;

    for i = 1:Total_zones_all;                                     %Setting up elements for equation 11

        if i <= Total_surface_zones
            c_LG(i,1) = A_zone_area;
        else
            %c_LG(i,1) = 4*kappa*V1_zone_volume;
            c_LG(i,1) = A_random; %0.125*4*pi*(0.5*D_pebble)^2; %It is now an 1/8th of the original
        end
        delta_LG(i,1) = c_LG(i,1) - sum(X_all_matrix(i,:));
    end

    for i = 1:Total_zones_all;
        for j = 1:Total_zones_all;
            if i == j
                r_LG(i,j) = w_LG(i,j) + sum(w_LG(i,:));
            else
                r_LG(i,j) = w_LG(i,j);
            end
        end
    end

    Lamda_LG_new = r_LG \ delta_LG;

    for i = 1:Total_zones_all;
        for j = 1:Total_zones_all;
            X_all_matrix_adjusted(i,j) = X_all_matrix(i,j) + w_LG(i,j) * (Lamda_LG_new(i) + Lamda_LG_new(j));
        end
    end

    Error_Lamda = sum((Lamda_LG_new - relaxation_factor*Lamda_LG).^2)
    X_all_matrix = X_all_matrix_adjusted;

end

%-----

%General parameters
relax_f = 1.01; %Relaxation factor for Newton-Raphson
emmissivity_front = 0.8; %Assume emmissivity as 1 for now to
    model blackbody radiation
emmissivity_sides = 0.68;
emmissivity_vol = 0.8;
sigma = 5.670373 * 10^(-8); %Stefan-Boltzman constant in SI Units

%Specify c_i as 1 if Temperature is specified ,
%Specify c_i as 0 if Q_i is specified for the relevant surfaces
c_front = 1;
c_back = 1;
c_sides = 0;
c_spheres = 0;

%Temperatures
T_A1 = 600 + 273.15; %Degrees Kelvin
T_A2 = 105 + 273.15; %Degrees Kelvin
T_A3 = 300 + 273.15; %Degrees Kelvin
T_A4 = 300 + 273.15; %Degrees Kelvin
T_A5 = 300 + 273.15; %Degrees Kelvin
T_A6 = 300 + 273.15; %Degrees Kelvin
T_V = 300 + 273.15; %Degrees Kelvin

%Heat values
Q_A1 = 933; %Watts for front surface
Q_A2 = -703.8; %Watts for back surface
Q_sides = -229.8; %Watts for side surfaces
Q_V = 0; %Watts for volume

```



```

%Emmisivity and Reflectivity Array
emmisivity_i(1:2*A1_number_zones,1) = emmisivity_front;
emmisivity_i(2*A1_number_zones+1:Total_surface_zones,1) = emmisivity_sides;
emmisivity_i(Total_surface_zones+1:Total_zones_all,1) = emmisivity_vol;

%Coefficient array
c_i(1:A1_number_zones,1) = c_front;
c_i((A1_number_zones+1):2*A1_number_zones,1) = c_back;
c_i((2*A1_number_zones+1):(Total_surface_zones),1) = c_sides;
c_i(Total_surface_zones+1:Total_zones_all,1) = c_spheres;

A_si(1:Total_surface_zones,1) = A_zone_area;
A_si(Total_surface_zones+1:Total_zones_all,1) = A_random;

%Guess Values
x_i(1:A1_number_zones,1) = Q_A1/A1_number_zones;
x_i((A1_number_zones+1):2*A1_number_zones,1) = Q_A2/A2_number_zones;
x_i((2*A1_number_zones+1):Total_surface_zones,1) = T_A3;
x_i(Total_surface_zones+1:Total_zones_all,1) = T_V;

%Temperature Array
T_i(1:A1_number_zones,1) = T_A1;
T_i((A1_number_zones+1):2*A1_number_zones,1) = T_A2;
T_i((2*A1_number_zones+1):Total_surface_zones,1) = x_i((2*A1_number_zones+1):Total_surface_zones,1);
T_i(Total_surface_zones+1:Total_zones_all,1) = x_i(Total_surface_zones+1:Total_zones_all,1);

%Heat array
Q_A(1:A1_number_zones,1) = Q_A1 / A1_number_zones;%x_i(1:A1_number_zones,1);
Q_A((A1_number_zones+1):2*A1_number_zones,1) = Q_A2 / A2_number_zones;
Q_A((2*A1_number_zones+1):Total_surface_zones,1) = Q_sides / (4*A3_number_zones);
Q_A(Total_surface_zones+1:Total_zones_all,1) = Q_V / V1_number_zones;

zone_coordinates(1:Total_surface_zones,1:3) = A_zone_coordinates(:,2:4);
zone_coordinates(Total_surface_zones+1:Total_zones_all,1:3) = V_zone_coordinates(:,2:4);

%-----
%-----
%Setting up the net heat equations
%To be solved with Newton–Raphson
%-----
%-----

% userview = memory

countiter = 0;

for loop = 1:2000

tic

    countiter = countiter + 1;
    fprintf('Iteration %d', countiter);

    %Conduction MSUC Model – Near–Wall and Bulk
    %-----

    k_c      = zeros(Total_zones_all,1);
    radius_x  = zeros(Total_zones_all,1);
    porosity  = zeros(Total_zones_all,1);
    Distance  = zeros(Total_zones_all,1);
    R_T_ij_old = zeros(Total_zones_all, Total_zones_all);

    gas_constant = 287; %j/kg–K gas constant for Nitrogen from engineering toolbox

    for i = 1:Total_zones_all

        coord_x = zone_coordinates(i,1);
        coord_y = zone_coordinates(i,2);
        coord_z = zone_coordinates(i,3);

        Z_depth = coord_y; %The height in the bed where the control volume resides

        disx1 = coord_x - 0;
        disx2 = Volume_thickness - coord_x;
        disz1 = coord_z - 0;
        disz2 = A1_side_length - coord_z;
    
```

```

%First Assumption — Weighted average between two walls
%(Reinecke 2010) — Disregard height of bed for now
a = disx1/D_pebble;
b = disz1/D_pebble;
inscription_x = find(abs(porosity_distance_DK-a) < 0.001); %A tolerance must be added due to floating
point roundoff errors
inscription_y = find(abs(porosity_distance_DK-b) < 0.001); %A tolerance must be added due to floating
point roundoff errors
porosity_x = porosity_x_DK(inscription_x);
porosity_z = porosity_z_DK(inscription_y);
porosity(i,1) = ((Volume_thickness-disx1)*porosity_x + (A1_side_length-disz1)*porosity_z) / ((
Volume_thickness-disx1) + (A1_side_length-disz1));

N_bar_c = 25.952*porosity(i,1)^3 -62.364*porosity(i,1)^2 + 39.724*porosity(i,1) - 2.0233;
phi_bar_c = -6.1248*N_bar_c^2 + 73.419*N_bar_c - 186.68;
phi_bar_c_rad = phi_bar_c * pi/180;

%Hertzian Resistance
k_s = 186.021 - 39.5408e-2 * (T_i(i,1)-273.15) + 4.8852e-4*(T_i(i,1)-273.15)^2 - 2.91e-7 * (T_i(i,1)
-273.15)^3 + 6.6e-11*(T_i(i,1)-273.15)^4;
%k_s = 0.035*(T_i(i,1)-273.15);
F_bah = 72.307*Z_depth+7.8716;
r_eq = r_pebble;
mu = 0.3;
E_young = 7.41e9;
r_c = (0.75 * F_bah * r_eq /E_young)^(1/3);
omega_0 = r_c^2/(2*r_pebble); %Assume that the deformation depth at origin is 0 for now

%-----

%Lamda Resistance — for gas?
T_00 = 273.15;
T_k = T_i(i,1);
M_gg = 14.0067; %Molar mass of Nitrogen
M_star = M_gg; %1.4*M_gg; Helium is used in the SANA-I while Nitrogen is used in HTTU
M_ss = 12;
mu_vis = M_gg / M_ss;
alpha_T1 = exp(-0.57*((T_k-T_00)/T_00)) * (M_star/(6.8+M_star)) + (2.4*mu_vis)/(1+mu_vis)^2 * (1-exp
(-0.57*((T_k-T_00)/T_00)));
alpha_T2 = alpha_T1;
cp = 1e-10*T_k^4-6e-7*T_k^3+0.0009*T_k^2-0.3867*T_k+1084.9; %Specific heat — regression from
engineeringtoolbox data
cv = cp-gas_constant; %Speific heat — estimate
gamma_f = cp / cv;
lamda_meanfree_0 = 0.7387e-7;
T_g = T_k;
P_0 = 10000; %Just check these again please
P_g = 10000; %Just check these again please
T_0 = 273.15; %Just check these again please
lamda_meanfree = (P_0*T_g)/(P_g*T_0) * lamda_meanfree_0;
Pr = 0.74; %Estimate of Prandtl number for Nitrogen from engineeringtoolbox
j_gas = (((1-alpha_T1)/alpha_T1) + ((1-alpha_T2)/alpha_T2))*((2*gamma_f)/(1+gamma_f)) * (1/Pr) *
lamda_meanfree;
AA = 2*r_pebble + j_gas - omega_0;

radius_lambda = sqrt(r_pebble^2 - (r_pebble-0.5*omega_0-5*lamda_meanfree)^2);
BB = sqrt(r_pebble^2 - radius_lambda^2);

mu_sphere = 0.3;
a_H = ((0.75*F_bah*r_eq*(1-mu_sphere^2))/E_young)^(1/3);
CC = sqrt(r_pebble^2 - a_H^2);
k_f = 0.0557251+0.000357143*T_k -4.87013e-8*T_k^2;

%Gas Resistance
A_G = 2*r_pebble - omega_0;
B_G = sqrt(r_pebble^2 - radius_lambda^2);
%R_G = 2 / (pi*k_f*(A_G*log(abs(A_G/(A_G-2*B_G)))-2*B_G));

%Outer Resistance
A_out = r_pebble - 2*(0.5*omega_0+5*lamda_meanfree);
B_out = sqrt(r_pebble^2-radius_lambda^2);

```

```

%-----
%-----
%Conduction MSUC Model - Wall
%-----
%-----

%Hertzian Resistance
k_s_star = 60;
%R_hertz_w_12 = 0.64 / (k_s_star * r_c);
%-----

%Lamda Resistance - for gas?
AA_w = r_pebble+j_gas - omega_0;
radius_lambda_wall = sqrt(r_pebble^2 - (r_pebble-omega_0-10*lambda_meanfree)^2);
BB_w = sqrt(r_pebble^2 - radius_lambda_wall^2);

%-----
%Gas Resistance
A_G_w = r_pebble - omega_0;
B_G_w = sqrt(r_pebble^2 - radius_lambda_wall^2);

%-----
%Outer Resistance
A_out_w = r_pebble - 2*(omega_0+10*lambda_meanfree);
B_out_w = sqrt(r_pebble^2 - radius_lambda_wall^2);

%-----
%Combined Resistance R_j
% R_j_w = (1/R_hertz_w_12 + 1/R_lamda_w + 1/R_G_w)^(-1) + (1/R_B_in_w_12 + 1/R_B_mid_w_12 + 1/R_B_out_w_12)
% ^(-1);
%-----

%Thermal Conductivity due to conduction in bulk & Near-wall region
% k_c_w = (r_pebble - omega_0) / (D_pebble^2 * R_j_w) %Effective thermal conductivity for conduction in
% the bulk/near-wall region
%-----

%Calculation for k_c for wall, near-wall and bulk regions

if disx1 <=r_pebble || disx2 <=r_pebble || disz1 <=r_pebble || disz2 <=r_pebble
    R_hertz_w_12 = 0.64 / (k_s * r_c);
    R_lamda_w = 1 / (2*pi*k_f*(AA_w*log(abs((BB_w-AA_w)/(CC-AA_w))+BB_w-CC)));
    R_G_w = 1 / (2*pi*k_f*(A_G_w*log(abs(A_G_w/(B_G_w-A_G_w))-B_G_w)));
    R_B_in_w_12 = (D_pebble - omega_0)/(2*k_s*pi*r_c^2);
    R_B_mid_w_12 = (D_pebble - omega_0)/(2*k_s*pi*(radius_lambda_wall-a_H)^2);
    R_B_out_w_12 = (log(abs((A_out_w+B_out_w)/(A_out_w-B_out_w)))/(2*k_s*pi*B_out_w));
    R_ij = (1/R_hertz_w_12 + 1/R_lamda_w + 1/R_G_w)^(-1) + (1/R_B_in_w_12 + 1/R_B_mid_w_12 + 1/
        R_B_out_w_12)^(-1);
    k_c(i,1) = (r_pebble - omega_0) / (D_pebble^2 * R_ij);
else
    R_hertz_12 = 0.64 / (k_s * r_c);
    R_lamda = 2 / (pi*k_f*(AA*log(abs((AA-2*BB)/(AA-2*CC))+2*BB-2*CC)));
    R_G = 2 / (pi*k_f*(A_G*log(abs(A_G/(A_G-2*B_G))-2*B_G)));
    R_B_in_12 = (D_pebble - omega_0)/(k_s*pi*r_c^2);
    R_B_mid_12 = (D_pebble - omega_0)/(k_s*pi*(radius_lambda^2-a_H^2));
    R_B_out_12 = (log(abs((A_out+B_out)/(A_out-B_out)))/(k_s*pi*B_out));
    R_ij = (1/R_hertz_12 + 1/R_lamda + 1/R_G)^(-1) + (1/R_B_in_12 + 1/R_B_mid_12 + 1/R_B_out_12)^(-1);
    k_c(i,1) = N_bar_c * (D_pebble - omega_0) * sin(phi_bar_c_rad) / (2*D_pebble^2 * R_ij);
end

x_coor_i = zone_coordinates(i,1);
y_coor_i = zone_coordinates(i,2);
z_coor_i = zone_coordinates(i,3);

for j = i+1:Total_zones_all

    x_coor_j = zone_coordinates(j,1);
    y_coor_j = zone_coordinates(j,2);
    z_coor_j = zone_coordinates(j,3);

    Distance(i,j) = sqrt((x_coor_j-x_coor_i)^2+(y_coor_j-y_coor_i)^2+(z_coor_j-z_coor_i)^2);

```

```

        if Distance(i,j) <= (r_pebble + 0.0001) && i <= Total_surface_zones
            if j <= Total_surface_zones
                R_T_ij_old(i,j) = 0;
            else
                R_T_ij_old(i,j) = R_ij^(-1); %The inverse of the resistances is used in most of the instances
            end
        elseif Distance(i,j) <= (r_pebble + 0.0001) && i > Total_surface_zones
            if j == i
                R_T_ij_old(i,j) = 0;
            else
                R_T_ij_old(i,j) = R_ij^(-1); %The inverse of the resistances is used in most of the instances
            end
        end

    end

end

R_T_ij = (R_T_ij_old + R_T_ij_old') - eye(size(R_T_ij_old,1)).*diag(R_T_ij_old);
Distance = (Distance + Distance') - eye(size(Distance,1)).*diag(Distance);

%-----
%Calculate the Q_j part of Part 3
%-----
subterm3_matrix = -R_T_ij .* (T_i');
term3 = sum(subterm3_matrix,2);

%-----
%Calculate Parts 1, 2 and 3 (Part with conduction)
%-----
Part1a = (X_all_matrix.') .* (emmisivity_i); %Don't transpose e_i, that way we can multiply with e(i) instead of e
(j);
Part1c = Part1a .* (((emmisivity_i .* A_si) ./ (ones(Total_zones_all,1) - emmisivity_i))); %Some doubt
diag1 = diag(diag(Part1c) - 1); %The diagonal of Part1 needs a '-1'; Expanding the diagonal
Part1 = (Part1c + diag1 - diag(diag(Part1a))) .* (Q_A');

Part2c = -Part1a;
diag2 = diag(diag(Part2c) + (emmisivity_i .* A_si));
E_bb = sigma*(T_i.^4);
Part2 = (Part2c + diag2 - diag(diag(Part2c))) .* E_bb'; %Since the diagonal of Part2c is NOT all zeros, we need to
subtract the expanded matrix of its diagonal to avoid duplicating its sum

Part3a = -Part1c;
diag3 = diag(Part3a) + 1;
Part3diag = diag(diag3);
Part3a = Part3a + Part3diag - diag(diag(Part3a));
Part3b = sum(R_T_ij,2) .* T_i; %Some doubt
Part3 = Part3a .* (Part3b + term3)';

A_matrix = Part1 + Part2 + Part3;

first = 1;
second = 2*A1_number_zones;
dPart1a = (Part1c + diag1 - diag(diag(Part1a)));
dPart1 = zeros(Total_zones_all, Total_zones_all);
dPart1(:, first:second) = dPart1a(:, first:second);
clear dPart1a

third = 2*A1_number_zones + 1;
fourth = Total_zones_all;
dPart2a = (Part2c + diag2 - diag(diag(Part2c)));
dE_bb = sigma*(T_i.^3);
dPart2 = zeros(Total_zones_all, Total_zones_all);
dPart2(:, third:fourth) = 4 * dPart2a(:, third:fourth) .* dE_bb(third:fourth)';

dR_T = sum(R_T_ij,2);
dPart3 = zeros(Total_zones_all, Total_zones_all);
dPart3(:, third:fourth) = Part3a(:, third:fourth) .* dR_T(third:fourth)';

dphi_dxj = dPart1 + dPart2 + dPart3;

%-----
% Newton-Raphson Method
%-----

% Partial Derivatives

```

```

%-----
minus_phi_n = -sum(A_matrix,2);

%Calculate delta_x_n by matrix inversion
%-----
DELTA_X = dphi_dxj \ minus_phi_n;

%Update guess values
%-----
x_i = x_i + relax_f*DELTA_X;

%Temperature array — Update the guess values for the unknown temperature
T_i(1:A1_number_zones,1) = x_i(1:A1_number_zones,1);
T_i((2*A1_number_zones+1):Total_surface_zones,1) = x_i((2*A1_number_zones+1):Total_surface_zones,1);
T_i(Total_surface_zones+1:Total_zones_all,1) = x_i(Total_surface_zones+1:Total_zones_all,1);

%Heat array — Update the guess values for the unknown heat
Q_A(1:A1_number_zones,1) = x_i(1:A1_number_zones,1);
Q_A((A1_number_zones+1):2*A1_number_zones,1) = x_i((A1_number_zones+1):2*A1_number_zones,1);

fprintf('...Done\n');

Q_i_total = sum(Q_A(1:A1_number_zones));
Q_o_total = sum(Q_A((A1_number_zones+1):(2*A1_number_zones)));
Q_balance = Q_i_total + Q_o_total;

fprintf('Heat In (W): %.2f\n',Q_i_total);
fprintf('Heat Out (W): %.2f\n',Q_o_total);
fprintf('Energy Balance (W): %.2f\n',Q_balance);
fprintf('Front Surface Temp (K): %.2f\n',T_i(1));

toc

end

c = clock;
userview = memory;

```